Title
Engineering Nano-Structured Multiferroic Thin Films

Author
Cheung, Pui Lam

Publication Date
2017

UNIVERSITY OF CALIFORNIA

Los Angeles

Engineering Nano-Structured Multiferroic Thin Films

A dissertation submitted in partial satisfaction of the
requirements for the degree Doctor of Philosophy
In Chemical Engineering

by

Pui Lam Cheung

2017

ABSTRACT OF THE DISSERTATION

Engineering Nano-Structured Multiferroic Thin Films

by

Pui Lam Cheung
Doctor of Philosophy in Chemical Engineering
University of California, Los Angeles, 2017
Professor Jane Pei-Chen Chang, Committee Chair

Multiferroics exhibit remarkable tunabilities in their ferromagnetic, ferroelectric and magnetoelectric properties that provide the potential in enabling the control of magnetizations by electric field for the next generation non-volatile memories, antennas and motors. In recent research and developments in integrating single-phase ferroelectric and ferromagnetic materials, multiferroic composite demonstrated a promising magnetoelectric (ME) coupling for future applications. Atomic layer deposition (ALD) technique, on the other hand, allows fabrications of complex multiferroic nanostructures to investigate interfacial coupling between the two materials.

In this work, radical-enhanced ALD of cobalt ferrite (CFO) and thermal ALD of lead zirconate titanate (PZT) were combined in fabricating complex multiferroic architectures in investigating the effect of nanostructuring and magnetic shape anisotropy on improving ME coupling. In particular, 1D CFO nanotubes and nanowires; 0D-3D CFO/PZT mesoporous composite; and 1D-1D CFO/PZT core-shell nanowire composite were studied. The potential

implementation of nanostructured multiferroic composites into functioning devices was assessed by quantifying the converse ME coupling coefficient.

The synthesis of 1D CFO nanostructures was realized by ALD of CFO in anodic aluminum oxide (AAO) membranes. This work provided a simple and inexpensive route to create parallel and high aspect ratio (~55) magnetic nanostructures. The change in magnetic easy axis of (partially filled) CFO nanotubes from perpendicular to parallel in (fully-filled) nanowires indicated the significance of the geometric factor in controlling magnetizations and ME coupling.

The 0D-3D CFO/PZT mesoporous composite demonstrated the optimizations of the strain transfer could be achieved by precise thickness control. 100 nm of mesoporous PZT was synthesized on $Pt/TiO_x/SiO_2/Si$ using amphiphilic diblock copolymers as a porous ferroelectric template (10 nm pore diameter) for ALD CFO growth. The increased filling of CFO decreased the mechanical flexibility of the composite for electric field induced strain, hence the converse ME coupling was mitigated. The highest converse ME coefficient of 1.2 10^{-5} Oe-cm/mV was achieved with a 33% pore filling of CFO, in compare to 1×10^{-5} Oe-cm/mV from mesoporous CFO filled with 3 nm of PZT in literature (Chien 2016).

Highly directional 1D-1D PZT-core CFO-shell composite in AAO demonstrated the magnetic shape anisotropy could be modulated. The CFO shell thickness allowed the tuning of magnetic easy axis and saturation magnetizations; whereas the PZT volume allowed the optimization of electric field induced strain of the composite. Enhanced converse ME coupling of 1.3×10^{-4} Oe-cm/mV was realized by 5 nm CFO shell on 30 nm of PZT core.

In summary, the work has demonstrated nanostructuring of multiferroic composite is an effective pathway to engineer converse ME coupling through optimizations of magnetic shape anisotropy and interfacial strain transfer.

The dissertation of Pui Lam Cheung is approved.

Yunfeng Lu

Yvonne Chen

Sarah H. Tolbert

Jane Pei-Chen Chang, Committee Chair

University of California, Los Angeles

2017

This page is intentionally left blank.

TABLE OF CONTENTS

LIST OF FIGURES

LIST OF TABLES

ACKNOWLEDGEMENTS

This work and my last five years in this program would not have been possible without the input, support, and caring from countless number of people. Unfortunately, although I have tried to include as many people as I could, I will have inevitably left out some people who also deserve to be thanked for which I apologize for not mentioning.

I would first like to thank my graduate advisor, Professor Jane P. Chang for the guidance and lessons she has given me throughout my graduate studies. Since my undergraduate research in the lab, I thank her for taking a chance on me and giving me this wonderful opportunity of conducting researching in her lab. Her critical analyses in research and high standard in presentations have encouraged me to improve myself continuously. Her attention in details for both writing manuscripts and presenting at conferences are the values I have learned from her and will last throughout my professional career. I hope that I will be able to live up to her high expectation after I leave the academic setting. I would also like to thank my dissertation committee, Professor Sarah Tolbert, Yunfeng Lu, and Yvonne Chen for their time and input as well as the funding support from TANMS and FAME.

The member of Chang Lab must also be thanked for their input and companionship. Without which, both work and life would not have been nearly as pleasant. I must thank my mentor Vladan Jankovic, who taught me not only critical analysis skills, but also his guidance and mentality in both research and life. I would like to thank Jay Cho and Colin Rementer for their support and guidance when I was lost in research; Jeffrey Chang and Kevin Fitzell for their tremendous help in experimental work and countless hours in discussing results; Ryan Sheil for his willingness to learn and dedication to research which helped motivate me to be a better mentor; Nicholas Altieri for bringing all the joyful moments in the lab. In addition, the other members of the lab which I had the privilege of working with and knowing: Wilson Lin, James Dorman, Jack Chen, Diana Chien, Trevor Seegmiller, Taeseung Kim, Younghee Kim, Luke Minardi, and Ernest Chen. Outside the Chemical Engineering department, I have had the pleasure to collaborate with Abraham Buditama and Ty Karaba.

I would like to give thanks to all my friends who gave me support during my PhD career, especially Rainbow Siu for her encouragements during the most difficult times. In addition, I would like to give special thanks to Karen Wong for the companionship and motivations.

Last but most importantly, I would like to thank my parents, my brother, and my uncle, for the love and support that I got while studying overseas at UCLA in the past ten years. It has been truly wonderful and plentiful and it would not have been possible for me to come this far without their encouragement and guidance.

VITA

2012	Undergraduate Research Assistant Department of Chemical and Biomolecular Engineering University of California, Los Angeles
2012	B.S., Chemical and Biomolecular Engineering (Specialization in Semiconductor) University of California, Los Angeles Los Angeles, CA
Mar-Jun 2013	Teaching Assistant Department of Chemical and Biomolecular Engineering University of California, Los Angeles
2012-2017	Graduate Student Researcher Department of Chemical and Biomolecular Engineering University of California, Los Angeles

PUBLICATION AND PRESENTATIONS

Cheung, P., Chang, J., Chang, J. P., presentation of "Magnetic Anisotropy of $CoFe_2O_4$ Nanotubes Synthesized by Radical-Enhanced ALD", 2016 AVS 63rd International Symposium and Exhibition, Nashville, TN, November 2016

Cheung, P., Chang, J., Chang, J. P., poster presentation of "Magnetic Anisotropy of $CoFe_2O_4$ Nanotubes Synthesized by Radical-Enhanced ALD", 2016 SCCAVS, Buena Park, CA, October 2016

Cho, J., Seegmiller, T., Lau, J., Smith, L., Hur, J., Cheung, P., Dunn, B., Chang, J. P., presentation on "Engineering Lithium-Containing Ionic Conductive Thin Films by Atomic Layer Deposition for Li-ion Battery Applications", 2015 AVS 62nd International Symposium and Exhibition, Long Beach, CA, October 2015

Liang, K., Buditama, A., Chien, D., Cui, J., Cheung, P., Goljahi, S., Tolbert, S. H., Chang, J. P., and Lynch, C. S., "The Conductivity Mechanism and Improved C-V Model of Ferroelectric PZT Thin Film," Journal of Applied Physics, 117, 174107 (2015)

Janković, V., Yang, Y., You, J., Dou, L., Liu, Y., Cheung, P., Chang, J. P., Yang, Y., "Active Layer-Incorporated, Spectrally Tuned Au/SiO_2 Core/Shell Nanorod-Based Light Trapping for Organic Photovoltaics," ACS Nano, 7, 5, 3815-3822, (2013).

CHAPTER 1 INTRODUCTION

New generation power efficient devices have become the center of modern technology advancements ranges from microprocessors, batteries and storage memories. The renaissance of multiferroic materials is evidenced by novel discoveries and concepts, both experimentally and theoretically. In this study, various progressive milestones are outlined, especially the leap from single-phase multiferroic materials, which ferromagnetism and ferroelectricity coexist, to engineer nanocomposites. Potential applications of multiferroic composites were strengthened due to the flexibility to purposely select the material of each ferroic material, and its increased performances in magnetoelectric coupling have significant improvement. To begin, the motivation and fundamentals of multiferroicity are detailed, in transition to advantages of engineered nanocomposites.

1.1 Motivation

Densification and miniaturization have been the development trend for electronic devices. Memory storage device, in particular, has shrunk down its size exponentially. Since the invention of dynamic random access memories (DRAM), memory devices have become an essential part in integrated circuits. They are embedded in many digital electronics such as cellphones, computers, and other mobile devices. Memory capacity and density has doubled according to Moore’s Law every 24 months. Over the last decades, the market size of memories was increased to 77-billion-dollar as of 2016. The compound annual growth rate (CAGR) of memory devices was predicted to be higher than average IC industry in the next 5 years, according to the market research (McClean 2017).

While downscaling raises concerns in existing memory architectures, a fast, scalable and energy efficient memories is needed. Performances and maturity of various kinds of memories were summarized in Table 1.1. Traditional DRAMs have simple and compact 1T1C architecture. Its capacitor charge-discharge mechanism has a retention time of 64 milliseconds, which requires energy to refresh each memory bit in order to retain the information. Therefore, it maintains an undesired power consumption and barrier in downscaling.

In order to fundamentally eliminate the use of stored electrical charge, ferroelectric RAM (FeRAM) and magnetoresistive RAM (MRAM) utilized the ferroic orderings (polarizations and magnetizations, respectively) of the ferroic materials to store the information. It no longer needs a periodic refresh. However, the single-layer cell (SLC) size of such devices is often larger while the energies required for reading and writing are higher than traditional DRAMs. As a result, new memory devices were proposed and being researched on aiming to achieve higher power efficiency and smaller footprint.

Considering the essential performance metrics such as SLC size, energy per bit, write and read (W/R) access time, endurance, and retention, a faster and more efficient memory is needed for further downscaling. The W/R access time of hard-disc drives (HDD) is limited to 9.5 ms and 8.5 ms due to the physical movements of the disc head. The short retention of information in DRAMs is undesired in nanoscale as the energy for refresh becomes more significant in smaller devices. Flash memories, on the other hand, has a relatively high W/R time at 200 μs and 25 μs due to the use of floating gate and charge pumps. The endurance, or lifetime, of flash memory is ten orders of magnitude lower than DRAM. MRAM has a large footprint of $20F^2$ and high energy per bit of 120 pJ. Newer types of memory such as spin-transfer torque RAM (STT-RAM) uses spin polarized tunneling current for writing requires 0.02 pJ energy per bit with a comparable W/R time to DRAM. However, the memory has low memory capacity due to issues such as memory crosstalks in high-density configurations.

Table 1.1 Performances of various memory devices (Kryder 2009)

Device	HDD	DRAM	Flash	FeRAM	MRAM	STTRAM	MeRAM*
SLC size	$(2/3)F^2$	$6F^2$	$4F^2$	$6F^2$	$20F^2$	$4F^2$	/
Energy/bit	N/A	2pJ	10nJ	2pJ	120pJ	0.02pJ	1fJ
W/R time	9.5/8.5ms	10/10ns	200/25μs	50/75ns	12/12ns	10/10ns	1/1ns
Endurance	N/A	10^{16}	10^{5}	10^{15}	10^{16}	10^{16}	/
Retention	N/A	64ms	10yr	10yr	10yr	10yr	10yr
Maturity	Product	Product	Product	Product	Product	Prototype	Research

* MeRAM performances are based on the projection (Wang 2013)

Magnetoelectric effect, as one of the candidate properties, has been studied for decades since the discovery of multiferroicity in bismuth ferrite, $BiFeO_3$ in 1950s. Aiming for a more energy efficient device, a possible memory structure was proposed in 2008 with the use of interfacial exchange coupling of ferromagnetic layer with antiferromagnetic layer (Bibes 2008), which was expected to have faster writing time (~1ns), lower writing energy (~1fJ), and more importantly, multi-level cell capability (Amiri 2012). Researchers have demonstrated the possibility of switching local ferromagnetic domains with electric field using multiferroics (Yang 2009). Although prototype magnetoelectric RAMs have yet to be built, the interesting aspects of magnetoelectric coupling and its potential in the energy efficient devices are nonetheless attractive to research community.

1.2 Ferromagnetism (FM)

Magnetic materials can be categorized into the following classes: Diamagnetic, paramagnetic, ferromagnetic (FM) and antiferromagnetic (AFM). Materials are classified as diamagnetic when spontaneous opposing field is induced under an external magnetic field. The electron configuration of diamagnetic material is usually fully filled that no permanent magnetic moment could contribute to magnetization. Some materials such as copper oxide possess perfect diamagnetism for superconductivity when quenched below a critical temperature. A strong opposing field could be induced spontaneously to exclude any magnetic flux from its surface, known as Meissner effect. Most transitional metal salts are paramagnetic that magnetization increases proportionally to the applied magnetic field as suggested by Curie-Weiss Law. The net magnetic moment originates from the partially filled *d*-shell. With a weak coupling between neighboring spins through the mediation of anions in the crystal structure, the small magnetization is perfectly reversible to its random state when applied field is removed. Graphs of M as a function of H, namely magnetization curves, are commonly used as an illustration of magnetism types of materials. In paramagnets and diamagnets, the magnetization curves are represented by a positive and negative slope respectively, both of which are reversible in dipole moment orientations, restoring its random alignments when the applied field is removed.

In ferromagnetic materials, the neighboring spins are coupled and aligned in the same orientation to achieve a lower energy state. Ferromagnets become paramagnets when the temperature elevated beyond Curie temperature, T_c. Above the critical temperature, thermal energy outweighs the coupling of spins, and thus destroying the long-range FM ordering. The derivation is explained in Appendix A. The importance of ferromagnets originates from their hysteresis characteristics under applied magnetic field. The magnetization increases with increasing magnetic field until reaching saturation Ms with a corresponding field H_s. Further elevation of magnetic field strength does not change magnetization value since all magnetic (Weiss) domains are aligned, reaching its maximum value. In B-H plots, though, the magnetic induction increase linearly because of intrinsic response to applied magnetic field beyond saturation. A typical hysteresis response is shown below in Figure 1.1.

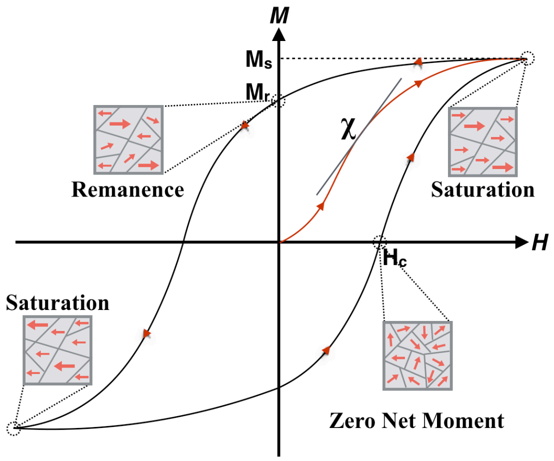

Figure 1.1 Magnetic hysteresis for ferromagnets with domain orientations

When the applied field slowly decreases, magnetization does not follow the previous path, but a curve with higher magnetization values due to the strong coupling of domains in ferromagnets. When the applied field is removed, the intrinsic demagnetizing field rotates domains in opposite direction. However, such field is not strong enough to overcome the exchange interactions between domains. The magnetization remains as remanence or remnant magnetization M_r. Fully demagnetization occurs at coercivity or coercive field strength H_c, which is a measure of the “hardness” of the material and the energy required for demagnetization. The net magnetic moment is zero but not necessarily randomized.

Further increase in the opposing field would orient domains as previously described by saturating the magnetization in the different direction, and complete the loop by increasing the field until the positive coercivity. The entire loop is termed hysteresis curve. The permeability is represented as the slope of the curve as a function of the applied field. The magnetic dipoles cannot be reset to random alignment unless the material is heated beyond its Curie temperature, Tc, above which becomes paramagnetic as thermal energy dominates.

Unlike paramagnets, ferromagnets allow the neighboring spins to have parallel orientation instead of randomly oriented. From quantum mechanics, the system with parallel spins is more energetically favorable due to exchange interactions between spins, overcoming the thermal energy in randomly aligning spins. Exchange interaction occurs between indistinguishable fermions, whose spin number is multiple of half-integer. Electrons are fermions and limited by Pauli exclusion principle that two electrons cannot occupy identical quantum states, suggesting that two electrons are antisymmetric under exchange interaction. Hund's rule suggests electrons tend to maximize their total spin. It indicates each orbital has to be filled with one electron with parallel spin before pairing in the same orbital. Qualitatively, such arrangement minimizes electron spatial overlap between orbitals and thus electron repulsions.

Although quantum mechanics suggested parallel spins contribute the least energy to the system, single magnetic domain is rare in nature. A single-domain material is similar to a permanent magnet that magnetic field conduct in the vicinity of the material, which requires a large magnetostatic energy to sustain. Therefore, magnetic domain intrinsically divides themselves into compartments in order to complete the magnetic circuit (flux closure domain), minimizing the demagnetizing field and the total internal energy of the system.

On the other hand, domains tend to align in certain crystallographic directions (easy axes) as energy required to magnetize in such orientation has lower magnetocrystalline energy. The energy difference in magnetizing easy and hard axes is known as magnetocrystalline anisotropy energy. This quantity has been used extensively, as shown in Figure 1.2 for magnetic random-access memories (MRAM) and voltage-controlled magnetic anisotropy (VCMA) devices for magnetic switching. To minimize the energy, larger domains tend to form along the easy axes for magnetization, while smaller domains with perpendicular orientation form to complete the magnetic circuit.

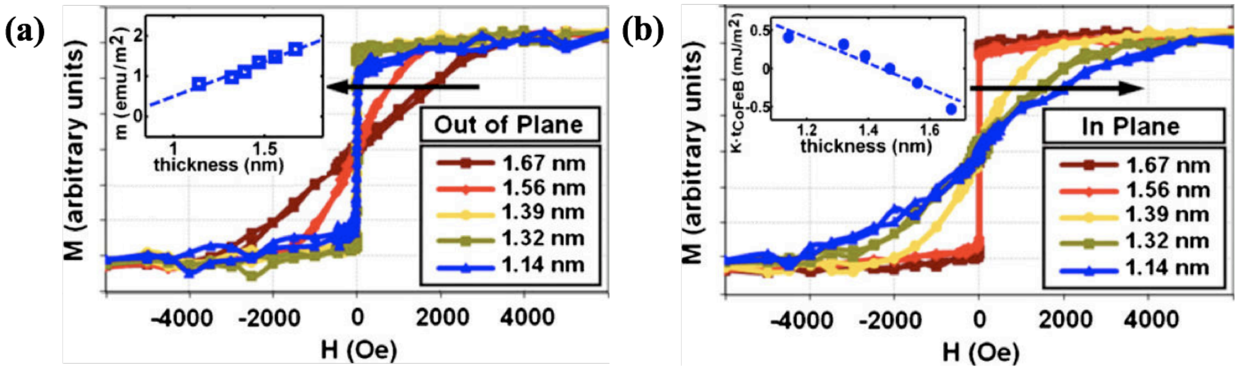

Figure 1.2 M-H curve of CoFeB with (a) out-of-plane and (b) in-plane field at various thickness (adapted from (Amiri 2012))

Table 1.2 summarizes single-phase FM materials commonly used, along with the synthesis methods, magnetostriction (λ_s), saturation magnetizations (M_s), coercivity (H_c), and Curie temperature (T_c). All ferromagnetic materials are magnetostrictive that the material experiences strain when magnetic field is applied as a result of domain reorientation. The strain ranges from 1.4 με for Fe metal to 1200 με for intermetallic TbDyFe. Ferromagnetic metals such as Co and Fe have a high saturation magnetization of 1.78 T and 2.15 T respectively. Intermetallics are primarily synthesized by sputtering and melt, such as NiFe, AlFe CoFe. The adjustment of individual constituents in intermetallic allows tuning of coercivity and saturation magnetostriction. The coercivity of AlFe can be tuned between 0.025 to 0.67 Oe depending on the Al content. Similarly, the magnetostrictive coefficient of CoFe changes from -25 to 86 με. The negative magnetostrictive coefficient indicates the enhancement of magnetization when compressed. Intermetallics with three constituents can also be synthesized by sputtering such as CoFeB, FeGaB and TbDyFe. CoFeB has a higher coercivity of 2 Oe than AlFe while TbDyFe has an exceptional high coercivity of 1200 Oe and saturation magnetostriction of 1200 με. On the other hand, spinel ferrites such as $CoFe_2O_4$ and $NiFe_2O_4$ provide non-conductive alternatives with ferromagnetic properties. They are typically synthesized through wet chemical routes. $CoFe_2O_4$ in particular has a very high negative magnetostrictive coefficient of -164 με that is two orders of magnitude higher than Fe, and a comparable coercivity of 1200 Oe, to TbDyFe. In order to study multiferroic composites, the non-conducting properties of ferrimagnetic $CoFe_2O_4$ is essential when combined with ferroelectric oxides. The high magnetostriction is particularly useful in enhancing the magnetoelectric coupling at the ferromagnetic-ferroelectric interface in strain-mediated multiferroic composites. As a result, $CoFe_2O_4$ is a promising candidate for nanostructured multiferroic composite.

Table 1.2 Summary of single-phase ferromagnetic intermetallic and oxides

Material	Synthesis	Magnetostriction	Ferromagnetic		Curie	Ref
		λ_s ($\mu\varepsilon$)	M_s (T)	H_c (Oe)	T_c (K)	
Fe	Gas Evap.	-1.4	2.15	0.1-1	1000	(Hall 1959, Gong 1991)
Co	Gas Evap.	/	1.784	/	1400	(Gong 1991, Cardarelli 2008)
Ni	Gas Evap.	-38	0.603	/	630	(Hall 1959, Gong 1991, Cardarelli 2008)
Ni_xFe_{100-x}	Melt	4.4 - 25	0.87-1.5	0.06	730	(Hall 1959, Cardarelli 2008)
Si_xFe_{100-x}	Melt	-5 - 10	2.0	0.3-0.6	1000	(Hall 1959, Cardarelli 2008)
Al_xFe_{100-x}	Melt	-5 - 46	0.78-1.2	0.03-0.67	670-730	(Hall 1959, Cardarelli 2008)
Co_xFe_{100-x}	Melt	-25 - 86	/	/	1300	(Hall 1959)
$Co_xFe_yB_{100-x-y}$	Sputter	31	1.5-2.2	0.06-0.12	>1000	(Wang 2005, Lebedev 2012)
$Ni_xCo_yFe_{100-x-y}$	Melt	15	/	0.63-2.00	>1000	(Hall 1959)
FeGaB	Sputter	70	1-1.3	1	900	(Lou 2009)
TbDyFe	Sputter	600-1200	0.75	1200	650	(Sandlund 1994)
Fe_3O_4	Melt	20-40	0.1	/	850	(Bozorth 1955, Zou 2005)
$CoFe_2O_4$	Chemical	-164	0.44	1200	540	(Bozorth 1955, Fritsch 2012)
$NiFe_2O_4$	Chemical	-29 - -17	/	/	880	(Bozorth 1955)

1.3 Magnetic Anisotropy

One factor that strongly influences the magnetic properties of FM materials is magnetic anisotropy. Magnetic anisotropy refers to the difference in energy required to orient magnetization into a specific direction. An energetically favorable orientation of the magnetization is often referred as magnetic easy axis, which is essential to hysteresis properties of FM materials. Magnetic anisotropy can be categorized into magnetocrystalline anisotropy, shape anisotropy, and magnetoelastic anisotropy.

Among three different types of anisotropy, magnetocrystalline anisotropy is the intrinsic property originated from directional dependence of crystal structures. In a simple cubic structure of iron, for example, the <100> orientation requires less energy to be magnetized than the <111> due to the coupling between orbit and the crystal lattice. As a result, the magnetization in the <100> orientation saturates at a lower magnetic field as shown in Figure 1.3. As mentioned in Appendix A, the origin of magnetism is the combination of spin and orbital angular momentum. Although there are exchange interactions between neighboring spins, the coupling between the crystal lattice and the orbital is very strong that cannot be changed easily as a result of bonding. When an external magnetic field is applied, both spin and orbital of electrons tend to orient themselves into the direction of the field. While the orbitals are strongly coupled to the lattice, they are limited in reorientation. Due to spin-orbit coupling, the spin reorientations are indirectly restricted, resulting in magnetocrystalline anisotropy.

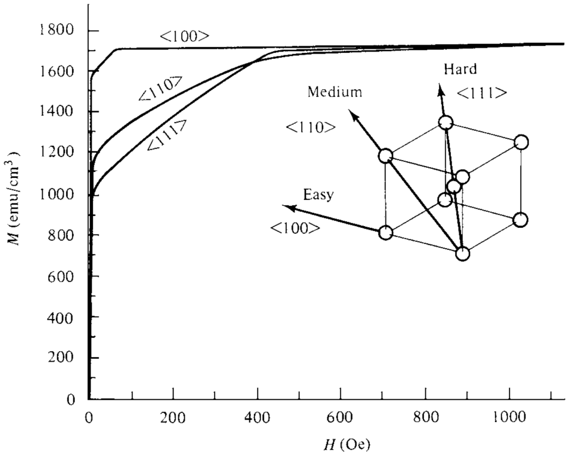

Figure 1.3 Magnetization curves for single crystals of iron in different crystalline orientations: <100>, <110> and <111> (adapted from (Cullity 2005))

The energy required to reorient the magnetization orientation from the easy axis is defined as anisotropy energy, E_{ani}, which is expressed as a series expansion of the cosines of the angle between the magnetization orientations (S_1, S_2, S_3) and crystal axes with anisotropy constants (K_0, K_1, $K_{2, \ldots}$). In a cubic crystal, the anisotropy energy can be expressed as,

$$E_{ani} = K_0 + K_1(S_1^2S_2^2 + S_2^2S_3^2 + S_1^2S_3^2) + K_2(S_1^2S_2^2S_3^2) \tag{1.1}$$

In a polycrystalline substrate, other magnetic anisotropies dominate as the magnetocrystalline anisotropy is negligible from the isotropic nature of the substrate. Magnetoelastic anisotropy is originated from magnetostriction of the material under applied magnetic field. All FM materials are magnetostrictive, which elongates or contracts upon magnetization, as shown in Figure 1.4. When magnetic field is applied, the electron spins are oriented and aligned. The shape of the electron cloud is therefore rotated and forces the neighboring nuclei to move away or closer to each other. As a result, the material is expanded or contracted. The strain response is in the order of με due to the reluctance to change from lattice-orbital coupling, in comparison with the relatively weaker spin-orbit coupling.

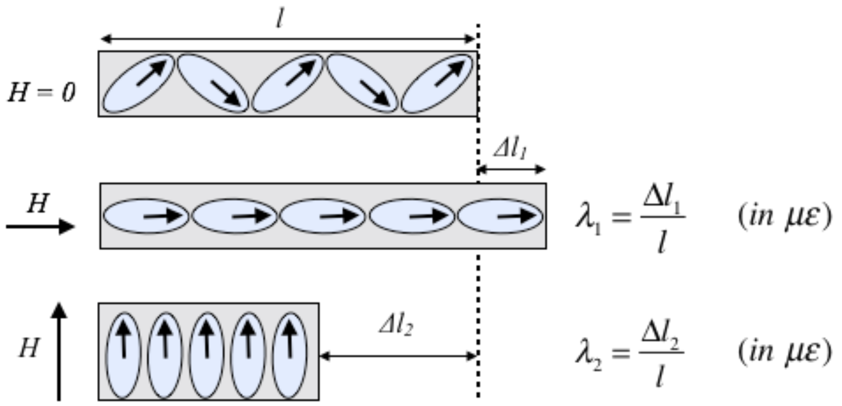

Figure 1.4 Schematic of magnetostriction under applied magnetic field

Magnetostriction is quantified by the saturation magnetostrictive coefficient, λ_s, at which the materials is fully strained in one direction. In a cubic crystal, the saturation magnetostrictive coefficient can be expressed as,

$$\lambda_s = \lambda_{100} + 3(\lambda_{111} - \lambda_{100})(S_1^2 S_2^2 + S_2^2 S_3^2 + S_1^2 S_3^2) \tag{1.2}$$

where λ_{100} and n_{111} are the saturation magnetostriction measured in (100) and (111) crystallographic direction respectively.

Magnetic shape anisotropy is originated from the geometry and physical boundaries of the magnetic structure. For a polycrystalline substrate, there is zero net magnetocrystalline anisotropy. Consider a bar is magnetized by a magnetic field pointing to the right of the page. After the external field is removed, the north pole is located on the top of the ellipsoid as shown in Figure 1.5. Magnetic field is generated not only outside of the magnet, but also within the magnet. The magnetic field lines inside the bar, however, point in the opposite direction of the magnetization of the magnet itself, which tends to demagnetize the bar. As a result, the field is termed demagnetizing field, H_{demag}. This demagnetizing field is stronger near the poles while weaker near the center. The closer the poles are, the stronger is the demagnetization field near the center.

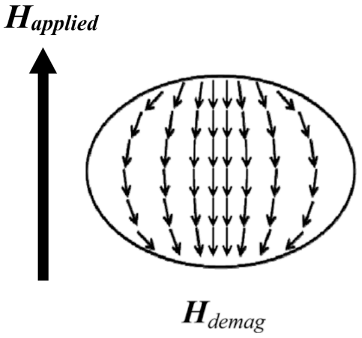

Figure 1.5 Schematic of demagnetizing field of a bar magnet

If the substrate is not spherical in shape, it is easier to magnetize along the long axis than the short axis due to the energy required to overcome the demagnetization field is less along the long axis than that along the short axis. In order to quantify shape anisotropy, the magnetostatic energy, E_{ms}, is defined as the total energy stored by demagnetization field. Consider a prolate ellipsoid with a long axis of length *a* and short axis of length *b* and *c*, the magnetostatic energy is given by,

$$E_{ms} = 0.5M^2N_c + 0.5(N_a - N_b)M^2\sin^2\theta \tag{1.3}$$

where *N* is the demagnetizing coefficient along orthogonal directions such that $N_a + N_b + N_c = 1$; θ is the angle between the magnetization and axis *a.* By manipulating the shape anisotropy and magnetoelastic anisotropy of the magnetic structure, the magnetic easy axis can potentially be switched.

The effect of demagnetizing field can also be seen in magnetic domain formations, as shown in Figure 1.6. In a single magnetic domain, the demagnetizing field is the highest with the strongest stray field outside the domain. In order to reduce the magnetostatic energy, the domain is dissected into two smaller rectangular antiparallel domains. The magnetic circuit is completed when four domain are formed with the minimum magnetostatic energy as no stray field occurs outside the domains.

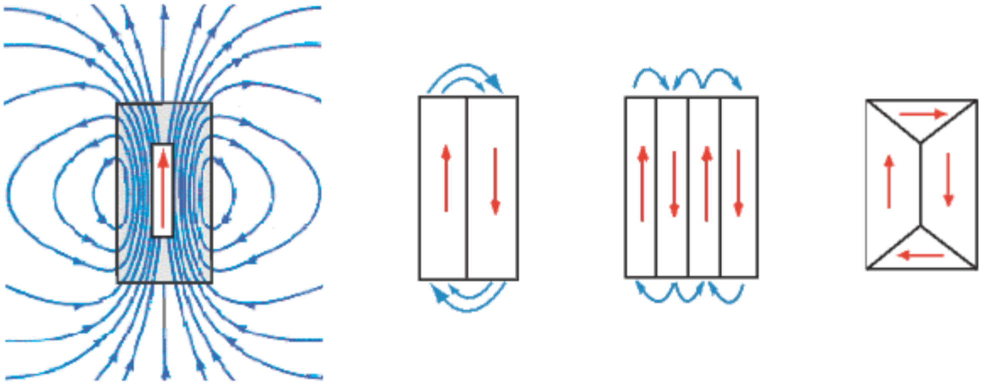

Figure 1.6 Schematic of demagnetizing field in different partitions of magnetic domains in a bar magnet (adapted from (Tipler 1999) and (Hubert 1998).

The shape anisotropy is directed affected by the demagnetization of the structures. In the case of a nanopillar, the magnetic domains along the pillar elongates while the domain in perpendicular are shrunk. Therefore, the net magnetization along the pillar increases while diminishes in the perpendicular orientation. The effect was demonstrated when cobalt ferrite pillars of 20 nm diameter were grown on bismuth ferrite using pulsed-laser deposition, as shown in Figure 1.7. The magnetization parallel to the nanopillars showed an enhancement in both saturation magnetization and coercivity.

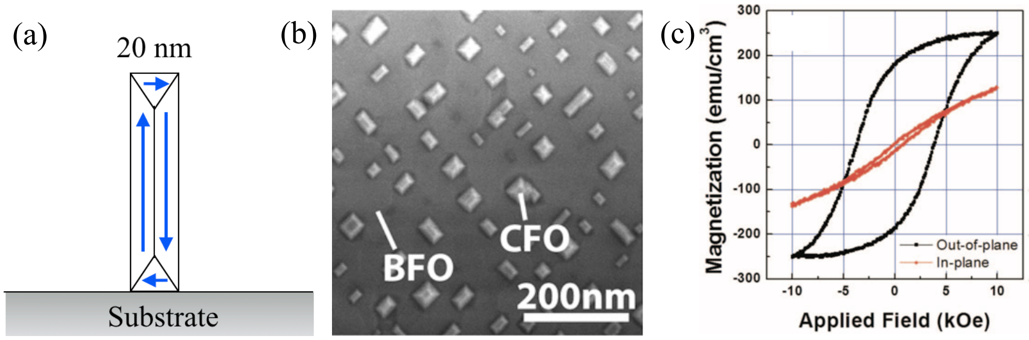

Figure 1.7 (a) Schematic of magnetic domains of a standing nanopillar with diameter of 20 nm. (b) 20 nm of $CoFe_2O_4$ nanopillar of aspect ratio of 1 was grown on $BiFeO_3$ by PLD with corresponding magnetic hysteresis (Kim 2014)

1.4 Ferroelectricity (FE)

Ferroelectric (FE) materials have attracted great interests from the research field due to the multi-functionality of the material class. Ferroelectrics are at the same time dielectric, pyroelectric (thermal-electric field coupling), and piezoelectric (strain-electric field coupling). It has the potential in controlling strain, polarizations and thermal effects by electric field. In analogy to ferromagnetism describing materials magnetization as a function of magnetic field, ferroelectricity describes the electric polarizations of the material as a function of electric field.

Dielectric materials, in general, are generally described as the ability to conduct electric field lines through the material before electrical breakdowns. Materials that could sustain large amount of electric field are regarded as insulators. When electric field, $E = E_0 e^{\mathrm{iie}}$ [V/m], is applied to dielectric materials, electric flux density (electric displacement) appears, $D = D_0 e^{\mathrm{i[V}}$ [C/m^2]. It describes the degree of bound charge displaced from its equilibrium position under an applied electric field. The proportionality is described by permittivity, ε [F/m], of the medium. The subscript *0* and *r* correspond to vacuum and relative permittivity respectively

$$\mathbf{D} = \varepsilon \mathbf{E} = \varepsilon_0 \varepsilon_r \mathbf{E} \tag{1.4}$$

Piezoelectricity of ferroelectric materials originates from the unbalanced polarization intrinsically from crystal structure. Among 32 crystal classes, 11 point groups are centrosymmetric, which often have balanced polarizations. The remaining non-centrosymmetric crystal classes, with one exception, are piezoelectric. Unlike electrostrictive effect, piezoelectric effect is a bipolar response and has the ability to expand or contract depending on the direction of the field. The inverse effect produces electric field under mechanical stress. The coupling of strain and polarization can be illustrated as,

$$\begin{cases} \mathbf{P} = d\sigma + \varepsilon_0 \chi \mathbf{E} \\ \mathbf{S} = s\sigma + d^T \mathbf{E} \end{cases} \tag{1.5}$$

where S and σ are the strain and stress tensors respectively; s is the elastic compliance; and d is the piezoelectric coefficient [m/V]. Common materials such as barium titanate ($BaTiO_3$), lead zirconate titanate (PZT), and lithium niobate ($LiNbO_3$) are used as actuators, microphones, motors and ultrasound generators.

Perovskite structure is an example of intrinsically unbalanced polarization and leads to ferroelectricity through ion displacive mechanism. It has a chemical formula of $A^{(2+)}B^{(4+)}O3$, which A and B are metal cations, as shown in Figure 1.8. Cation A are located at cubic corners (0,0,0) with eightfold coordination, cation B situated in the body-center (½,½,½) positions with octahedral coordination, while the oxygen atoms occupy face-centered position (½,½,0), as shown in Figure 1.8(a). The smaller cation usually located at the body-center with a charge of +4. More importantly, perovskites have cubic structure (centrosymmetric) with space group *P*m3m above the Curie temperature, and became tetragonal P4mm (non-centrosymmetric) at temperature below and exhibit spontaneous polarization. Some complex perovskites contain two types of B-site cation to increase possible coordination of the domains, such as PZT ($Pb(Zr_{1-x}Ti_x)O_3$) whose neighboring cubic cell contain different B-site ions.

Under external electric field, cations and anions displace from the resting position corresponding to the field direction. In perovskite structures, similar displacements of the ions are observed. As the face-center sites for oxygen atoms do not have cubic surrounding, the local field is relatively large, and thus a larger response in ferroelectricity. A net ionic polarization is then observed from the separation between the cation A and the surrounding oxygen atoms, as shown in Figure 1.8(b).

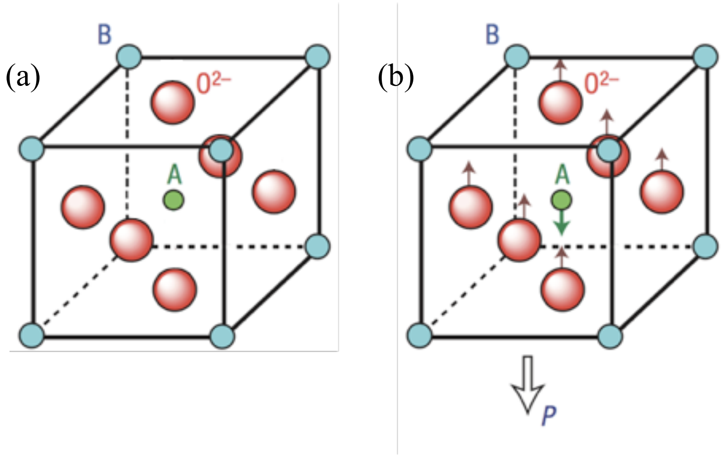

Figure 1.8 The displacive mechanism in perovskite structure ABO_3 such as PZT, responding to external electric field (adapted from (Horiuchi 2008)).

When the external field is removed, the polarization retains. Unlike ferromagnetism, polarization does not involve spin-orbital coupling and thus there is no exchange interaction between spins to stabilize the structure when Coulomb repulsion exists. Theoretical calculation shows that transition B-site ions allow d-hybridization with oxygen, which weaken short-range B-O repulsions (Cohen 1992). On the other hand, A-site ions stabilize the structure by coupling the ferroelastic responses to the FE distortions, which is usually on the order of 0.1Å. The total free energy is then decreased, as shown in Figure 1.9. At certain degree of distortion, the energy diagram shows local minimums especially in tetragonal crystal structure.

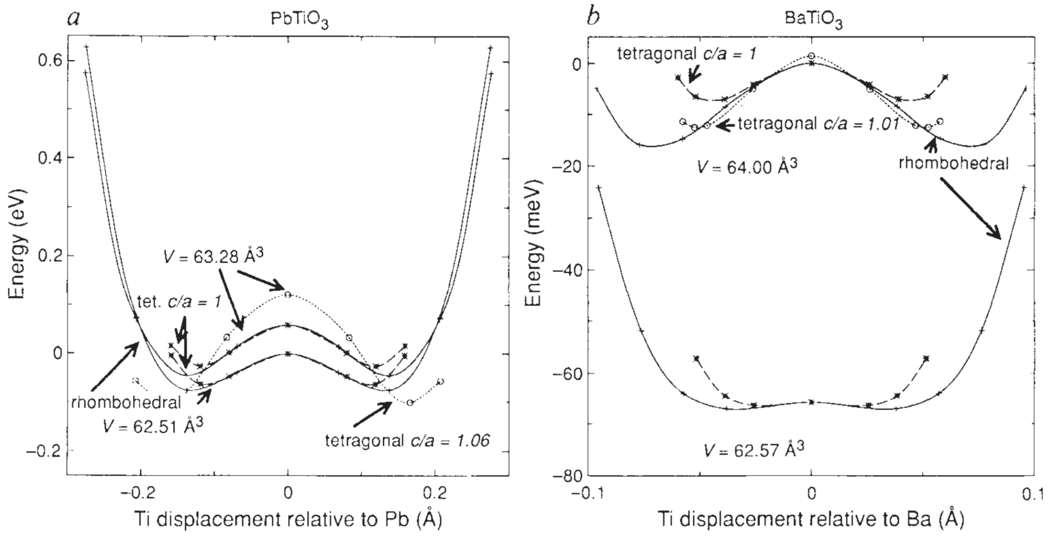

Figure 1.9 Calculated energy diagram as a function of ferroelectric distortion for (a) $PbTiO_3$ and (b) $BaTiO_3$ using local density approximation. Local minimum shows stabilized state with polarization (adapted from (Cohen 1992)).

The cause of polarization is further described by the softening and freezing of longitudinal optical phonons that the frequency of the phonon decreases and becomes zero at phase transition. Mathematically, the amplitude of the phonon mode (i.e. dipole moment) becomes the order parameter in Landau theory, which is discussed in the Appendix A.

The polarization of ferroelectric materials can also be reversed in analogy to magnetizations in ferromagnetism. Hysteretic polarization curves as a function of electric field are observed. Similarly, saturation polarization (P_s), remnant polarization (P_r), and coercive field (E_c) are the figures of merit of a particular ferroelectric material. Detail definition of the parameters can be referred to the description regarding magnetic hysteresis loop. One of the interesting features of FE material is the voltage-dependent permittivity. It is usually shown in capacitance-voltage (*C-V*) and dielectric constant-voltage (ε *a*) characteristics. “Butterfly” shape is observed by changing DC voltage in two opposing directions, as shown in Figure 1.10. Such C-V profile measures the change of polarization with respect to the change in electric field. Therefore, the peak of capacitance corresponds to a large polarization change, at which near the vicinity of coercive field, which is the energy required to decouple parallel magnetizations (or polarizations). The vicinity of the coercive field induces the largest domain reorientations and thus a high capacitance. Further voltage increase results in suppression of capacitance due to depletion of space-charge effects similar to MOS devices.

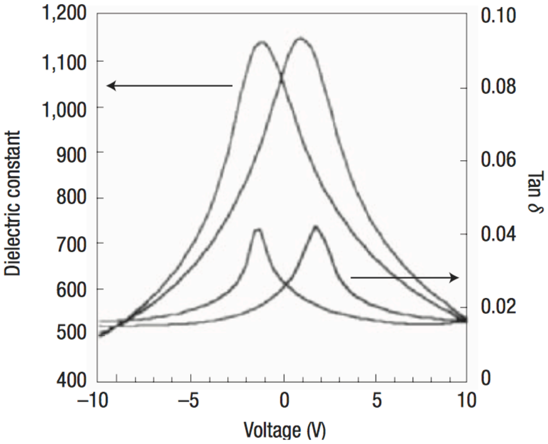

Figure 1.10 Dielectric constant (permittivity) as a function of voltage in PZT (1.2 μm) on Cu. Dielectric "Butterfly" characteristic is observed (Kingon 2005).

Different types of intrinsic FE materials such as lead-based materials, metal niobates, and doped-materials are summarized in Table 1.3 along with typical synthesis methods, piezoelectric coefficients (d_{33}), saturation polarizations (P_r), coercivities (E_c), and Curie temperatures (T_c). Several categories of the intrinsic ferroelectric materials such as manganese oxides (RMn_2O_5, $RMnO_3$), chromates ($RCrO_2$), and borates ($RFe_3(BO_3)_4$) are not included as they possess small piezoelectric response with T_c below room temperature. The synthesis techniques varies from wet chemical methods (co-precipitation, sol-gel) to pulsed-laser deposition. Common ferroelectric material such as $BiFeO_3$ with a saturation polarization of 55 μC/cm^2 was considered to be a candidate for multiferroic memories. The piezoelectric coefficient, d_{33}, is the measure of piezoelectric responses defined as the ratio of strain and applied electric field, which is exceptionally important for multiferroic composite. $LiNbO_3$ is commonly used in telecommunication for generating surface acoustic waves due to its piezoelectric properties, which has a value of 31.5 pm/V. Other niobate compounds such as $KNbO_3$ and $NaNbO_3$ with enhanced piezoelectric properties above 400 pm/V are being researched as $LiNbO_3$ alternatives as lithium is expensive. Lead-containing compounds remain dominant for their strong piezoelectric responses, which is ideal for strain-mediated multiferroic composites. Both $Pb(Mg_{0.33}Nb_{0.67})O_3$-$PbTiO_3$ (PMN-PT) and $Pb(Zn_{0.33}Nb_{0.67})O_3$-$PbTiO_3$ (PZN-PT) have a coefficient two orders of magnitude higher than $LiNbO_3$ at 2000 and 2500 pm/V respectively. The Curie temperatures are about 400 K, far below that of $LiNbO_3$ at 1413 K. On the other hand, PZT is simpler to synthesize while retaining FE properties. PZT is a common choice of material for research in multiferroic nanocomposites because its saturation polarization and coercivity are in the same order of magnitude with PMN-PT and PZN-PT, while its Curie temperature is higher at 600K, and has a piezoelectric coefficient of 500 pm/V, which is higher than the lead-free materials. Therefore, PZT is a promising candidate in studying nanostructured strain-mediated multiferroic composite in this work.

Table 1.3 Summary of key properties of ferroelectric materials

Ferroelectric Material	Synthesis	Piezoelectric	Ferroelectric		T_c (K)	References
		d_{33} (pm/V)	P_r (μC/cm^2)	E_c (kV/cm)		
$DyFeO_3$	Float Zone	/	0.2	22	/	(Tokunaga 2008)
$BiFeO_3$	PLD	0.05	55	15	1123	(Catalan 2009)
$BaTiO_3$	PLD	190	~1	~1	388	(Zhang 2009)
$BiCrO_3$	PLD	0.5	~1	~1	/	(Nechache 2007)
$(Bi,Dy)(Fe,Ti)O_3$	Solid-state Reaction	/	23	75	543-603	(Zhu 2009)
BNT-BKT-BLT	Solid-state Reaction	140-190	40	29	390-490	(Takenaka 2009)
$LiNbO_3$	Czochralski	31.5	/	40	1413-1473	(Gopalan 1998)
$KNbO_3$	Molten salt	400	13	10	570	(Zheng 2014)
$NaNbO_3$	Co-ppt	323-416	15-18	10	800	(Wu 2014)
$(K,Na)NbO_3$	Co-ppt	71	25	17	693	(Zhang 2006)
PZT	Sol-gel	300-500	15-33	25	601	(Ma 2003)
PMN-PT	Flux method	1000-2000	18-26	4-15	373	(Ho 1993)
$Pb(Zn,Nb)O_3$	Solid-state Reaction	1100	43	3.8	413	(Park 1997)
PZN-PT	Solid-state Reaction	2500	40	3	430	(Park 1997)

1.5 Multiferroic Composite Materials

Multiferroic materials, which possess more than one primary ferroic orders, has been grown in interests in recent years for various applications such as random-access memory (RAM), sensors and MEMs. Multiferroicity allows the formation of switchable domains from ferroelectricity (FE), ferromagnetism (FM). Figure 1.11 has illustrated the two ferroic orders in logic circles for a clearer understanding of the categories. Multiferroicity requires the materials to be both ferroelectric and ferromagnetic.

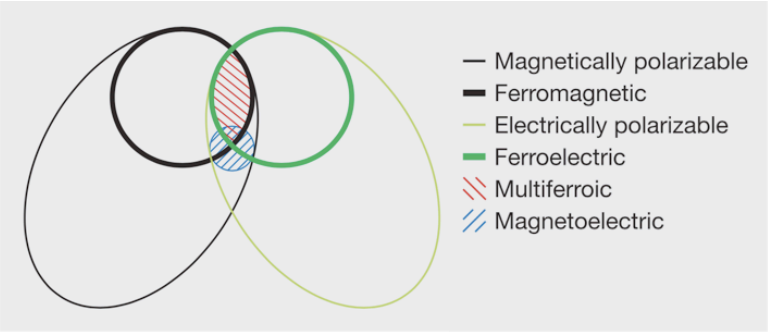

Figure 1.11 Relationship between multiferroic and magnetoelectric materials. (Eerenstein 2006).

The coupling and interaction between various ferroic orders introduces new properties, among which magnetoelectric (ME) effect attracts the most attention for its versatility in controlling magnetization by electric field and polarization by magnetic field. Direct (linear) ME effect controls electric polarization *P* by applied magnetic field *H*, while converse ME effect controls magnetization *M* by applied electric field *E*.

Magnetoelectric coupling coefficient was derived using Landau Theory of a single-phase multiferroic. The free energy, *F*, could be rewritten in terms of electric and magnetic field (Ascher 1966):

$$\begin{aligned} F(\vec{E},\vec{H}) = F_0 - P_{s,i}E_i - M_{s,i}H_i - \frac{1}{2}\varepsilon_0\varepsilon_{ij}E_iE_j - \frac{1}{2}\mu_0\mu_{ij}H_iH_j \\ -\alpha_{ij}E_iH_j - \frac{1}{2}\beta_{ijk}E_iH_jH_k - \frac{1}{2}\gamma_{ijk}H_iE_jE_k - \ldots \end{aligned} \tag{1.6}$$

where the subscript *s* represents the spontaneous polarization and magnetization; subscripts *i*,*j*, and *k* represent dimensions; *ε* and *μ* are the permittivity and permeability of the material respectively; and the coefficients *α*, *β* and *γ* are tensors that correlate free energy change in polarization by magnetic field or vice versa. The differential change of free energy with respect to electric field yields the overall polarization. Similarly, magnetization can be obtained.

$$P_i\left(\vec{E},\vec{H}\right)=-\frac{\partial F}{\partial E_i}=P_{s,i}+\varepsilon_0\varepsilon_{ij}E_j+\alpha_{ij}H_j+\frac{1}{2}\beta_{ijk}H_jH_k+\gamma_{ijk}H_iE_j-\ldots \tag{1.7}$$

$$M_i\left(\vec{E},\vec{H}\right)=-\frac{\partial F}{\partial H_i}=M_{s,i}+\mu_0\mu_{ij}H_j+\alpha_{ij}E_i+\beta_{ijk}E_iH_j+\frac{1}{2}\gamma_{ijk}E_jE_k-\ldots \tag{1.8}$$

The equations contain infinite terms with Einstein summation notation embedded. Particularly, the first term has drawn research attention as linear magnetoelectric coefficient, denoted as α_{ME}. It describes the degree of polarization induced by varying magnetic field [mV/cm-Oe]. Converse magnetoelectric effect describes the degree of magnetization induced by an external electric field [Oe-cm/mV].

Intrinsic multiferroic material is uncommon in nature as different crystal symmetries and electronic configurations are required for ferromagnetism and ferroelectricity. Materials that exhibit multiferroicity at room temperature are rare. Bismuth ferrite, for example, is ferroelectric and antiferromagnetic. Other intrinsic materials such as yttrium iron garnet (YIG), rare earth phosphates and boracites have small magnetoelectric coupling with less than 1 mV/cm-Oe (Rado 1984). As a result, intrinsic materials are not self-sufficient in applications, which held back research interests on magnetoelectric effects.

Not until mid 1970s, bulk composite of piezoelectric $BaTiO_3$ and piezomagnetic $CoFe_2O_4$ (CFO) phase was synthesized. $BaTiO_3$ has a piezoelectric coefficient of 190 pm/V (Table 1.3) while CFO has a magnetostrictive coefficient of -164 με (Table 1.2). The two layers were mechanically coupled. Under an external electric field, $BaTiO_3$, layer deformed and strained in the preferred polarization orientation. CFO experienced the strain at the interface and caused changes in magnetization. The magnetoelectric coupling increased by an order of magnitude compare with that in single-crystals (Vandenboomgaard 1976). The research signified the possibility of creating composite multiferroic by combining single-phase ferromagnetic material and single-phase ferroelectric material through mechanical coupling. The material selection was no longer limited to intrinsic multiferroics.

Current research focuses on the coupling between ferromagnetism and ferroelectricity through strain-mediated interfaces, which spans the variety of potential applications. Strain-mediated magnetoelectric effect has been observed by combining piezoelectric ferroelectric materials with magnetostrictive FM materials in systems such as PZT and Terfonal-D laminates (Dong 2004). In such cases, high magnetoelectric coupling compare with intrinsic material was achieved.

1.6 Strain-Mediated Magnetoelectric Coupling in Multiferroic Composites

Magnetoelectric (ME) coupling of multiferroic composites can be achieved in three major mechanisms. The synergy effect in composites eliminates the harsh requirements in a single compound for multiferroicity, opening the possibility of material combinations. ME coupling is categorized into charge-mediated, strain-mediated, and exchange coupling (Song 2017). In charge-mediated composites, the charge carrier density or the carrier doping level at the interface between FE and FM material. In exchange coupling, the magnetic performance of the FE layer is modified by the voltage-controlled FM domains at the interface between the two layers, as demonstrate in thin film bismuth ferrite (Zhao 2006)

Strain-mediated ME coupling is originated from the deformation of the FM layer transferred from the FE layer by interfacial strain. When magnetic field is applied to a FE-FM composite, ferromagnetic layer experiences the magnetic field and strain is induced due to magnetostrictive effect. The induced strain is transferred to the ferroelectric layer through the interface because they are chemically bonded. The deformation at the interface then induces an electric potential across the ferroelectric layer due to piezoelectric effect. As a result, magnetoelectric effect is observed. A more representative relationship between the ferroic orderings is shown in Figure 1.12. Similarly, in order to control magnetizations by electric field in multiferroic composite for memory applications, the converse ME coupling is considered. When electric field is applied, piezoelectric strain from the ferroelectric layer deforms the ferromagnetic layer and resulted in magnetization changes. By combining a magnetostrictive material and a piezoelectric material, ME coupling can be achieved. Therefore, magnetostrictive and piezoelectric coefficients became the controlling factors of the efficiency of ME coupling.

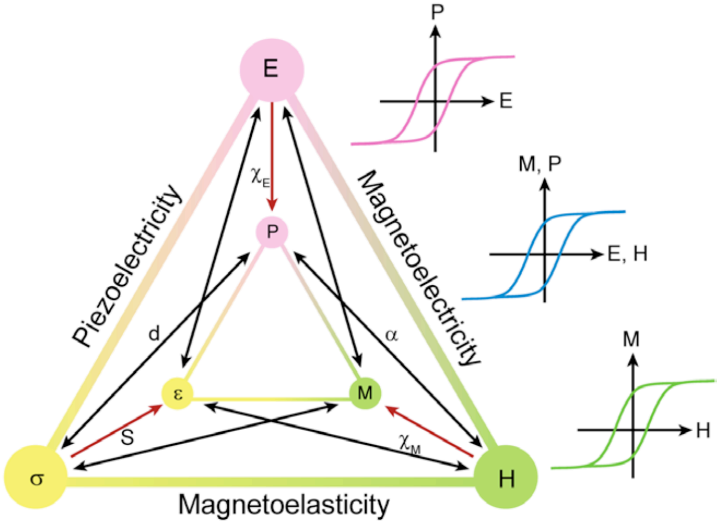

Figure 1.12 Multiferroic hierarchy with interconnected ferromagnetism (FM), ferroelectricity (FE) and ferroelasticity with illustration of strain-mediated magnetoelectric coupling in composite multiferroics (Kim 2015).

On the other hand, nanostructuring plays an important role in enhancing ME coupling. Composite structures were proposed by research community and represented by connectivity of phases, as summarized in Figure 1.13. For example, 0D, 1D, 2D represent nanoparticle, nanowire and planar film respectively; while 3D represents more bulk-like structure. The interfacial area is the highest when nanoparticles are used due to the high surface-to-volume ratio.

Thin films and nanowires structure, on the other hand, provide directionality parallel or perpendicular to the substrate while retaining extensive interfacial coupling.

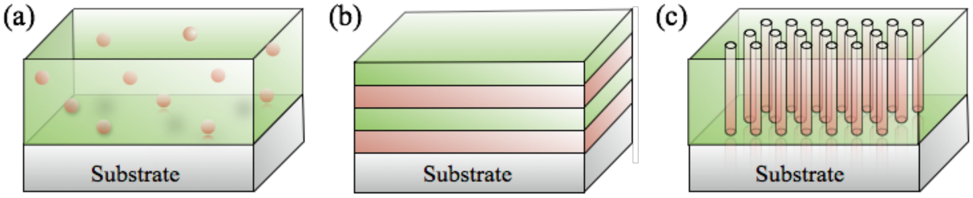

Figure 1.13 Schematic of multiferroic composite structures with (a) 0D-3D, (b) 2D-2D, and (c) 1D-3D connectivities of the two phases (Wang 2010).

Nanoparticle-embedded film, denoted as 0D-3D, is synthesized through chemical solution processing such as sol-gel and co-precipitations (Zhang 2005). Although the magnetoelectric coupling has seen improved, pure FE phase with homogenously dispersed FM phase is difficult, owing to high sintering and crystallization temperature such as $BaTiO_3$. Under electric field, percolation and interdiffusion of FM particles allow formation of eddy currents, resulted in leakage current through the composite. The magnetic response in particles could not be aligned coherently and thus diminishes magnetoelectric responses.

Nano-laminates, denoted as 2D-2D, require alternating layering of two phases. Quality of thin films has been increasing due to the advancement of nanofabrication technologies. Physical vapor deposition such as pulse-laser deposition and molecular beam epitaxy were used (Zhang 2008). Extensive studies on various material combinations in 2D-2D form were conducted. (Srinivasan 2001, Srinivasan 2002, Srinivasan 2003, Srinivasan 2004). Although the distribution of phases is better controlled, silicon substrate limits the movement of laminates, reducing the amount of piezoelectric strain (Bichurin 2003). As a result, modified substrates such as $LaNiO_3$ and $SrTiO_3$ were used despite the high cost.

Nanowire-embedded matrix, denoted as 1D-3D, has ordered directional array of rods in a matrix of the second phase. Magnetization direction can effectively align along pillars, maximizing the synergy effect. The substrate clamping effect can be reduced depending on strain orientation, as illustrated by CFO nanopillar embedded in $BaTiO_3$ grown by pulse-laser deposition (Zheng 2004, Zheng 2004). However, fabricating nanopillar array is complex, which was divided into top-down approach and bottom-up approach (Samuelson 2003). Top-down approach utilizes lithography and nano-patterning to selectively etch or deposit specific arrays of material. The method is limited by the resolutions of multiple lithographic steps and lift-off damages. Bottom-up approach requires spontaneous or catalytic-driven self-assembly of molecules. The fundamental understanding of reaction chemistry in a particular system becomes inevitable. Self-assembling synthesis, however, opened the opportunity to create highly ordered nanorods that traditional top-down approach could not achieve.

In the case of multiferroic composites, whose interfacial interactions are coupled between FE and FM phases, the coupling can be expressed using Green's Function as (Nan 2005),

$$\begin{cases} \sigma = c\mathbf{S} - d^T\mathbf{E} - c\mathbf{S}^{ms} - \sigma_s \\ \mathbf{D} = d\mathbf{S} + \varepsilon\mathbf{E} + \alpha\mathbf{H} + \mathbf{P}_s \\ \mathbf{B} = \mu(\mathbf{S},\mathbf{E},\mathbf{H})\mathbf{H} + \mathbf{M}_s \end{cases} \tag{1.9}$$

where c is stiffness, and the superscript ms represents the strain caused by magnetostriction. The difference between the equations from calculations of bulk material is the residual properties such as strain (σ_s), polarization (P_s) and magnetization (M_s) remain in thin films after external stresses is removed. Under static equilibrium, the differential change of equation (1.9) with respect to dimension equals to zero. Each equation can be expressed by Green's function of a homogenous medium relative to a reference state. The magnetic field induced polarization under strain is,

$$\begin{aligned}\mathbf{P} = (1-f)\left\{\mathbf{P}_s + \left(\varepsilon^p - \varepsilon^*\right)\mathbf{G}^\phi\left(\mathbf{P}_s - d^p\mathbf{G}^u\sigma_s^p\right) + \left(d^* - d^p\right)\mathbf{G}^u\left(\sigma_s^p + d^T\mathbf{G}^\phi\mathbf{P}_s\right)\right\} \\ + fd^*\left[\mathbf{I} - \mathbf{G}^u\left(c^m - c^p\right)\right]^{-1}\left(c^m s^{ms} + \sigma_s^m\right)\end{aligned} \tag{1.10}$$

where f is the volume fraction of the FM phase; G_φ, G_u are the Green's functions of displacement and electric potential; the asterisk denotes averaged quantities; and p and m indicates FE and FM phases respectively. In the 2D-2D system, the equation can be elaborated as follows:

2D-2D Type composite:

$$\begin{aligned}\bar{P}_3 &= (1-f)\frac{\varepsilon_{33}^m}{\bar{\varepsilon}_{33}}P_{s3} + \frac{f(1-f)d_{33}^p\varepsilon_{33}^m}{\bar{c}_{33}\bar{\varepsilon}_{33}}\left(\sigma_{33}^p - \sigma_{33}^m\right) \\ \sigma_{33}^{p(m)} &= 2c_{13}^{p(m)}s_{11}^{p(m)} + c_{13}^{p(m)}s_{33}^{p(m)}\end{aligned} \tag{1.11}$$

where σ_{11} is the total in-plane stress and s_{33} is the out-of-plane strain. The equation divides the effective polarization into two parts: the polarization that originates from the FE phase (first term on the right side) and the polarization induced from the differential stress between the piezoelectric and magnetostrictive responses.

However, for 2D-2D type structures, the in-plane strains are limited due to substrate clamping. It describes the small change in strain of the substrate at the interface due to the volume difference between the substrate and the deposited thin film, which leads to a limited strain in the thin film. This detrimental effect from the substrates in ME coupling was illustrated in nanobilayers of $NiFe_2O_4$ and PZT on MgO substrate, as shown in Figure 1.14. The ME coupling coefficient of the composite peaked at about 10% PZT volume fraction. With a free-standing 2D-2D structure, the direct ME coupling coefficient could reach 1600 mV/cm-Oe. However, when the MgO substrate contributed to 90% of the total volume, the ME coefficient decreased by two orders of magnitude, resulting in a significantly reduced ME coupling (Petrov 2007). In the case of nanobilayers, the composite volume contributes less than 0.1% of the total volume, therefore the ME coupling becomes negligible. It was experimentally demonstrated in 2D-2D $BaTiO_3$/CFO nano-laminates (2 nm individual layer thickness) with the highest direct

ME coupling of 20 mV/cm-Oe (Ren 2009), which has the same order of magnitude of bulk multiferroic composites (Zhai 2003).

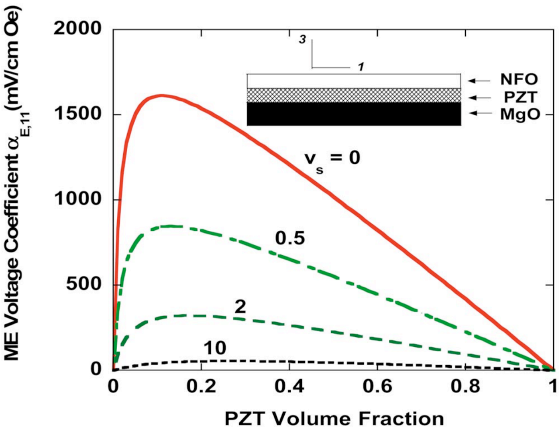

Figure 1.14 Simulated ME coefficient of 2D-2D $NiFe_2O_4$-PZT on planar MgO substrate as a function of MgO-composite volume ratio (v_s), and PZT volume fraction (Petrov 2007).

With the extension in the perpendicular dimension of the substrate to avoid substrate clamping, 1D-3D structure was proposed as a better candidate for ME coupling enhancement. The major difference between the two structures is the strain balance. In 1D-3D structure, the out-of-plane strains in both phases are equal and were used as the boundary conditions of continuity at the vertical interfaces. With the aid of structural symmetry, equation (1.10) can be rewritten as:

1D-3D Type composite:

$$\bar{P}_3 = (1-f)P_{s3} + \frac{2f(1-f)d_{31}^p}{f\left(c_{11}^p + c_{12}^p\right) + (1-f)\left(c_{11}^m - c_{12}^m\right) + c_{11}^p - c_{12}^p}\left(\sigma_{11}^p - \sigma_{11}^m\right)$$
$$\sigma_{11}^{p(m)} = (c_{11}^{p(m)} + c_{12}^{p(m)})s_{11}^{p(m)} + c_{13}^{p(m)}s_{33}^{p(m)} \tag{1.12}$$

The formulation demonstrated the effectiveness of 1D-3D nanostructuring in enhancing ME coupling. Figure 1.15 shows the calculated result that the induced polarizations of the $BaTiO_3$/CFO 1D-3D structure were increased by an order of magnitude to ~400 μC/m^2 by reducing the critical dimensions of the composite from orders of microns to 30 nm (Nan 2005).

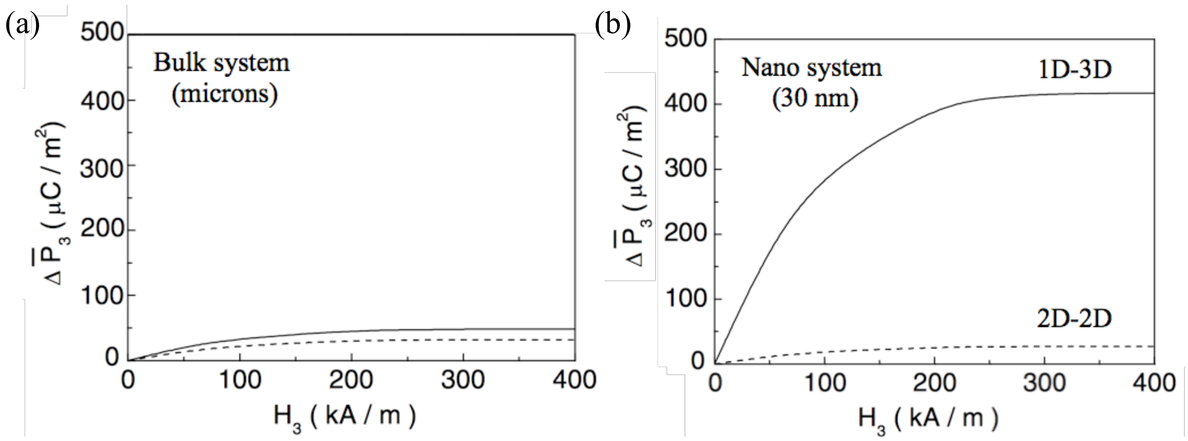

Figure 1.15 ME coupling response of $BaTiO_3$/CFO composites perpendicular to the substrate of (a) bulk systems and (b) nanostructured nano-systems as a function of applied magnetic field. The 1D CFO was 30 nm in diameter and 400 nm in height, while 2D layers were 30 nm in thickness (Nan 2005).

By further engineering the 1D-3D structure, the ME coupling can be tuned and enhanced by optimizing the geometric factors such as the nanopillar aspect ratio, the ferroelectric-ferromagnetic volume fraction, and the nanowire structure. The effect was demonstrated in simulating 1D $NiFe_2O_4$ nanopillars in 3D PZT matrix on planar MgO substrate, as shown in Figure 1.16(a) (Petrov 2007). It suggested that nanopillars with aspect ratios of about 1 could achieve a direct ME coefficient value of 1100 mV/cm-Oe, which is two order of magnitude higher than that of the 2D-2D structure, on a substantially thicker substrate. Increase in aspect ratio increases the maximum ME coefficient partially due to shape anisotropy and reduced substrate effect. In the case of $NiFe_2O_4$/PZT nanowires grown on MgO nanowire template, the direct ME coefficient could reach 1000 mV/cm-Oe when the radius of the composite nanowire was twice of the MgO nanowire radius. It should be noted that the simulation of this particular structure applied to 1D-1D nanocomposite system where a perfect PZT-core-$NiFe_2O_4$-shel experiences no substrate effect and therefore substantially increases the direct ME coefficient to 1600 mV/cm-Oe (Petrov 2007).

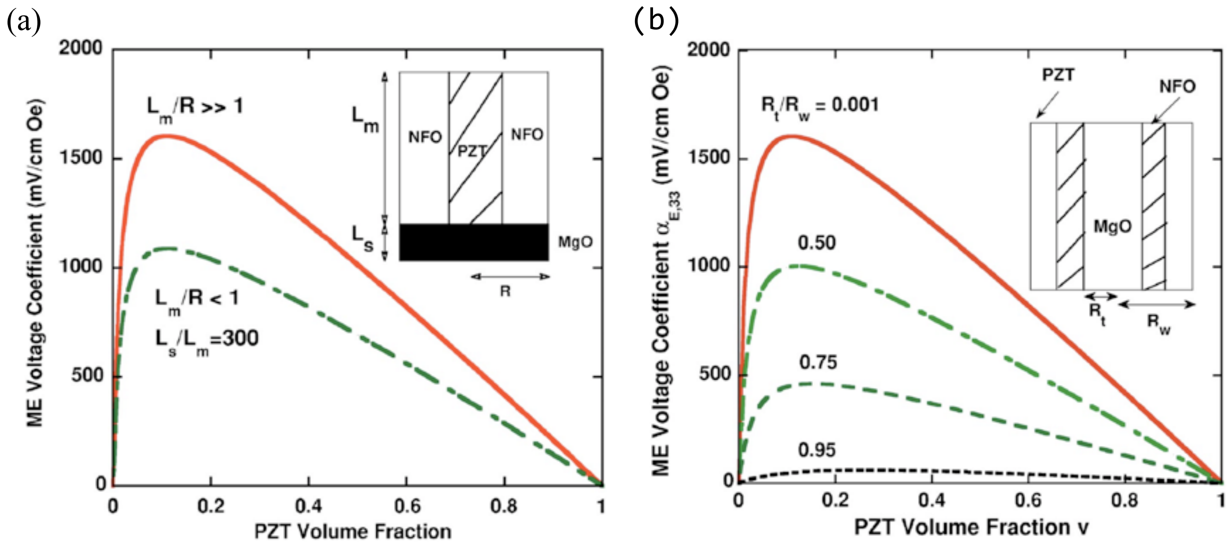

Figure 1.16 ME coefficient of (a) a nanopillar of $NiFe_2O_4$ and PZT of radius *R* and length L_m grown on planar MgO substrate with thickness L_s as a function of aspect ratio (L_m/R); and (b) $NiFe_2O_4$/PZT grown on MgO nanowire of radius R_t with a total radius of R_w as a function of MgO-composite radius ratio (R_t/R_w) and PZT volume fraction (Petrov 2007).

In Table 1.4, different material combinations in various nanostructures were summarized in comparing the effect on ME coefficient. Various FE and FM materials are considered, along with synthetic methods, the geometric types, the reported ME coefficients, and the critical dimensions. The critical dimension of the structure was referred to the total thickness of the multiferroic composite. In the case of 1D-3D structure, the length of the nanopillar was used. The direct ME coefficient of bulk PZT/CFO composite (30 mV/cm-Oe, (Zhai 2003)) is an order of magnitude lower than that in 2D-2D nano-laminates (270 mV/cm-Oe, (Xu 2011)), which agrees with the theoretical results. The majority of the research was performed on 2D-2D systems with different FE and FM material combinations due to the ease of fabrication. The synthetic methods ranges from wet chemical routes to sputtering and pulsed-laser deposition. The direct ME coefficient varies from 20 mV/cm-Oe in $BaTiO_3$/CFO to 300 mV/cm-Oe in PZT/TbDyFe. The high ME coupling in PZT/TbDyFe was attributed to the strong magnetostrictive properties of TbDyFe. When the same material combination such as PZT/CFO is compared between the three different structures, 2D-2D structure as a direct ME coupling of 270 mV/cm-Oe, which is lower than that from 0D-3D and 1D-3D above 300 mV/cm-Oe.

Table 1.4 Direct ME coefficients of strain-mediated multiferroic composite systems with 0D-3D, 2D-2D, and 1D-3D nanostructures

FE	FM	Synthesis	Type (D-D)	ME coef. α_{ME} (mV/cm-Oe)	Critical Dimension (nm)	Reference
PZT	CFO	Solid-state Reaction	Bulk	30	2 mm	(Zhai 2003)
$BaTiO_3$	CFO	Molten Salt	Bulk	17	1.5 mm	(Nie 2009)
PZT	CFO	PLD	0-3	50	150	(Wan 2007)
PLT	CFO	Sol-gel	0-3	250	700	(Roy 2011)
PZT	CFO	Sol-gel	0-3	320	400	(Wan 2005)
$BaTiO_3$	CFO	Sol-gel	2-2	20	>500	(Ren 2009)
BNT	CFO	Spin-coating	2-2	34	220	(Zhong 2007)
PZT	$Tb_{0.3}Dy_{0.7}Fe_2$	Sputtering	2-2	150	800	(Cibert 2013)
PLT	CFO	Sol-gel	2-2	200	700	(Roy 2011)
PZT	CFO	Sol-gel / Sputtering	2-2	240	150	(Sim 2008)
PZT	CFO	Sol-gel	2-2	270	580	(Xu 2011)
PZT	LSMO	PLD	2-2	300	273	(Tang 2013)
PZT	CFO	PLD	1-3	390	100	(Wan 2007)

* BNT = $Bi_{3.15}Nd_{0.85}Ti_3O_{12}$; PLT = $Pb_{0.85}La_{0.15}TiO_3$; LSMO = $La_{0.67}Sr_{0.33}MnO_3$

It is clear that a well-coupled interface is important to enhance the magnetoelectric effect in nanostructures of large surface areas. In order to synthesize nanoscale multiferroic composites with complex structures, atomic layer deposition is a suitable candidate as the conformal growth ensures a well-coupled interface. The precise thickness control would allow the study of ME coupling as a function of material thicknesses as well as the nanostructure such as nanotubes and nanowires.

In order to optimize ME coupling between FE and FM materials, the choice of the materials is dictated by 3 factors: the ability to react to strain, interfacial coupling, and synthesis viability in complex structures. The ability to react to strain is defined by the piezoelectric and magnetostrictive coefficients. They should be maximized and at the same time have the same order of magnitude in both phases to prevent formation of cracks at the interface. According to Table 1.2 and 1.3, Terfenol-D has a magnetostrictive coefficient of 1200 με in compare to -164 με from CFO. On the other hand, lead-based ferroelectrics such as PZT, PMN-PT, and PZN-PT with piezoelectric coefficients of 500, 2000, and 2500 pm/V respectively are also potential candidates. In terms of interfacial coupling of the two phases, the formation of an interfacial oxide layer should be avoided due to the build-up of oxygen vacancies, which act as charge barrier when electric field is applied. The disrupted surface also facilitates the formation of impurity oxide phases. Terfenol-D, like many metals and intermetallics, has spontaneous formation of native oxide, which is not suitable for interfacing with ferroelectric oxides. Among ferromagnetic oxides, CFO has the highest magnetostrictive coefficient, and therefore became the materials of choice. In terms of synthesis viability in complex 1D-3D structures, PMN-PT and PZN-PT are deemed hard to control due to the number of constituent oxides involved. Defects are prone to form at interfaces when the large unit cell cannot be formed in nanoscale. Atomic layer deposition, which is ideal for growth on complex structures, would not be practical to growth the two materials. PZT, on the other hand, is widely studied as a piezoelectric material and was successfully deposited using atomic layer deposition (Zhang 2011, Choi 2013). It became the ferroelectric candidate for the nanostructured multiferroic composite.

In order to implement multiferroic composite into memory devices, the characterization of electric field controlled magnetism, namely the converse ME coefficient, becomes the figure of merit. Table 1.5 summarizes the research on converse ME coupling. In contrary to Table 1.4, the magnetization is measured as a function of electric field. The converse ME effect was weak in the 2D-2D structure such as PMN-PT/CFO nanocomposite due to substrate clamping. The converse ME coupling was measured to be 3.2×10^{-6} (Peng 2015). With the increased of surface area between the two phases, 0D-3D structures had an increased coupling of 1×10^{-5} in mesoporous PZT/CFO composite (Chien 2016). On the other hand, the converse ME coefficient was found to be 4×10^{-5} Oe-cm/mV in a 1D-3D CFO/PZT composite due to both surface effects and reduction in substrate clamping (Ren 2008). In this work, the research goal is to enhance the converse ME coefficient of the multiferroic composite beyond 4×10^{-5} Oe-cm/mV through nanostructuring the ferromagnetic and ferroelectric phase, as well as optimization of the interfacial coupling between the two phases.

Therefore, this work focuses on the goal in the fabrication 1D CFO nanotubes and nanowires, 0D-3D CFO/PZT mesoporous composite, and 1D-1D CFO/PZT core-shell nanowire composite. The effects of nanopillars aspect ratios, volume fraction, and core-shell structure on the ME coupling effects are quantified by determining the converse ME coupling coefficient.

Table 1.5 Converse ME coefficients of strain-mediated multiferroic composite 2D-2D and 1D-3D nanostructures

FE	FM	Type (D-D)	ME coef. α_{CME} (Oe-cm/mV)	Critical Dimension (nm)	Reference
BTO	Ni	2-2	5×10^{-10}	100	(Gepras 2010)
BFO	CoFe/Cu/CoFe	2-2	3×10^{-5}	100	(Heron 2014)
BTO	LSMO	2-2	2.3×10^{-5}	40	(Eerenstein 2007)
PMN-PT	LSMO	2-2	6×10^{-6}	20-50	(Thiele 2007)
PMN-PT	Fe_3O_4	2-2	6.7×10^{-5}	900	(Liu 2009)
PMN-PT	CFO	2-2	3.2×10^{-6}	200	(Yang 2009)
PZT	CFO	0-3	1.1×10^{-6}	100	(Peng 2015)
PZT	CFO	0-3	1×10^{-5}	6	(Chien 2016)
BFO	CFO	1-3	1×10^{-5}	200	(Zavaliche 2005)
PZT	CFO	1-3	4×10^{-5}	80	(Ren 2008)

CHAPTER 2 Experimental Methods

This chapter illustrates the synthesis and characterization methods used to examine multiferroic nanocomposite and the effect of magnetic shape anisotropy on magnetoelectric coupling. The chapter first describes material of choice and various synthesis methods used in the study, including the experimental parameters such as deposition temperatures and precursor concentrations. The two architectures, 0D-3D and 1D-1D, are discussed . Characterizations of the as-synthesized materials are detailed including the morphologies, crystal structures, and multiferroic properties.

2.1 Synthesis of Material of Choice

The material of choice in this work is ferromagnetic CFO and ferroelectric PZT. As mentioned in Chapter 1.6, the dictating factors of choosing the materials were the magnetostrictive coefficient and piezoelectric coefficient to maximize the strain transfer between the two phases through interfacial coupling and nanostructuring. Both PZT and CFO are exceptional in their strain responses, as well as a high resistivity. PZT has a piezoelectric coefficient of 2000 pm/V and CFO has a negative magnetostriction of -164 με. The resistivity of CFO was 10^{10} μΩ-cm and the relative dielectric constant of PZT was 300.

CFO has a cubic inverse spinel crystal structure, as shown in Figure 2.1. The lattice parameter is 8.39 Å. In a normal spinel structure such as the mineral $MgAl_2O_4$ (AB_2O_4), the A^{2+} ion occupies 1/8th of the tetrahedral sites while the B^{3+} ion occupies half of the octahedral sites in the structure. The oxygen atoms are arranged in cubic closed packed structure. In an inverse spinel structure, A (Co^{2+}) ions occupy the octahedral sites while half of the B (Fe^{3+}) ions occupy the tetrahedral sites and the other half occupies the octahedral sites. Due to the exchange interactions of magnetic spins between both sites, the spins are aligned in an antiparallel fashion.

In the case of CFO, the spins originate from the Fe ions are cancelled. However, the spins from the Co^{2+} ion remains, giving rise to the magnetic properties of CFO. The antiparallel, non-zero cancelling of spins is known as ferrimagnetism. At elevated temperature beyond the Curie temperature at 870K, the ferrimagnetism becomes paramagnetic due to the dominating thermal effects over spin couplings.

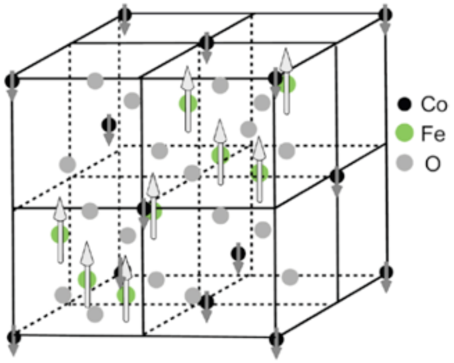

Figure 2.1 Schematic of cubic spinel structure of CFO (a = 8.39 Å).

PZT has a perovskite structure as described in Chapter 1.4. The Pb ion has a simple cubic structure with a Zr or Ti occupying the cubic center. The oxygen atoms form an octahedral around the center Zr or Ti atom as shown in Figure 2.2(a). Perfect cubic perovskite structure does not give ferroelectricity due to the centrosymmetric nature of the structure. Rhombohedral and tetragonal structure are common transitions from the cubic structures such as PZT. It has a rhombohedral structure when the structure is zirconium rich, whereas a tetragonal structure when it is titanium rich, as shown in Figure 2.2(b). The transition between the two phases occurs at a Ti-to-Zr ratio of 48:52 at room temperature, known as the morphotropic phase boundary. At this morphotropic boundary, PZT exhibit a higher dielectric constant as well as enhanced piezoelectric and ferroelectric effects (Pulskamp 2012). Increased number of ferroelectric domain orientations in both phases gave rise to the enhanced effect. At elevated temperature at 630K, the phase transition from tetragonal to cubic and becomes paraelectric.

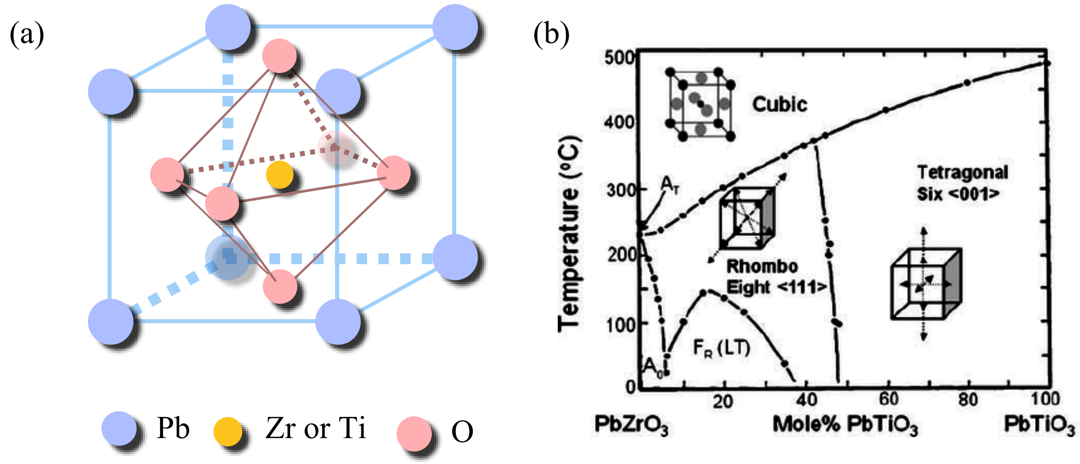

Figure 2.2 (a) Schematic of perovskite structure of PZT with a lattice spacing of 3.91 – 4.04 Å and (b) phase diagram of PZT system with transitions between cubic, rhombohedral and tetragonal structures (adapted from (Shrout 2007)).

2.2 Atomic Layer Deposition (ALD)

Atomic layer deposition (ALD), also known as atomic layer epitaxy (ALE), is typically referred to the binary chemical half-reaction sequence where the surface reaction of each chemical is self-terminating. Each step must be dominant and lead to monolayer saturation. The high conformality and uniformity makes ALD a suitable technique for research purposes.

In depositing a metal oxide, a metal-containing precursor ML_x is used. Water is the oxidizing agent to react with the precursor to form metal oxide, $MO_{x/2}$. The overall reaction of these two reactants is given by,

$$ML_x + {}^{x}\!/_{2}\,H_2O \longrightarrow MO_{x/2} + xLH \tag{2.1}$$

Single gas-phase precursor (MLx) is introduced and allowed to react with surface hydroxyl groups, generating volatile hydrolyzed ligands (LH). The reaction proceeds to completion when initial surface functional groups are consumed and replaced by ligands from metallic alkoxyl precursors, as shown in Figure 2.3.

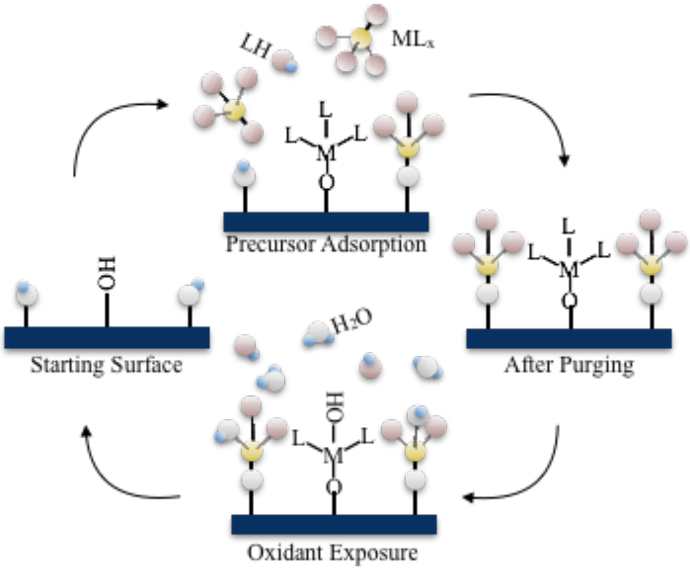

Figure 2.3 Schematic of atomic layer deposition half-cycle reactions

While the precursor does not react with the new surface, the half reaction is self-limiting. The growth of thin films beyond one monolayer become less possible once all the surface functional groups are reacted.

$$R-OH+ML_x \longrightarrow R-OML_{x-1}+LH \tag{2.2}$$

After the first half-reaction, the substrate surface is covered with extra ligands that protect the underlying oxide to react with other molecules. Water is introduced in the second half-reaction. The metal-ligand bond is replace by a hydroxyl group, revealing the same functional group as what it was started.

$$RO-ML_{x-1}+(x-1)H_2O \longrightarrow RO-M-(OH)_{x-1}+(x-1)LH \tag{2.3}$$

When precursor vapor pressure increases, deposition rate increases due to a higher concentration of reactants supplied to the substrate surface in alternating pulses. In ideal situation, an optimal temperature range, known as ALD window, should be observed as a proof of the process, as shown in Figure 2.4. Such temperature range dictates equilibrium between precursor adsorption and desorption rate. It can also view as the optimal energy to overcome reaction activation barrier before decomposition of precursor.

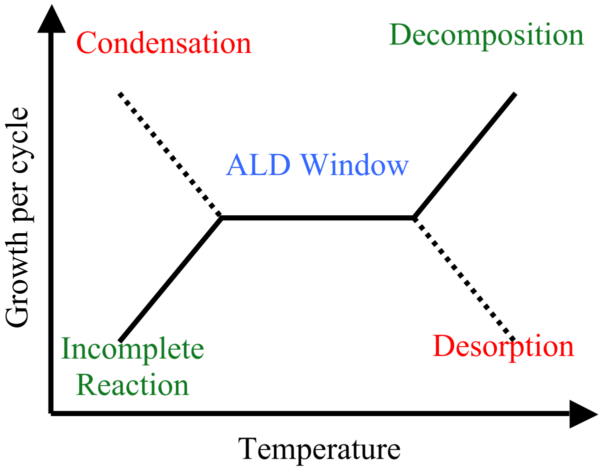

Figure 2.4 Schematic of the atomic layer deposition window with condensation and desorption regimes

Specifically, a radical enhanced atomic layer deposition (RE-ALD) system was used in this work to synthesize CFO and PZT, where the thin film deposition was carried out in a custom vacuum system that consist of a reaction chamber and a designated load-lock chamber for sample transfer. The main chamber was maintained at ultra-high vacuum (~10^{-6} Torr) using a CTI-Cryogenics pump with a pumping speed of 4000 L/s without exposing to ambient to minimize atmospheric contamination.

Table 2.1 Temperature window of ALD of CFO (Pham 2015)

Chemicals	With H2O (°C)	With Oxygen Radicals (°C)
$Fe(TMHD)_3$	160–210	190–230
$Co(TMHD)_2$	114–307	190–230

Due to the non-overlapping thermal deposition windows between precursors as shown in Table 2.1, oxygen radicals were introduced to facilitate growth. Oxygen radicals were generated inside a quartz cavity using a 2.46 GHz Sairem microwave power source at 25 W and a constant oxygen flow at 0.6 sccm.

Metal beta-diketonate (TMHD) precursors and other chemicals used in this study are listed below in Table 2.2. The bulky ligand, 2,2,6,6-tetramethyl-3,5-heptanedionato, is chosen as it retains high thermal stability at elevated temperatures in compare with butyl and isopropyl ligands. The $Fe(TMHD)_3$ and $Co(TMHD)_3$ precursors were sublimed at 120°C and 130°C respectively. The sublimed precursors were delivered to the sample surface through precursor dosers. The sample stage was heated at 200°C during deposition. Three different substrates were used in this study: (001)-oriented SrTiO3 (MTI Corp.) for thin film depositions, AAO membranes (Synkera Technologies, Inc.) for 1D nanostructure fabrications, and mesoporous PZT. Deposited thin films were subsequently annealed at 650°C under oxygen ambient for 60 seconds with a ramp rate of 50 °C/s for crystallization using AccuThermo AW 610 RTP furnace.

Table 2.2 List of chemical precursors and process gases used this work

Chemicals	Melting Point (°C)	Decomposition Temp. (°C)	Vendor	Purity
$Pb(TMHD)_2$	129-133	280	Strem Chemicals	99%
$Zr(TMHD)_4$	157-171	300	Strem Chemicals	99%
$Ti(O\text{-}i\text{-}Pr)_2(TMHD)_2$	171-185	240	Strem Chemicals	99.99%
$Fe(TMHD)_3$	164	-	Strem Chemicals	99.9%
$Co(TMHD)_2$	143	250	Strem Chemicals	99.9%
H_2O	0	-	-	-
N_2	-	-	Airgas	99.999%
O_2	-	-	Airgas	99.999%

* TMHD = 2,2,6,6-tetramethyl-3,5-heptanedionato

Using RE-ALD, the growth rate, composition and crystallinity of CFO were first studied. Different thicknesses of CFO were deposited on (001)-oriented $SrTiO_3$ in order to establish the growth rate. The thickness was determined using J. A. Woollam M-88 spectroscopic ellipsometer. The growth rate was calculated to be 2.41 Å/cycle. The composition was confirmed to have the correct stoichiometric ratio of CFO, as shown in the inset of . In addition, 50 nm of CFO were annealed in oxygen ambient at 450°C to 750°C for 60 s. At 450°C, no peak was observed originated from CFO. After annealing at 550°C, a broad CFO (004) peak became apparent from inverse spinel structure, that the unequal spins between cobalt and iron at octahedral sites gave rise to the ferrimagnetic properties (Zaliznyak 2007), indicating the formation of small grains. Further annealing at higher temperatures decreased the full-width-half-maximum (FWHM) of the peak, resulting from grain growths.

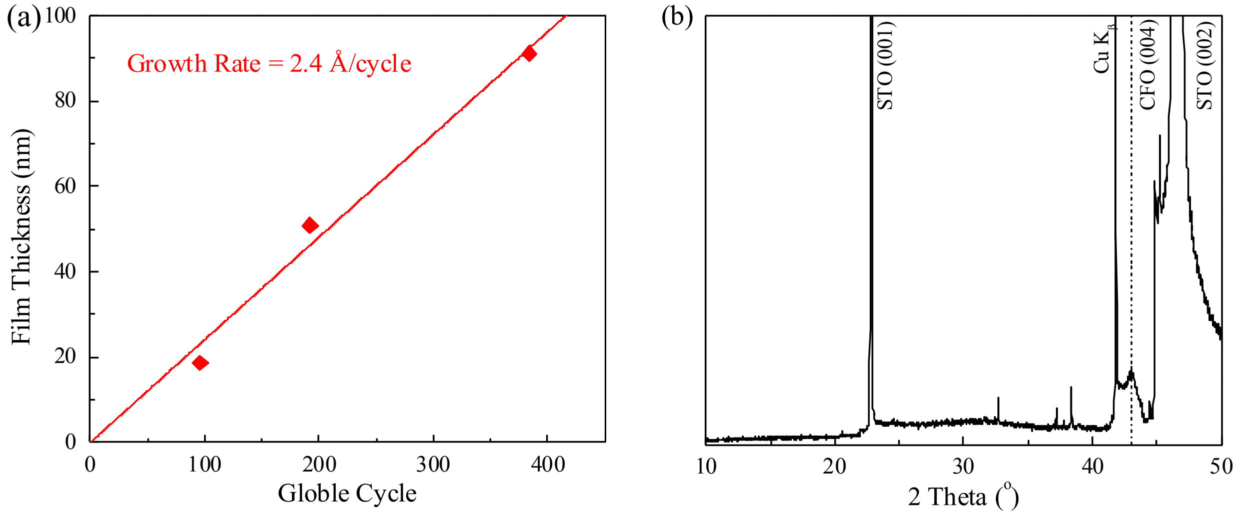

Figure 2.5 (a) Growth rate of RE-ALD of $CoFe_2O_4$ on (001)-oriented $SrTiO_3$ and (b) crystallinity of the sample after annealing at 550°C (Pham 2015).

For the deposition of ferroelectric PZT, precursors were pulsed sequentially as $n[-a(\text{-Pb-}H_2O\text{-})\text{-}b(\text{-Ti-}H_2O\text{-})\text{-}a(\text{-Pb-}H_2O\text{-})\text{-}c(\text{-Zr-}H_2O\text{-})\text{-}]$, where n corresponds to the number of global cycles; a,b, and c represents the local cycles of each precursor. The stoichiometric ratio of PZT is controlled at the morphotropic phase boundary of $Pb(Zr_{0.52},Ti_{0.48})O_3$ by changing precursor local cycles. At this specific composition, PZT has both the rhombohedral and tetragonal phases, which has increased piezoelectric responses due to the increased allowable domain states from both phases. The lead, zirconium, and titanium precursors were sublimed at 115°C, 200°C, and 130°C respectively. The substrate temperature was heated at 250°C by a boron nitride coated nickel-chromium heater in contact to the platinized silicon substrate.

Similarly, ALD PZT was grown on $Pt/TiO_x/Si$ to verify the growth rate and crystallinity. Thickness calibration of the ALD process is shown in Figure 2.6 with a growth rate of 10.0 Å/cycle. The crystalline phase of the PZT (10 nm) was identified to be perovskite using XRD with compared to JCPDS 00-033-0784.

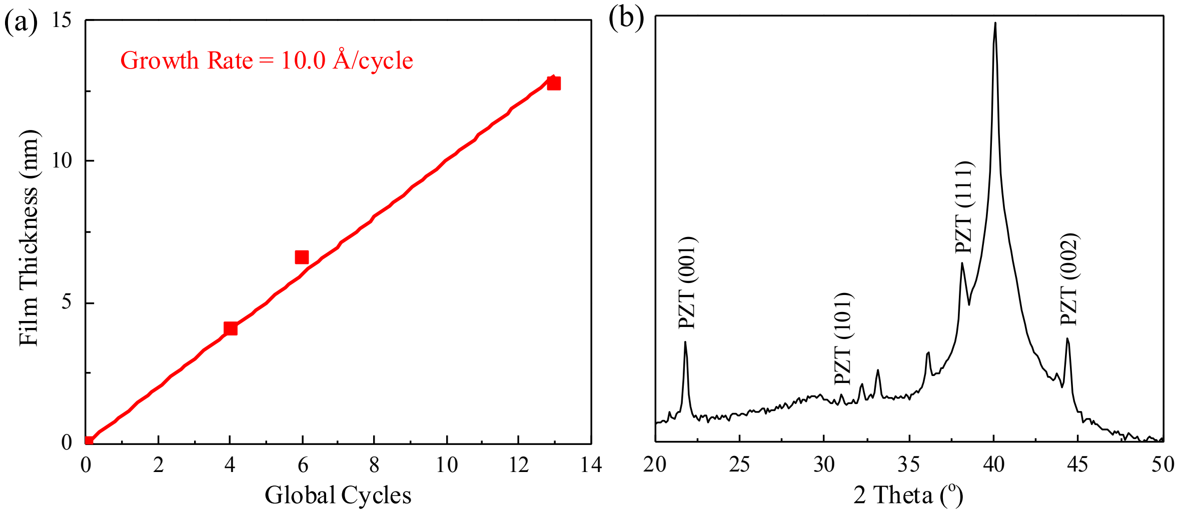

Figure 2.6 The as-deposited PZT thin film on $Pt/TiO_x/Si$ by atomic layer deposition at 250°C had (a) a calibrated growth rate of 10.0 Å/cycle by spectroscopic ellipsometry. (b) Identification of perovskite phase of 10 nm PZT using XRD (Chien 2016).

2.3 1D-1D Architecture

In order to investigate the shape anisotropy as well as effective strain transfer between the ferroelectric PZT and ferromagnetic CFO, a highly directional 1D-1D core-shell structure is chosen to elucidate the effect of strain-induced shape anisotropy

Anodic aluminum oxide (AAO) is used as hard physical templates for synthesizing the 1D-1D multiferroic composite. It consists of symmetrical nanoporous architecture with uniform cylindrical pores penetrating the entire thickness of the membrane. The pores are arranged in a hexagonal honeycomb array with a pore size adjustable by electrochemistry, as shown in Figure 2.7. The highly organized porous structure is therefore suitable to fabricate directional CFO-PZT composite.

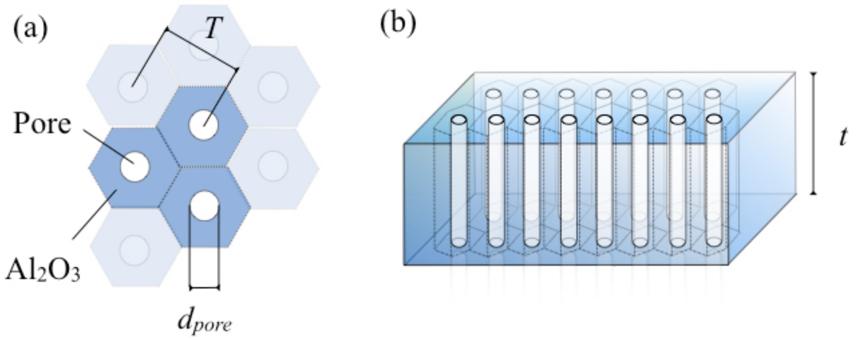

Figure 2.7 (a) Top-down and (b) tilted schematics of anodic aluminum oxide membranes with a thickness t, pore diameter d_{pore}, and pore period T.

In this work, the membranes were purchased from Synkera Technologies, Inc. and summarized in Table 2.3. The membranes are commercially available and inexpensive from various vendors. The diameters of the pores were 18, 35 and 80 nm with a thickness of 50 μm. The pore densities were estimated to be 6×10^{10}, 1×10^{10}, and 2×10^{9} respectively by counting the number of pores in the SEM images using the software ImageJ, which groups dark color pixels within the same pore as one entity and counts the total number of pixel groups.

Table 2.3 Anodic aluminum oxide membrane used in this work (Synkera Technologies, Inc.)

AAO Membrane	1	2	3
Pore Diameter, *d* (nm)	18	35	80
Pore Density (cm^{-2})	6×10^{10}	1×10^{10}	2×10^{9}
Pore Period (nm)	44	94	243
Porosity (%)	15	13	10
Thickness, *t* (μm)	50	50	50
Aspect Ratio	56	29	13

The top-down morphologies of the as-received AAO templates are shown in Figure 2.8. Due to severe charging of the aluminum oxide, 5 nm of Au was deposited by sputtering. Clear pore openings in all three membranes were observed although the hexagonal arrangement was not apparent. From the membrane with the largest pore diameter of 80 nm, multiple pores were observed within a larger opening as an indication of incomplete dissolution of the aluminum oxide during the electrochemical process on the top surface, which is less apparent in membranes with smaller pores. It should be noted the pore wall thickness scale with the pore diameter. The wall thickness of the 80 nm pore was about 100 nm, while that of 18 nm was less than 10 nm.

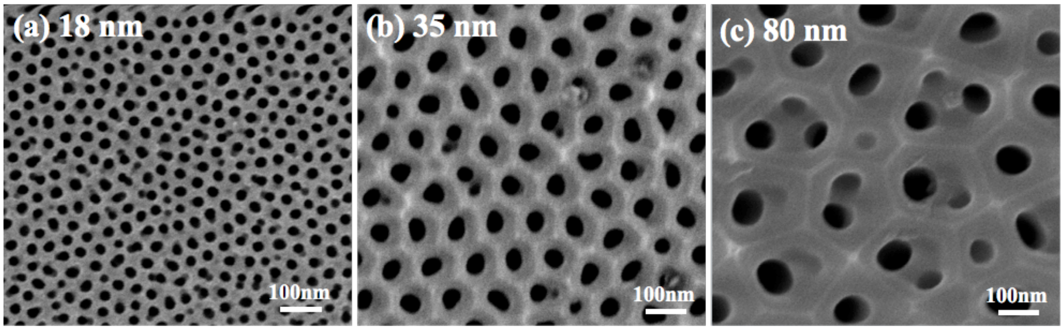

Figure 2.8 Top-down SEM image of anodic aluminum oxide membranes with a thickness of 50 μi, and pore diameter of (a) 18 nm, (b) 35 nm, and (c) 80 nm.

Due to the high aspect ratio of the porous structure, atomic layer deposition is an ideal technique for its uniformity and conformality over complex structures. The infiltration of the membrane using ALD is illustrated in Figure 2.9.

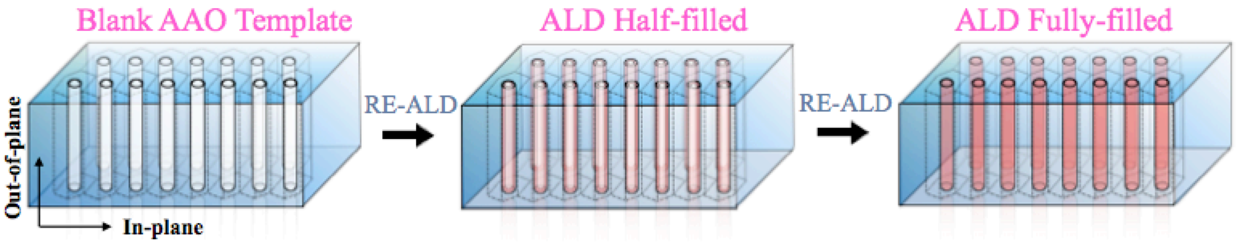

Figure 2.9 Atomic layer deposition of CFO in pore-filling process of the anodic aluminum oxide membranes.

The shape anisotropy is therefore studied as a function of the pore filling, which is defined as the ratio between the ALD deposition thickness and the pore radius. For example, a 20 nm ALD deposition in a 80-nm pore is termed 50% filled.

$$Filling\ \% = \frac{Deposition\ thickness}{Pore\ radius} \times 100\% \tag{2.4}$$

After the growth rate was established, ALD of CFO in AAO membranes was performed. In Figure 2.10, the morphologies of the deposited CFO in AAO with 35-nm pores were observed under SEM at different deposition thicknesses. Pore narrowing is apparent with increasing deposition of the material. When the pores were completely filled, the outline of the porous structure was still apparent due to the conformal coating of ALD as well as the rough top surface

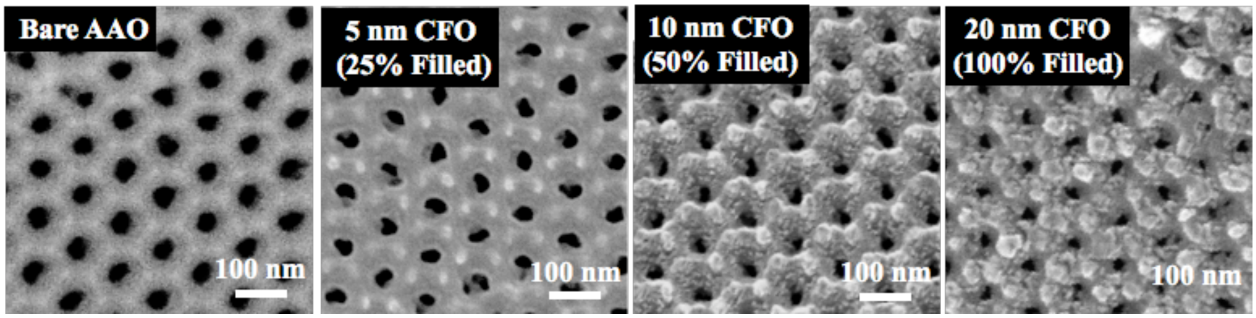

Figure 2.10 Top-down SEM images of deposited CFO in AAO membranes of 35-nm pore with different 0%, 25%, 50% and 100% filling.

2.4 0D-3D Architecture

2.4.1 Mesoporous PZT Template by Evaporation-Induced Self-Assembling (EISA)

To further the investigation of the shape anisotropy as well as effective strain transfer between the ferroelectric PZT and ferromagnetic CFO, a 0D-3D structure is created to elucidate the effect.

A mesoporous template was generated to provide the 0D template, by an evaporation-induced self-assembly (EISA) process which refers to spontaneous aggregation of molecules in specific patterns through weak intermolecular forces such as hydrogen bonding and electrostatic forces (Brinker 1999), (Zhao 2013). Metal alkoxide precursors usually do not have the capability to self-assemble due to their bulky hydrocarbon chains, in which Van der Waals forces dominant. Surfactants, or structure-directing agents (SDA), are added to assist the organization of precursors. Amphiphilic diblock copolymers are typical SDAs, which consist of non-polar hydrophobic head and polar hydrophilic tail. Aggregation of polymers occurs similar to phospholipid in cell membranes depending on the relative concentrations and polarities of solvents. When the concentration of the polymer exceeds a threshold, namely, critical micelle concentration (cmc), the surfactants create micelle structures. Upon evaporation of solvents, the relative concentration of the SDA increases and eventually exceeds cmc, resulting in self-assembly. The formation of micelles is originated from hydrophobic-hydrophilic nature of surfactants. Hydrophilic parts are directed toward polar solvent reservoir due to hydrogen bonding, whereas hydrophobic parts are directed away from the solvent. Spherical micelles can then be formed by spatially separating polar and non-polar parts. The structure gives the lowest surface energy and thus thermodynamically stable. Further evaporation of solvent drives the evolution of micelles into various patterns. Figure 2.11 shows various structures of the self-assembling agent cetrimonium bromide (CTAB). Phase diagram of SDA contains valuable information of critical micelle temperature, concentration and various structures. In general, SDA with low cmc value (0-30 mg/L) gives more distinct orderings.

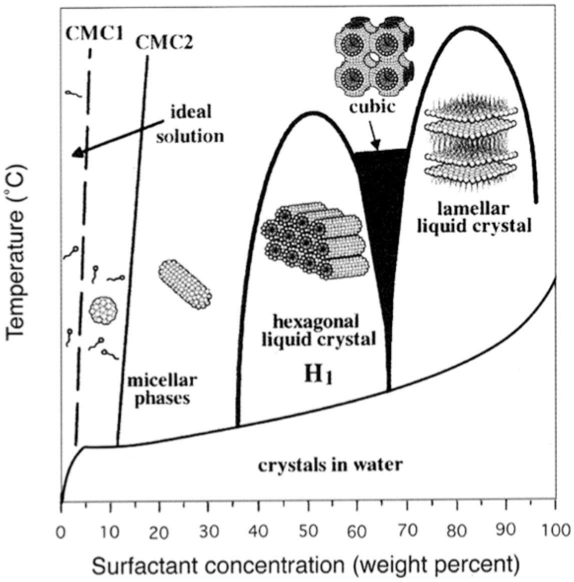

Figure 2.11 CTAB self-assembly structures upon solvent evaporation (Raman 1996).

In this work, mesoporous PZT was synthesized by following sol-gel process with addition of amphiphilic diblock copolymer (Reitz 2014). Amphiphilic diblock copolymer, poly(butadiene (1,4 rich))-*block*-poly-(ethylene oxide) (PBd-*b*-PEO), with a mass ratio of PBd(5500)-*b*-PEO(7500), was purchased from Polymer Source Inc.. This PBd-*b*-PEO solution was dissolved in 1 mL of warm ethanol. Once the PZT precursor solution was homogeneous after the addition of glacial acetic acid to slow down phase segregation and gel formation, the PBd-*b*-PEO solution was added and allowed to clarify by magnetic stirring for 1 h. Films were dip-coated from the solution onto platinized silicon wafers in a humidity-controlled chamber set to 10–20% relative humidity. During the synthesis, amphiphilic diblock copolymer segregated the organic and the inorganic phase. Polar ethylene oxide aggregates with metal oxide and hydroxide, while the lipophilic butadiene hydrocarbon chain aggregates itself, resulted in the formation of two continuous and intertwined networks within the dip-coated film. To form rigid inorganic/organic structures, the films were calcinated in air at 80 °C for 6 h, at 130 °C for 8 h, and at 180°C for 6 h for a total heating time of 24 h including temperature ramps. The network of the hydrocarbons was burnt off during the calcination step, leaving a porous structure of amorphous PZT. Finally, the PZT is crystallized at 700°C in air for 4 minutes with a ramp rate of 12°C/s using MPTC RTP 600xp rapid thermal annealing furnace. Figure 2.12 shows the morphology of the as-deposited and annealed PZT with a pore neck diameter of 20 nm. The PZT thickness was 100 nm and was controlled by the viscosity of the solution and the dip-coating retract rate. The top surface was covered by organics before annealing, after which the mesoporous structure was apparent. Some degree of sintering effect was also observed from the larger grains.

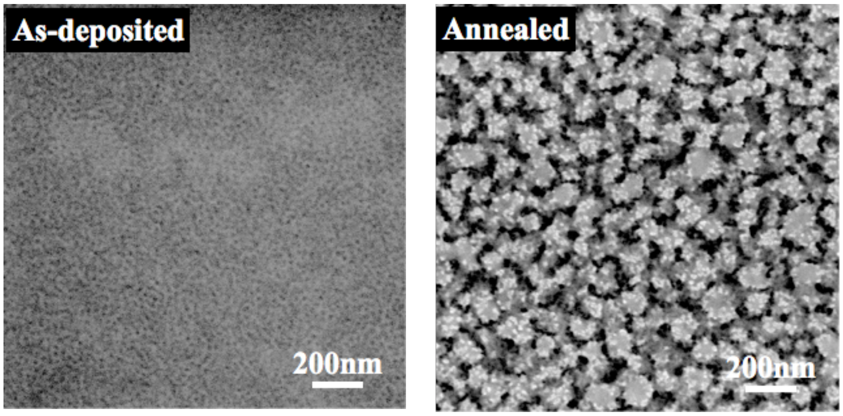

Figure 2.12 SEM Top-view morphology of 100 nm dip-coated mesoporous PZT template with pore neck diameter of 20 nm before and after annealing at 700°C in air for 4 minutes with a ramp rate of 12 °C/s.

Due to the high porosity of the interconnected pores, atomic layer deposition is an ideal technique for its uniformity and conformality over this complex structure. The infiltration of the mesoporous template using ALD is illustrated in Figure 2.13.

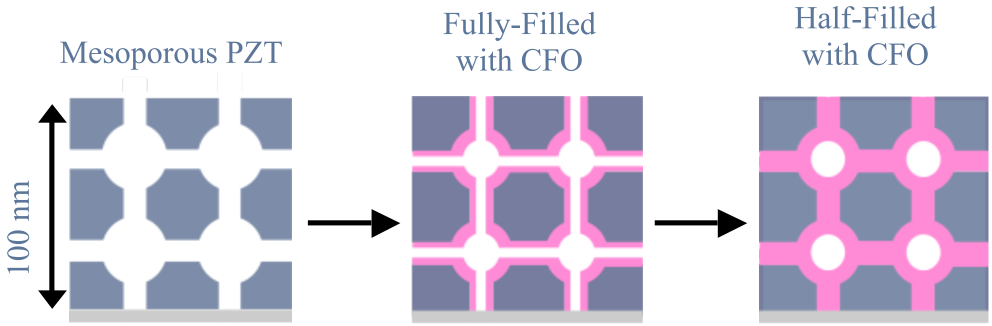

Figure 2.13 Atomic layer deposition of CFO in pore-filling process of 100 nm of mesoporous PZT.

The annealed mesoporous PZT template structure was then filled with ALD CFO in synthesize a complete 0D-3D multiferroic composite. The degree of filling, “Filling %,” was defined by the ratio of ALD CFO thickness and pore neck radius:

$$Filling\ \% = \frac{Deposition\ thickness}{Pore\ neck\ radius} \times 100\% \tag{2.5}$$

For example, 5 nm of ALD CFO deposited into the mesoporous PZT structure that has a pore neck radius of 10 nm would be referred as “50% filled.”

2.5 Material Characterizations

The surface morphology was characterized using Hitachi S4700 scanning electron microscopy (SEM). The film composition was analyzed using Kratos Analytical Axis Ultra DLD X-ray photoelectron spectrometer (XPS). X’pert Pro PANalytical Powder X-ray Diffractometer (XRD) and Stanford Synchrotron Radiation Lightsource (SSRL) beamline 7-2 were used for determining crystal structure and lattice spacing. MPMS superconducting quantum interference device (SQUID) was used for magnetic properties respectively. Bruker Dimension Icon Scanning Probe Microscope was used for measuring surface roughness, piezoresponse and magnetic domains. An *ex-situ* electrical poling setup was used to bias the multiferroic composite for measuring converse ME coefficients.

2.5.1 X-ray Photoelectron Spectroscopy (XPS)

X-ray Photoelectron Spectroscopy (XPS) is one of the photoelectron emission methods used to identifying most elemental compositions except light atoms such as hydrogen. The X-ray penetration depth is approximately 10 nm due to the escape length of photoelectrons from the sample surface. (Vickerman 2009)

The fundamental processes in photoelectron spectroscopy are based on photoelectric effect, in which electrons are ejected through the absorption of quantized energy packet hν provided by incident X-ray.

Aluminum and magnesium are commonly used to generate X-rays by bombardment of high-energy electrons. Core electrons of heavy metals on the K level are ejected, leaving a hole in the electron level. Electrons from higher energy state drop down to fill the vacancy and release energy as electromagnetic waves. $K_{\alpha lum}$ X-rays are produced during the process, where $K_{\alpha X}$ corresponds to a $2p_{1/2}$ /2rresponds to a 2d $d_{\alpha/}$ corresponds to a $2p_{3/2}$ /2r*s* transition. The energy is concentrated at 1486.6 eV as shown in Figure 2.14.

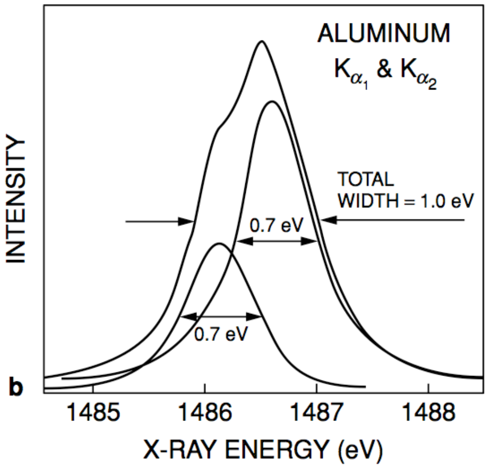

Figure 2.14 Schematic of X-ray generation from high-energy electron bombardment with corresponding Aluminum Kα emission (Siegbahn 1967).

The kinetic energy of the ejected electrons can be calculated through conservation of energy. The photon energy is contributed to the kinetic energy and the binding energy of the electrons. The binding energy is the energy required to remove an electron from the *n*-th energy level to the vacuum level in gases, or Fermi level in solids, with zero kinetic energy. In the case of electrical contact between the spectrometer and the specimen, the two Fermi levels are aligned under thermodynamic equilibrium, as shown Figure 2.15. The energy balance can be described by,

$$h\nu = E_{kin}^{'} + \phi_{spec} + E_{Fermi} \tag{2.6}$$

where the work function of the spectrometer is equipment specific.

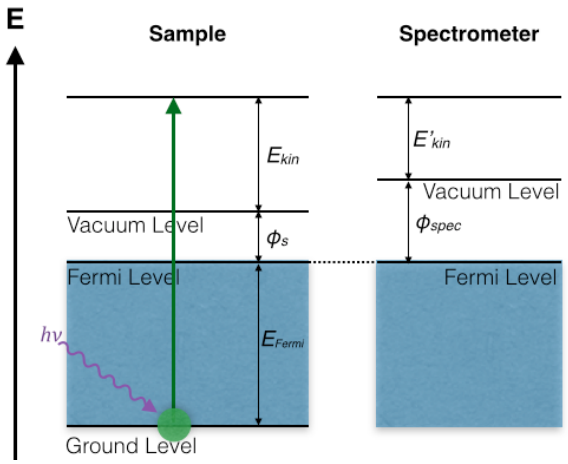

Figure 2.15 Schematic of band diagram in X-ray photoelectron spectroscopy

Table 2.4 shows the binding energies of the selected elements in this work, along with their spin orbital splitting, intensity ratios, and relative sensitivity factor (RSF). During data analysis, carbon 1*s* reference peak at 284.6 eV is used to account for binding energy changes caused by local chemical shifts. The peaks are chosen such that the overlapping of peaks are avoided. The standard values are extracted from the National Institute of Standards and Technology (NIST) database.

Table 2.4 XPS binding energies of selected elements of interest in this work

Element	Peak	Binding Energy (eV)	RSF	Spin-Orbital Splitting (eV)
O	1*s*	529.2	0.78	-
C	1*s*	284.6	0.278	-
Pb	$4f_{7/2}$	138.4	8.329	4.87
Zr	$3d_{5/2}$	178.9	2.576	2.4
Ti	$2p_{3/2}$	454.1	2.001	6.1
Co	$2p_{3/2}$	778.2	3.59	14.99
Fe	$2p_{3/2}$	706.7	2.957	13.1

The binding energies of elements are prone to be shifted due to various bonding states of atoms and chemical environment surrounding it. The binding energy increases when the neighbor atom has a high electronegativity that withdraws electron density away. This imbalanced charge distribution causes a chemical shift, rendering the atom harder to eject an electron. Binding energy also increases with formal charges, or oxidation state of the atom itself and the atoms surrounding it.

Compositions of the sample can be deduced from the weighed area ratio of peaks by the use of relative sensitivity factor (*RSF*), which represents how detectable the photoelectrons are. The total intensity, *I*, of a photoemission can be expressed as,

$$\frac{n_A}{n_B} = \frac{RSF_B \cdot I_A}{RSF_A \cdot I_B} \tag{2.7}$$

where n is the concentration of element i; the subscripts A and B represents two different elements.

Splitting of peaks is observed based on the electronic states of the electron. Non-zero angular momentum such as *p*, *d* and *f* orbitals causes orbital splitting known as Jahn-Teller effect. Doublets are seen due to the random excitation of spin-up and spin-down electrons in the same energy level. The intensity ratio of the two peaks depends on the degeneracy of the energy level, $(2j_- + 1) / (2j_+ + 1)$, where $j_- = \mathrm{L} - \mathrm{S}$ and $j_+ = \mathrm{L} + \mathrm{S}$. The intensity ratio is 1:2 for $p_{1/2}$ to $p_{3/2}$, 2:3 for $d_{3/2}$ to $d_{5/2}$, and 3:4 for $f_{5/2}$ to $f_{7/2}$ because of the electron population ratio.

The system used in this work is Kratos Analytical Axis Ultra DLD X-ray Photoelectron Spectrometer with a hemispherical analyzer. The data was collected using Aluminum anode was equipped and biased at 15 kV to generate monochromated Al K_α at a photon energy of 1486.6 eV. ALD CFO with major peaks are highlighted in Figure 2.16(a) from kinetic energy of 286.69 eV to 1491.69 eV (Binding energy of 1199.91 eV to -5.09 eV). The purpose of a full scan is to identify the existence of elemental peaks of interest, in this case, cobalt, iron and oxygen. The pass energy was 160 eV. The step size was 1 eV with a dwell time of 100 ms. The collected scan was first calibrated by using the adventitious C 1*s* peak to 284.6 eV. From Figure 2.16, the 2*s* and 2*p* peaks of Co and Fe were found between 950 and 700 eV. Higher energy levels such as Co 3*s* and Fe 3*s* (not labeled) were found at lower binding energies around 95 eV, which overlapped with Si 2*p* peaks. Auger peaks of O KLL, Fe LMM and Co LMM peaks were seen at 971, 891, and 713 eV respectively. Due to undesired overlapping of Auger peaks and insufficient signal-to-noise ratios, Co 2*s* and Fe 2*s* peaks were avoided.

For composition analysis, Co 2*p*, Fe 2*p*, and O 1*s* peaks were quantified. A detail measurement was performed for each elemental peak with a 0.1 eV step size and 300 ms dwell time. The pass energy was narrowed from 160 eV to 20 eV. Average of 5 scans was conducted to increase signal-to-noise ratio. Figure 2.16 (b) – (d) shows the detail measurement and sample fitting of the Co 2*p* peak. CasaXPS was the software used for data analysis. The scan was calibrated with C 1*s* peak as mentioned. A Shirley-type background fitting was implemented. Regarding the peak fitting parameters, the separation between $2p_{3/2}$ and $2p_{1/2}$ was forced to be the same as that between the corresponding satellite peaks. The area ratio of $2p_{3/2}$ to $2p_{1/2}$ was set to 2 from spin-orbital splitting. The full-width-half-maximum (FWHM) was set to equal. Same conditions were applied to the corresponding satellite peaks. Similar fitting procedures can be found in literature (Biesinger 2011).

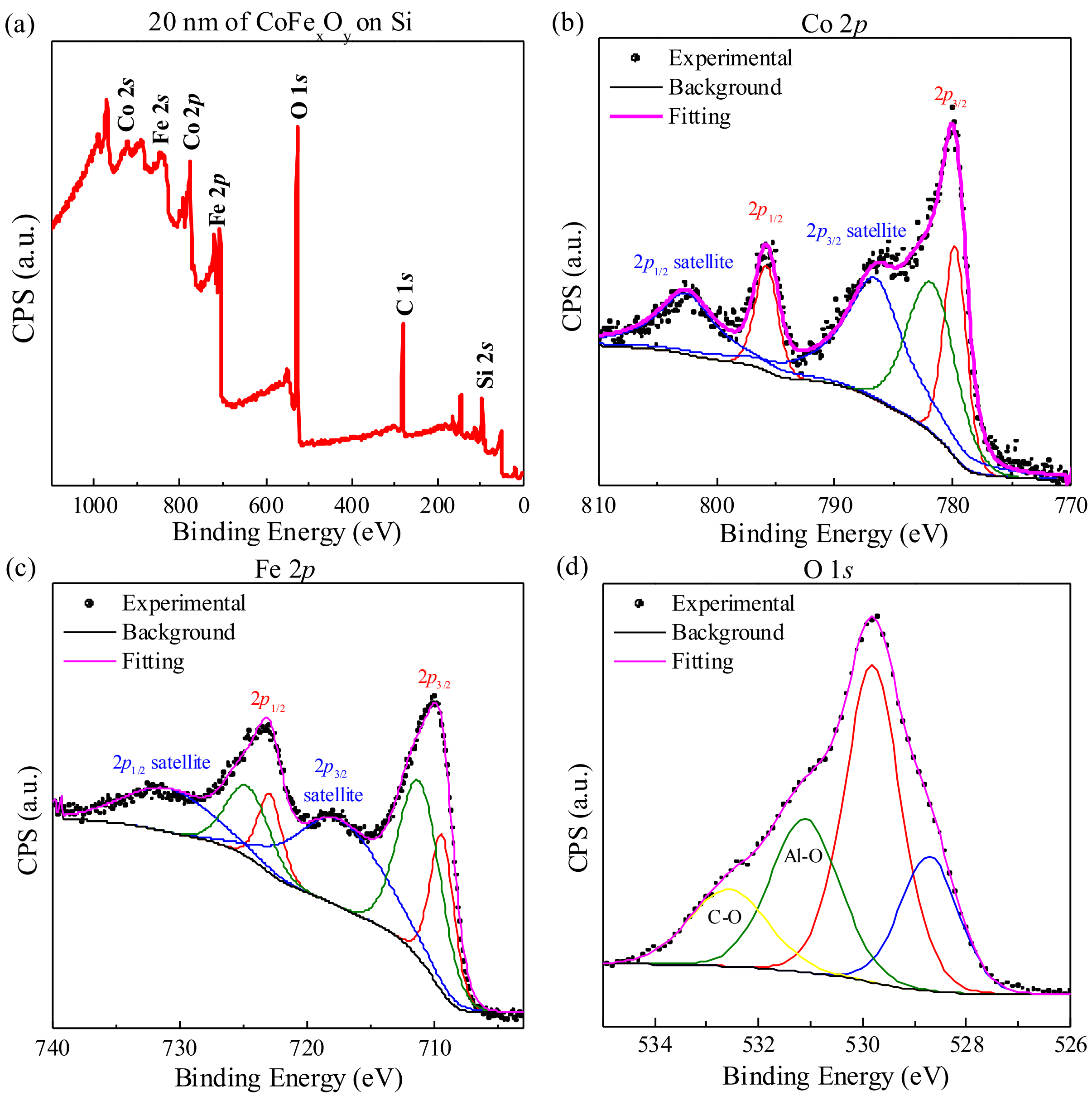

Figure 2.16 XPS spectra and fitting of (a) survey scan and detail scans of (b) Co 2*p*, (c) Fe 2*p*, and (d) O 1*s* peaks from 20 nm ALD CFO on Si. All spectra were calibrated with adventitious C 1*s* peak at 284.6eV. The calculated composition ratio of Co:Fe:O was 1:1.94:3.78.

An additional peak at 781.8 eV was added due to the asymmetric Co 2$p_{3/2}$ peak from mixed oxidation state of Co (II) and Co (III). The Co 2$p_{3/2}$ and 2$p_{1/2}$ were located at 779.8 and 795.8 eV respectively. The 2$p_{3/2}$ binding energy matches very well with the literature values of CFO at 779.7 eV. The peak splitting of 16.0 eV also matches the data retrieved from NIST database. Similarly, the Fe 2*p* peak was fitted with the same conditions with peak locations at 710.1 and 723.5 eV for $2p_{3/2}$ and $2p_{1/2}$ respectively with a separation of 13.4 eV. By using the RSF values of Co and Fe provided by the manufacturer and the area under curve, the composition ratio of Co to Fe was calculated to be 1:1.94, which is very close to the ideal 1:2 ratio in CFO.

The peak fitting of O 1*s* was different from Co and Fe due to various bonding states of oxygen and chemical shifts. As mentioned before, the binding energy increases when the bonded atom has a high electronegativity that withdraws electron density away. As a result, C-O peak was found at 532.6 eV. The peak at 531.1 eV was attributed to Al-O from the aluminum oxide substrate, which matches to the literature value (Wagner 1982). The remaining two peaks at 529.8 and 528.9 eV were originated from different oxidation states of Co and Fe or possibly hydroxyl-terminated surface. The areas of the two peaks were compared against that of Co. The ratio of Co to O was determined to be 1:3.78, which is slightly lower than the theoretical value of four.

2.5.2 X-ray Diffraction (XRD)

X-ray diffraction (XRD) is a widely used surface characterization method to investigate the crystalline structure, lattice spacing, crystallinity and crystal grain size of sample-under-test based on the interference of two reflected x-ray beams (Alford 2007).

Under illumination of X-ray, electron clouds around an atom resonate by the incident electromagnetic wave. The movement of the charges induces a coherent electromagnetic wave with the same frequency as the incident wave, and re-emitting to space. When the wave is scattered by an array of atoms in a unit cell of the crystalline structure, the intensity of the reflected light is derived based on the wavelength of the light, interatomic spacing, and the relative angle of the incident beam to the orientation of the crystal. Peaks are detected if constructive interference occurs between scattered light beams towards the detector.

Mathematically, the diffraction condition can be represented by the construction interference, occurs if the path difference (*Δa*) of the two beams is an integer multiples (*n*) of the incident wavelength, namely, Bragg's Law,

$$n\lambda = 2\Delta P = 2d_{hkl}\sin\theta \tag{2.8}$$

Measurements are taken by a diffractometer, consists of monochromatic radiation source, slit, sample stage and a detector. A typical system uses a theta-theta configuration and equip with Cu-K_α source, producing X-ray with wavelength of 1.54 Å. Both the X-ray source and the detector move with the same degree, θ, relative to the sample plane and along the circumference with the powder sample as the origin. The collected intensity is directly proportional to the intensity of the X-ray entering the detector.

From first principles, Bragg's Law can be rewritten as the following by representing the lattice constant, d_{hkl}, by Miller indices, (*h k l*), and the lattice constant, a_o, such that,

$$\sqrt{h^2+k^2+l^2} = \frac{2a_0\sin\theta}{n\lambda} \tag{2.9}$$

where the lattice constant can be calculated given that Miller indices are known from the diffractogram. However, assigning peaks with the correct indices is a challenging task due to overlapping of similar crystal structures and interference between grains.

In an atomic analysis, the optical path difference in reaching electrons within an atom is negligible. However, the wavelength used in X-ray analysis is chosen to be comparable to atomic spacing, such that the path difference in reaching neighboring atoms would affect the phase difference between scattered waves, resulting in interference. The scattered amplitude from a unit cell can be described as,

$$F_{hkl} = \sum_{n} f_n e^{i\varphi} = \sum_{n} f_n e^{i2\pi(hu_n + kv_n + lw_n)} \tag{2.10}$$

where φ accounts for the phase difference of the wave scattered by an atom relative to origin of the unit cell. The change in phase can be further manipulated and represented by the Miller indices (*hkl*), and the position vector (*uvw*). The above equation is the sum over all atom scattering within the unit cell. The allowed reflection is resulted from a non-zero intensity $I_{hkl} = F_{hkl}^2$. Note that the exponent of odd multiples of $n\pi i$ equals to -1, while that with even multiples equals to 1. Therefore, the odd or even nature of the sum of the Miller indices (*hkl*) dictates which crystal plane would lead to constructive interference and allows diffraction to be detected.

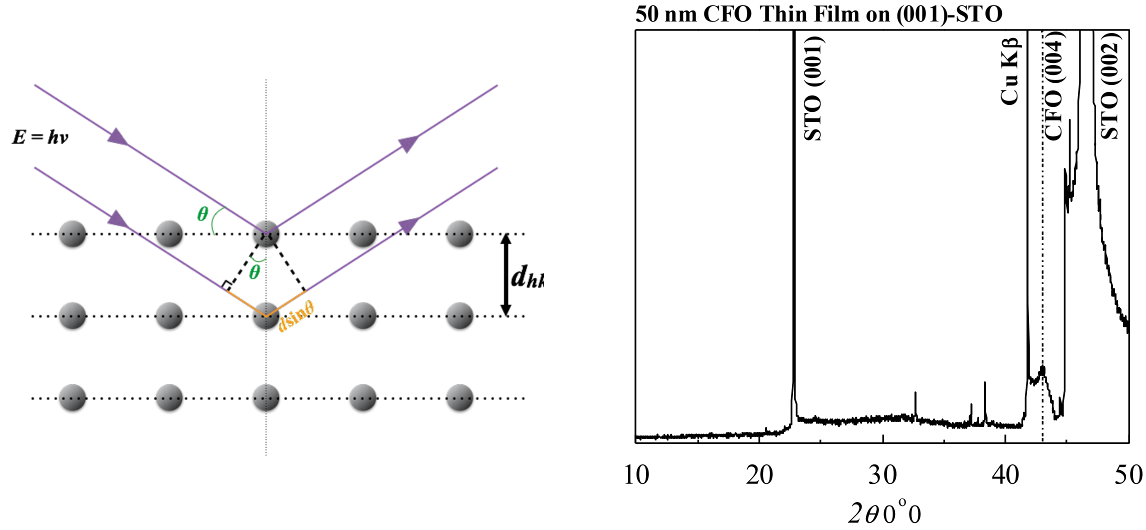

Figure 2.17 (left) Schematic of X-ray diffraction in crystal lattice; (right) diffractogram of 50 nm of ALD CFO on (001)-$SrTiO_3$ after annealing at 550°C. (Pham 2015).

The systems used in this work are X'pert Pro PANalytical Powder X-ray Diffractometer and SSRL Beamline 7-2. For X'pert Pro diffractometer, copper anode was used to generate K_α radiations (1.54 Å). A 1/2° divergence slit was used and an automatic slit control was implemented to keep the irradiated length to be 5 mm as 2θ increases. The receiving slit size was 0.1 mm. A sample scan of 50 nm of CFO on (001)-$SrTiO_3$ deposited by ALD was shown in

Figure 2.17, measured after the samples were annealed from 450°C to 750°C. The measurement was scanned at ambient conditions from 10° to 50° with a step size of 0.05° and a dwell time of 40 ms. Based on tabulated tables and known crystal structures, Highscore X'Pert Plus software was used for data analysis. Peak location, area and intensity determination were used to identify the crystalline structure and phase of the material of interest. For SSRL Beamline 7-2, synchrotron was used to generate X-ray at 1.5418 Å with an energy resolution of 0.03% error. The experimental station is equipped with a customized Huber type 5021 6+2 axis and uses Pilatus 100K and 300K area detectors, a Si crystal-analyzer with point detector for higher resolution studies. The angle resolution is kept within 0.03 degrees.

The diffraction pattern was indexed by referencing to tables of data such as Joint Committee on Powder Diffraction Standards (JCPDS), a database of powder diffraction patterns organized by the International Center for Diffraction Data (ICDD). Powder samples are regarded as polycrystalline. Table 2.5 shows a list of compounds with corresponding JCPDS used in this study.

Table 2.5 XRD JCPDS for selected chemicals studied in this work

Compound	JCPDS	Crystal Structure	Space Group
Si	00-027-1402	Cubic	Fd-3m
SiO_2	00-005-0490	Hexagonal	P3121
Pt	00-004-0802	Cubic	Fm-3m
$SrTiO_3$	00-074-1296	Cubic	
$Pb(Zr_{0.52},Ti_{0.48})O_3$	00-033-0784	Tetragonal	P4mm
$PbZrO_3$	00-035-0739	Orthorhombic	P2cb
$PbTiO_3$	01-070-0746	Tetragonal	P4mm
$CoFe_2O_4$	00-022-1086	Cubic	Fd3m
Al_2O_3	00-001-1243	Rhombohedral	R-3c

Crystallinity, grain size and strain can be calculated from XRD spectra. The relative intensity, presence and absence of peaks comparing with JCPDS can be used to identify the crystalline phase of the material, and deduce if the crystal structures are preferentially oriented in a specific direction. From the JCPDS of STO, the strongest diffraction peak was (110) at 32.4° while the second strongest peak (200) has half the intensity. From Figure 2.17, the strongest peak was found at 22.775°, which correspond to STO (100) peak at 22.783° from JCPDS. It indicated the substrate was strongly (100) oriented. Similarly, the only apparent CFO peak was found at 43.25°, which corresponds to CFO (400) peak at 43.06°. Since the strongest diffraction of powder CFO was (311), the XRD of the sample indicated the CFO was preferentially grown and crystalized in (400) orientation. The shift of the peak location was not attributed to the fact that the samples were not perfectly aligned in the z-axis. A smaller shift was seen in a higher 2θ value from (002) STO at 46.505° compare with the JCPDS value of 46.485°. However, the shift in the CFO peak was 0.19°. The increased 2θ value translates into a decreased *d*-spacing according to Bragg's Law. The CFO lattice was compressed due toe the lattice mismatch between STO (3.905 Å) and CFO (8.39 Å). By increasing the annealing temperature from 550°C to 750°C, the CFO (004) peak sharpens as an indication of grain growth. According to the Scherrer equation, the grain size could be approximated using the full-width half maximum (FWHM) of the peak.

$$\tau_{grain} = \frac{0.9\lambda}{FWHM \cdot \cos\theta} \tag{2.11}$$

where τ_{grain} is the grain size; λ is the wavelength of the x-ray (1.5418 Å); and θ is the Braggs angle. The FWHM (in radians) of the CFO peak was determined to be 0.006 rad from the plot. The grain size was calculated to be 24.8 nm after annealing at 750°C.

2.5.3 Scanning Electron Microscopy (SEM)

Scanning electron microscopy (SEM) collects the emitted secondary electrons from the specimen to create an image. The electron beam is sharply focused onto a point of the sample by the deflection coil. The sample is scanned in a raster fashion until the entire image is obtained, as shown in Figure 2.18. The electron bombardment on the sample generates secondary electrons and back-scattered electrons. The amount of emitted electrons being collected equals signal intensity. In principle, the magnification in SEM systems does not depend on the power of objective lens, which is the case in optical systems and TEM. In extreme case, SEM would operate without focusing. How sharp the beam is focused onto sample determines the magnification of the setup.

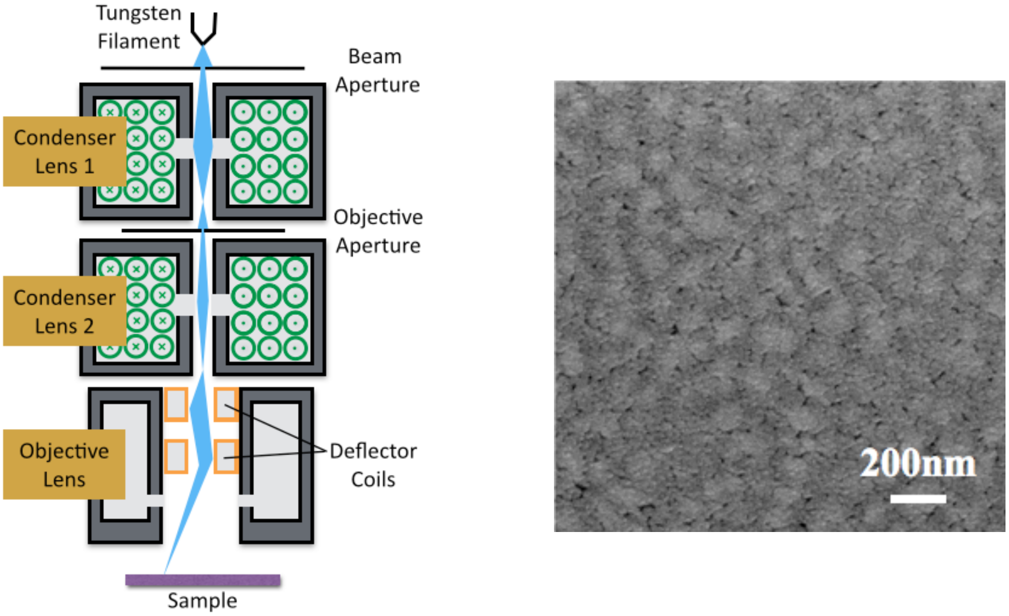

Figure 2.18 (Left) Schematic of scanning electron microscopy. (Right) Top-down SEM image of mesoporous PZT with pore neck radius of 10 nm, coated with 3 nm of ALD CFO (33% filled) was taken using Hitachi S4700 SEM.

By definition, secondary electrons are electrons emitted from the outermost shells of an atom. They can be emitted with relatively low energy as they are loosely bounded. Electron bombardment causes cascade damages into the film similar to ion implantation. The affected area has a shape of raindrop along the axis of bombardment direction. Therefore, flat surfaces have less secondary electron emission due to large escape length required, resulting in darker features. Curves and edges, however, allow secondary electron to escape from the surface easily, resulting in brighter features. The intrinsic difference in signal intensities gives the three-dimensional effect on the image without further image processing.

Back-scattered electron is a different mode of operation in SEM systems. It collects the electron reflected backwards to the incident direction by diffused reflection. Elements with higher atomic number have higher efficiency in reflecting electrons. Based on the signal intensity distribution, an elemental plot can be obtained for composition analysis. However, it is difficult to determine specific elements.

Although the resolution of SEM is in the order of micron, it allows simpler sample preparation for quick measurements than TEM. Material charging, due to the emission of electrons under excitation, poses a disadvantage on insulating materials. Gold sputtering is usually recommended.

The system used in this work was 15kV Hitachi S-4700 electron microscope with a resolution of 1.5 nm. It is a field emission SEM with attached energy dispersive x-ray spectrographic detector and backscatter electron detector. The working distance used in this work was fixed at 12 mm with a resolution of 20 nm. The accelerating voltage was fixed at 10kV while the current was adjusted between 5 and 10 mA depending on whether the sample is charging. Specimen tilt at maximum 45 degrees was used for tilted-view imaging. Samples with size of 5 mm x 5 mm were adhered onto the aluminum sample stage by copper adhesive. An image of mesoporous PZT with neck diameter of 20 nm coated with 3 nm of CFO is shown in Figure 2.18.

2.5.4 Superconducting Quantum Interference Device (SQUID)

Superconducting quantum interference device (SQUID) is used to measure magnetic properties of materials of interest. It utilizes inductive detection of magnetic moment with a sensitivity up to 10^{-11} J/T.. The high sensitivity is originated from Josephson effect of superconductors. In a SQUID magnetometer, two superconductors are separated by a thin insulator, creating two Josephson junctions as shown in Figure 2.19

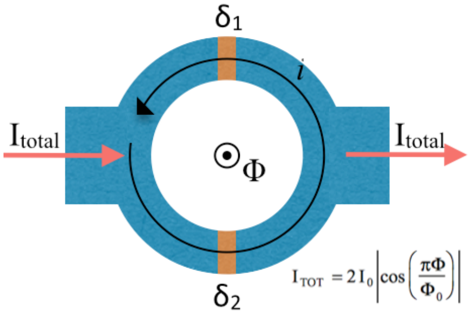

Figure 2.19 Schematic of Josephson junctions in SQUID

If the insulating layer is thin enough (~10 nm), electron pairs can tunnel through the barrier without potential difference, and thus no energy loss. Such electron pairs are known as Cooper pairs, which only exist in superconducting states. Electrons in general do not couple with each other due to high electrostatic repulsion. At extremely low temperature, however, electrons are coupled with the help of metal cation lattice as a result of electron-phonon coupling. It can be viewed as the distortion of cation lattice caused by a single electron that attracts another electron at a certain separation (~100nm) due to the local positive charge density. Mathematically, a Cooper pair can be represented by a single wavefunction. During the tunneling effect, the wavefunction decays exponentially similar to free particle within potential wall. Since Cooper pairs can tunnel from either side of the Josephson junction, the net difference of the phase in the wavefunction determines the tunneling current, with the absence of potential difference.

From the quantum analysis, the Josephson current oscillates as a function of applied magnetic field. In SQUID magnetometer, a separate input coil generated magnetic flux into the primary coil, which consists of two Josephson junctions in parallel (Lueken 2012). The total current becomes the difference of the tunneling currents in both paths and can be represented as,

$$I_{tot}(\Phi) = 2I_0 \left| \cos\left(\frac{\pi\Phi}{\Phi_0} \right) \right| \tag{2.12}$$

When applied magnetic field increases, the total current oscillates with a period of Φ_0 with a slower modulation envelope created by individual Josephson junction. If the total current is set to constant larger than $2I_0$, the modulation of both junctions can be seen. As a result, the output voltage across the two ends oscillates with a period of Φ_0 as a function of applied magnetic field, allowing the measurement on magnetic flux change with the use of shunt resistors. The mechanism of SQUID is often described to be quantum interference as the modulation of signals resembles optical interference in Young's double slit experiments. Depending on the magnetization response of the sample under external field, the amplitude of the output voltage changes. The output voltage is then plotted as a function of magnetic signal input from the pickup coil.

Valuable information such as saturation magnetization and coercive field can be obtained. Due to the sample mount in SQUID magnetometer, diamagnetic and paramagnetic signals are unavoidable in measurements. Since the ferromagnetic signals can be saturated at high enough field, a magnetic field greater than 5 times of the coercivity is normally used. The diamagnetic and paramagnetic signals are subtracted though linear regression of the both tails of the signal. It is then normalized by the magnetic volume of the samples.

In this work, Quantum Design MPMS SQUID magnetometer was used with a sensitivity down to 10^{-7} emu. Figure 2.20 shows SQUID plot of 7 nm of CFO sample on $SrTiO_3$ deposited by ALD. The magnetic moment was measured with an applied magnetic field from 20 to -20 kOe and back to 20 kOe. The step size changes from 5 kOe increments at fields higher than 2 kOe to 100 Oe increments at low field for better accuracy near the coercivity. The measurements were averaged over 3 scans. The details of each step can be found in Appendix B. FM hysteresis loop was observed at room temperature of CFO grown on STO with a saturation magnetization value (M_r) of 550 emu/cm^3 and a coercive field value (H_c) of about 1300 Oe when the applied field is in plane with the substrate. The out-of-plane measurements have a lower saturation magnetization value of 400 emu/cm^3 and a lower coercivity of about 400 Oe.

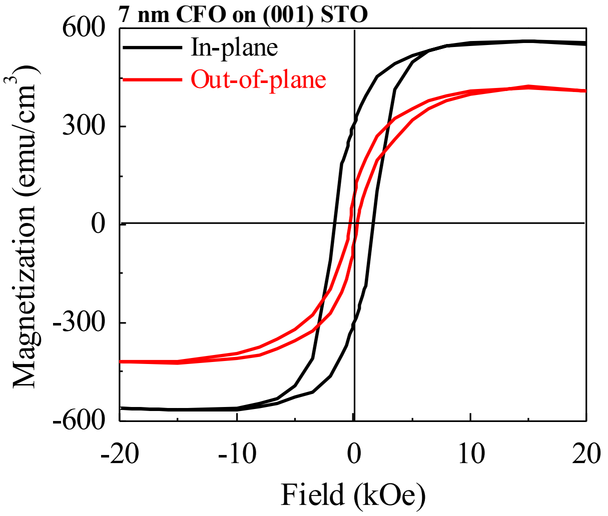

Figure 2.20 In-plane (black) and out-of-plane (red) SQUID measurements of 7 nm of ALD CFO grown on SrTiO$_3$ planar substrate. The coercive field and saturation magnetization were 1300 Oe and 550 emu/cm^3 respectively (Pham 2017).

2.5.5 Force Microscopy (AFM, PFM, MFM)

Atomic force microscopy (AFM) is used to characterize surface roughness and morphologies of relatively large area (5 µm x 5 µm). In a typical AFM setup, a cantilever with a sharp tip is brought into contact with the device under test. The forces between the tip and the sample such as van der Waals forces, electrostatic and dangling chemical bonds cause a deflection of the cantilever. The small deflection is measured by a laser reflecting off the cantilever surface and captured by a photodiode. Based on which photodiode is activated by the reflected light, the trajectory of the reflected beam is translated into the vertical motion of the cantilever tip. Different modes of data collection such as actual trajectory of laser beam and phase change of light can determine the surface roughness of the sample. The tip is then moved as raster scan to obtain data for the selected area. A root-mean-square value of surface roughness is calculated by averaging the sum of height differences between individual data point with its mean value, namely,

$$t_{rms} = \sqrt{\frac{1}{n}\sum\left(t_i^2\right)} \tag{2.13}$$

where t correspond to the height of the tip. Piezo-response force microscopy (PFM) and magnetic force microscopy (MFM) are modifications of AFM setups using different contact tips. In PFM, as the tip is brought upon contact, a small sensing current with a fixed bias is applied through the tip. When the material is piezoelectric, the local area that experience the electric field would expand or contract, resulting in deflection of the tip as a function of electric field. MFM, on the other hand, uses permanent magnetic coatings on the tip such that local area on the sample would experience an external magnetic field, while magnetic forces acting on the tip would cause deflection when the material is magnetized. Therefore, magnetostrictive changes in surface morphology could be detected. In MFM measurements, a morphology scan is first performed with contact mode. The tip is then lifted up by a user-defined height and retraces the morphology. The measure deviation from the morphology is treated as the magnetic response from the sample.

The combination of AFM, PFM and MFM could be used as a qualitative demonstration of ME coupling. Changes in magnetic domains orientation as a function of poling voltage can be qualitatively observed. Mesoporous PZT fully filled with CFO by ALD was measured under PFM and MFM using Bruker Dimension Icon Scanning Probe Microscope as shown in Figure

2.21. The PZT thickness was 100 nm with pore size of 20 nm. The same area of 5 x 5 μm^2 was measured with 256 raster lines and a scan rate of 1.00 Hz. The drive amplitude of the tip was 717.16 mV at amplitude setpoint of 289.45 mV. Bruker AFM MESP tip was used for the measurement. The rectangular Sb-doped Si cantilever was coated with magnetic CoCr. The tip height and radius were 10 µm and 35 nm respectively.

The morphology, piezoresponse and magnetic response of the sample were first measured by SPM before poling as a reference, as shown in Figure 2.21 (a)-(c). The surface roughness was measured to be 2.59 nm. There was no apparent piezoresponse or preferred magnetic orientations. The center 1 x 1 μm^2 was then biased at -10 V using the probe in three consecutive scans with contact mode. The same measurements were performed after the sample was poled. The central area has an increase of 5-7 nm in morphology. More importantly, the darker color in the MFM image indicates the magnetic domains were oriented out-of-plane by the applied voltage, while the surrounding was lighter in color indicating the domains were oriented out-of-plane and antiparallel. The use of both PFM and MFM illustrated the sample demonstrated magnetoelectric couplings.

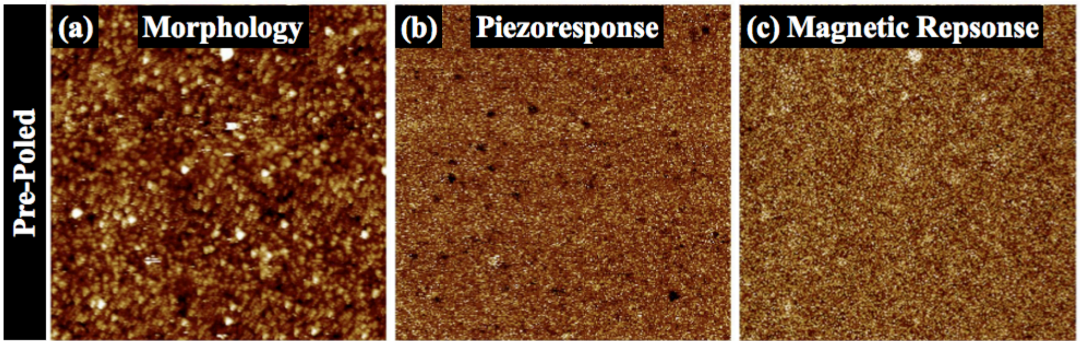

Figure 2.21 (a) AFM, (b) PFM, and (c) MFM measurements of 100 nm thick mesoporous PZT template with 3 nm of ALD CFO coating (33% pore neck filling). The scanned area has dimensions of 5 µm x 5 µm.

2.5.6 Converse Magnetoelectric Coupling Measurement

Magnetoelectric coupling is the primary figure of merit in this work. It describes the material ability in controlling magnetic field by manipulation of electric field. As a quantitative measurement of ME coefficient, it can be realized by measuring the induced electric field under an applied AC magnetic field using a FE tester and SQUID magnetometer. Instead of using SQUID to measure magnetizations of the sample, ac magnetic field is modulated through the sample. The frequency of the magnetic field is fed back to the FE tester through a lock-in amplifier as the reference phase. With set values of frequency and amplitude of ac magnetic field at constant dc magnetic field, the FE response is collected to compute magnetoelectric coupling by comparing polarization changes at given increment of ac magnetic field at constant dc magnetic field. Wan et al measured ME coupling in similar fashion for CFO-PZT nanocomposites (Wan 2007).

Similar quantification of magnetoelectric coupling can be obtained. When a composite sample is poled to a remnant state prior to SQUID measurement. By definition, the magnetoelectric coupling at a given magnetic field is the change in magnetization at two different poling electric fields, given that the change in electric field is small.

In order to quantify the magnetoelectric coupling in multiferroic composites, the magnetic responses of a 100 nm mesoporous CFO coated with ALD PZT was measured at different electrical poling. The backside of the substrate was coated with 300 nm of Ti as a back electrode by e-beam evaporation. The silicon substrate was heavily doped to be conductive. The sample was *ex-situ* poled between two aluminum electrodes (1.28 cm in diameter) and a 12 µm thick polyvinylidene chloride (PVDC) layer was added on top of the sample to prevent electrical breakdown. The aluminum electrodes were electrically connected to a Stanford Research System PS350 DC power supply. The electrical poling setup is shown in Figure 2.22.

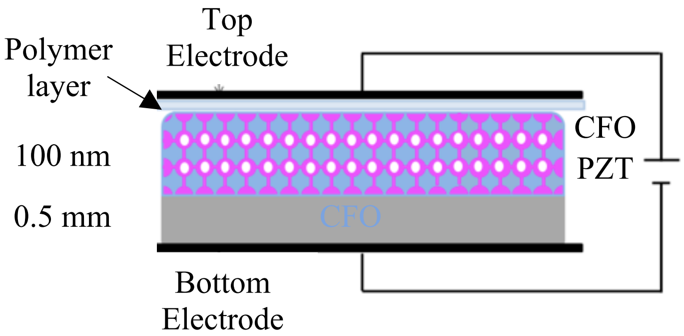

Figure 2.22 Schematic of the *ex-situ* electrical poling setup of the mesoporous CFO coated with ALD PZT.

The composite was poled for 10 minutes ranging from 0 to 200 V. The voltage was converted into c field by the following equations.

$$
\begin{aligned}
E_{composite} &= \frac{V_T}{d_{composite}} = \frac{Q_T}{C_{composite} d_{composite}} \\
Q_T &= C_T V_T = \left(\frac{1}{C_{PVDC}} + \frac{1}{C_{composite}} \right)^{-1} V_T \qquad (2.14) \\
C_{composite} &= \frac{\varepsilon_0 \varepsilon_r A}{d_{composite}}
\end{aligned}
$$

where the subscripts T represent the total electric field (E_T), voltage (V_T), or charge (Q_T). The composite and the PVDC were treated as dielectrics in series that the charge accumulated at the interface was equal ($Q_T = Q_{PVDC} = Q_{composite}$). Individual capacitance can be calculated as parallel plate capacitors with a sample size of 5 x 5 mm^2. The dielectric constants of PVDC, PZT, and CFO were 6, 720, and 370 respectively (Udayakumar 1995), (Gul 2008). For the composite, the dielectric constant was approximated by the volume due to the complexity of the porous structure. The electric field across the composite and PVDC were calculated to be 0.18 and 16.67 MV/m at 200 V.

Figure 2.23 shows the out-of-plane SQUID spectra of 100 nm thick PZT coated mesoporous CFO after 10 V and 100 V after *ex-situ* out-of-plane poling. Based on the definition of magnetoelectric coupling, as a ratio of change in magnetization as a function of the change in electric field, the sample has a converse ME coupling factor of 1 × 10^{-5} Oe-cm/mV. The step-by-step calculation is shown. The value was one order of magnitude higher than that in the literature of PZT/CFO composite of 1.1 × 10^{-6} Oe-cm/mV (Peng 2015).

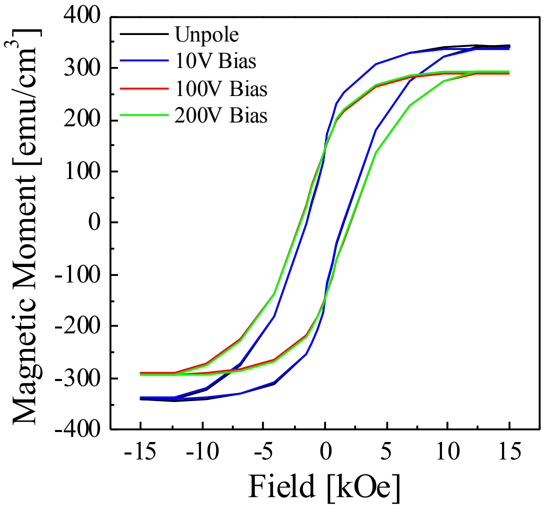

	Unpoled PZT	100V Poled PZT
Electric field	–	0.71 MV/m
Saturation Magnetization	337 emu/cm^3	286 emu/cm^3
Change in magnetization	ΔM = 51 emu/cm^3 = 640 Oe	
Converse ME coupling	ΔM/ΔE = 1 × 10^{-5} Oe-cm/mV	

Figure 2.23 Out-of-plane SQUID scans of ALD PZT of 3nm film on EISA mesoporous CFO with 15 nm pore size. PZT was poled out-of-plane from 10V to 200V (Chien 2016). The table on the right shows the sample calculation of the converse ME coupling of PZT coated mesoporous CFO after *ex-situ* poling at 10 V and 100 V.

In summary, CFO and PZT are introduced as the material of interest in investigating the strain-induced magnetic shape anisotropy and magnetoelectric coupling. The characterizations of single phase CFO and PZT were carried out using SEM, XPS, XRD and SQUID. With the use of atomic layer deposition, the magnetic properties of 1D CFO are discussed in Chapter 3. After fabricating 0D-3D and 1D-1D CFO/PZT nanocomposite in two different templates, the composite functionalities are discussed in Chapter 4 and 5 respectively.

CHAPTER 3 Magnetic Anisotropy of 1D $CoFe_2O_4$ Nanotubes

CFO nanotubes were grown in anodic aluminum oxide (AAO) membranes of pore sizes 80 nm, 35 nm, and 18 nm via radical-enhanced atomic layer deposition (RE-ALD) to study magnetic shape anisotropy of 1D magnetic structure. The deposition was achieved using TMHD precursors (TMHD = 2,2,6,6-tetramethyl-3,5-heptanedionate) and oxygen radicals at 200°C with a growth rate of 2.41 Å/cycle, as described in Chapter 2. Amorphous nanotube arrays were formed inside the cylindrical pores and crystallized at 550°C according to XRD. With a deposition depth of 1 micron verified by EDS studies, the aspect ratios of the nanotubes were 13 29, and 56. Compare with planar CFO thin films, the saturation magnetization was increased by a factor of 5 in nanotube structure. As the pores were progressively filled with RE-ALD, the magnetic easy axis was switched from perpendicular to parallel to the nanowires' axes. The out-of-plane anisotropy energy was observed to be 51% higher than that from in-plane axis, indicating the out-of-plane axis was magnetically more favorable. The magnetic anisotropy increases as the aspect ratio increased. It demonstrated by controlling the degree of filling and pore diameter of the nanostructures, it is possible to manipulate the magnetization based on shape anisotropy. By reducing the pore diameter of the membrane, the anisotropy in the out-of-plane orientation increases.

3.1 Growth and Characterizations of One-Dimensional CFO Nanostructures

Exploiting the conformal nature of atomic layer deposition, high aspect ratio (greater than 10) CFO nanotubes and nanopillars could be grown inside the pores. The magnetic shape anisotropy of the CFO nanostructures was then investigated as a function of pore diameters and the degree of which the pores were filled.

ALD of CFO was deposited inside AAO membranes and the surface morphology was studied. Same deposition and annealing conditions as described previously were carried out to fabricate CFO nanotubes in AAO membranes. Figure 3.1 (a)-(c) shows the top-down view of a blank AAO surface, AAO after the pores were half-filled and fully-filled respectively. The 80 nm diameter pore was narrowed and sealed as increasing amount of CFO was deposited. The surface morphology was preserved as the shape of the pore was observable after being fully filled due to the conformality of the ALD process. A thin film began to form on top of the membrane as observed in Figure 3.1(c) after the pores were fully filled. The schematic shows the formation of nanotubes inside the AAO structure. The bottom copper adhesive layer was used to prevent charging from SEM measurements.

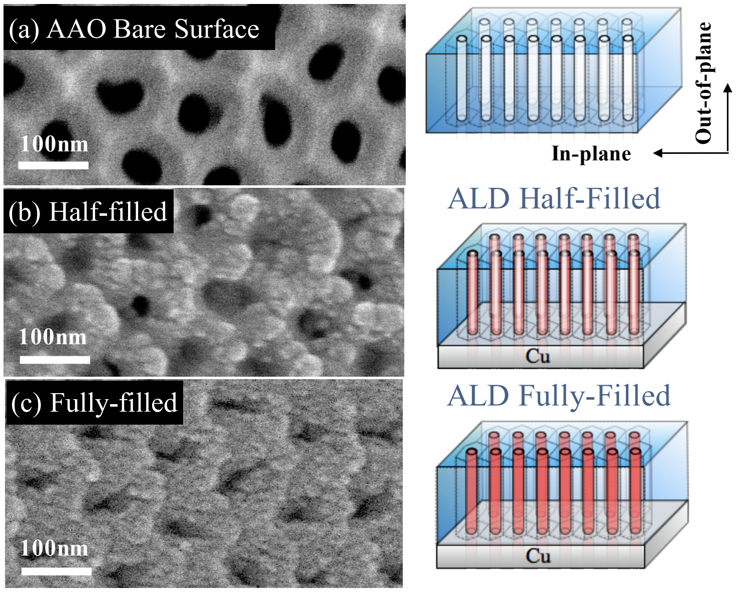

Figure 3.1 Surface morphology of (a) AAO bare surface with 80 nm diameter pores, (b) pore half-filled, and (c) pore fully-filled with ALD CFO. The schematic showed on the right illustrate the deposition process of ALD CFO inside the membranes to form nanotube and nanopillar array

The aspect ratio and morphology of the CFO nanotubes and nanopillars were investigated. In order to observe the nanotubes inside the AAO structures, the membranes were dissolved in

1M NaOH after 30 minutes at room temperature. Due to the high aspect ratio of the nanotubes and lack of structural support, the assembly collapsed and agglomerated after the removal of the template. Figure 3.2 (a)-(b) showed the top-down micrographs of both nanotube and nanopillar structures. A wall thickness of 22 nm with a length up to 1 micron was observed from the half-filled sample.

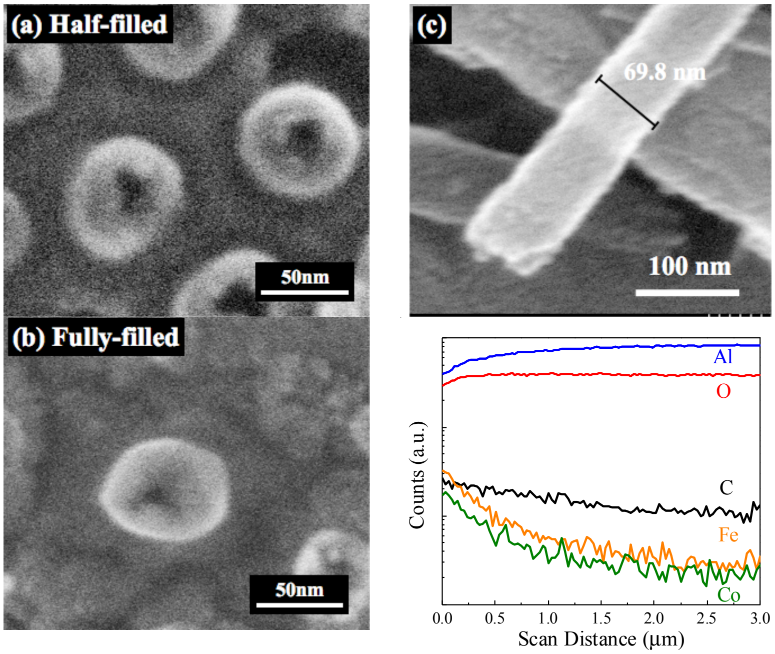

Figure 3.2 SEM images of AAO (diameter = 80 nm) with (a) half-filled, and (b) fully-filled with ALD CFO to form nanotube array. (c) A single nanotube were imaged after dissolution of AAO membrane in 1M NaOH for 30 minutes. (d) Cross-sectional EDS spectrum of the half-filled membrane.

A single nanotube with diameter of 69.5 nm was imaged and shown in Figure 3.2 (c). The reduced diameter was attributed to the slight narrowing of the original pore and slow dissolution rate of CFO in NaOH. The penetration depth of the deposition process was investigated by cross-sectional energy-dispersive X-ray spectroscopy. The compositions were measured along the thickness of the membrane before dissolution. Characteristic X-rays emitted from Co and Fe electron transitions were detected down to 1 micron from the membrane surface, which agrees with the SEM results. The partial penetration of the RE-ALD process could be explained by the nature of oxygen radicals recombination in high aspect ratio channels.

3.2 Manipulating Magnetic Easy Axis of One-Dimensional CFO Nanostructures through Shape Anisotropy

The geometric effect on magnetic responses of CFO thin film and pillar structure were compared. In Figure 3.3, 15 nm of CFO thin film was deposited on planar $SrTiO_3$ to compare with 15 nm of CFO in AAO. The in-plane is defined to be along the membrane surface, while out-of-plane is defined as along the thickness and along the long axis of the nanotubes. In-plane magnetic easy axis was observed with a higher remnant magnetization, coercivity, and saturation magnetization. The in-plane direction was expected to inherit strain from substrate surface and clamped. In contrast, a dominating out-of-plane easy axis was measured from the array of 1D CFO nanotubes, attributing to the enhanced perpendicular magnetic shape anisotropy in 1D structure. The out-of-plane saturation magnetization was an order of magnitude higher than that from in-plane. It should be noted that both magnetic responses were not normalized.

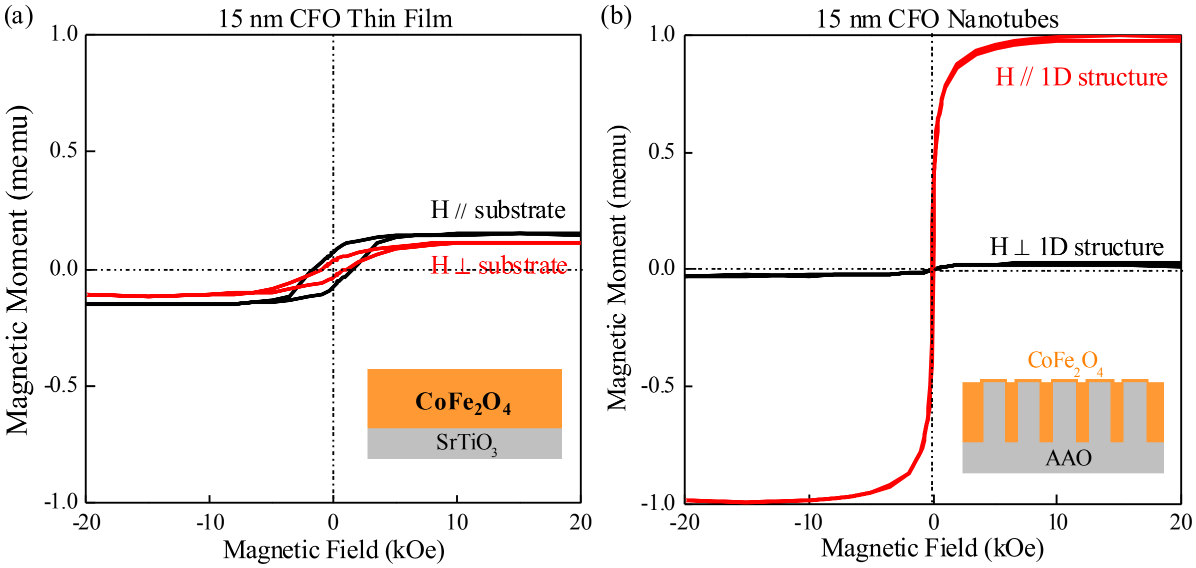

Figure 3.3 Magnetic responses of (a) 15 nm of planar ALD CFO deposited on planar SrTiO$_3$ and (b) 1D CFO nanostructure inside AAO membrane with 18 nm pore diameter, measured by SQUID at magnetic field along both in-plane and perpendicular directions at room temperature.

The effect of AAO pore diameter and filling degree on magnetic shape anisotropy were also investigated. When the membrane with 35nm pore diameter was 33% filled and 67% filled, the magnetic response resided in-plane. Upon complete filling of the pores, the magnetic easy axis was switched to out-of-plane due to the formation of nanopillars. Similar responses were observed in the pore diameters studied (18, 35, and 80 nm). As more CFO was deposited after completely filling, the magnetic easy axis was switched back to in-plane due to the formation of magnetic thin film on top of the membrane, as shown in Figure 3.4.

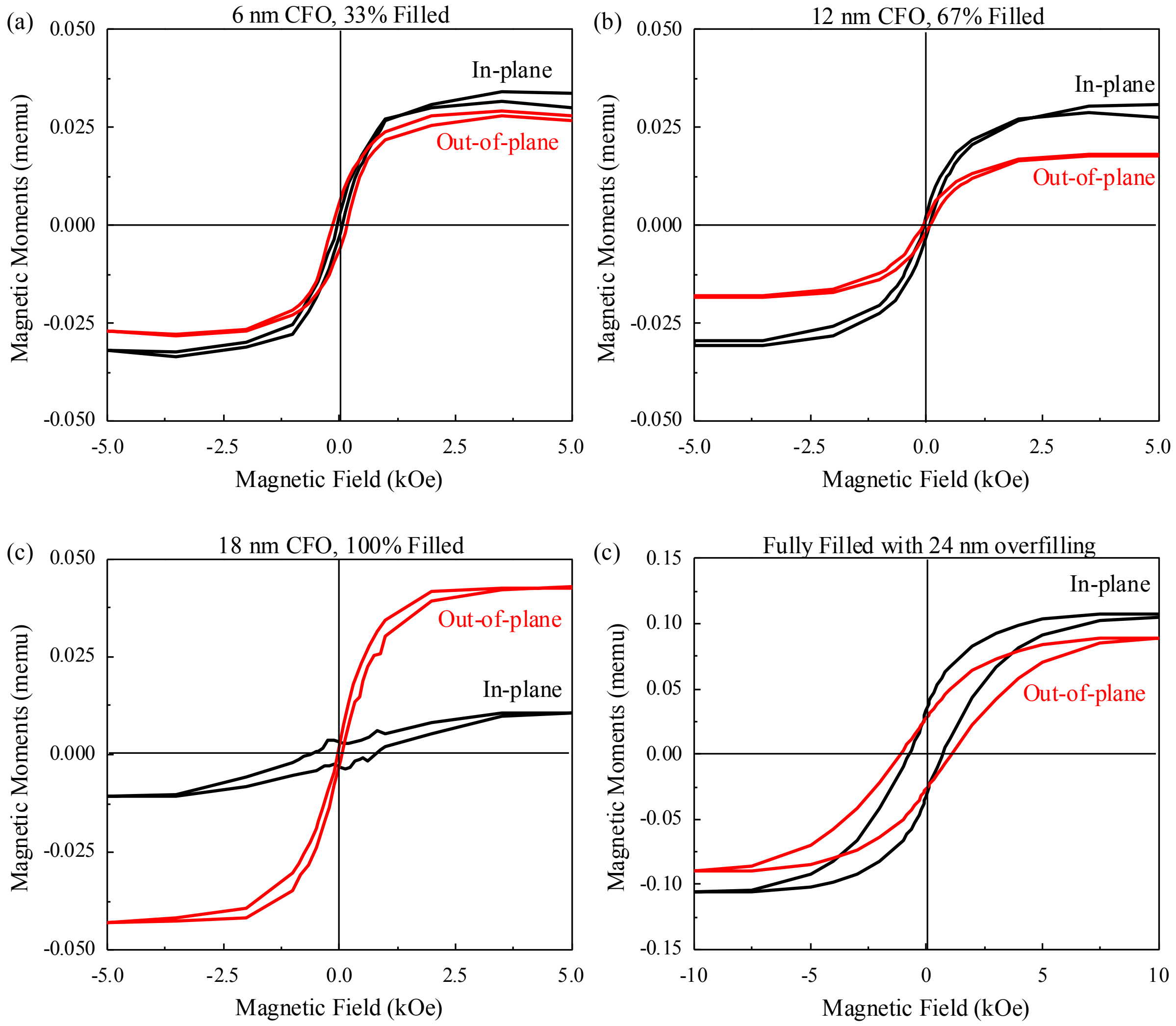

Figure 3.4 Magnetic responses of 1D CFO nanostructure deposited in AAO with 35 nm pore diameter with (a) 6 nm (33%), (b) 12 nm (67%), (c) 18 nm (100%) CFO deposition (% filling), and (d) 100% filled with additional 24 nm thin film.

Nanopillars with different diameter were fabricated to compare the effect of shape anisotropy. In Figure 3.5, the difference between in-plane and out-of-plane responses was the greatest at 18nm pore diameter. The distinction of the out-of-plane easy axis decreases as the pore diameter increases from 18 nm to 80 nm. The aspect ratio of the nanopillars decreases as the diameter increases, which led to a reduced shape anisotropy.

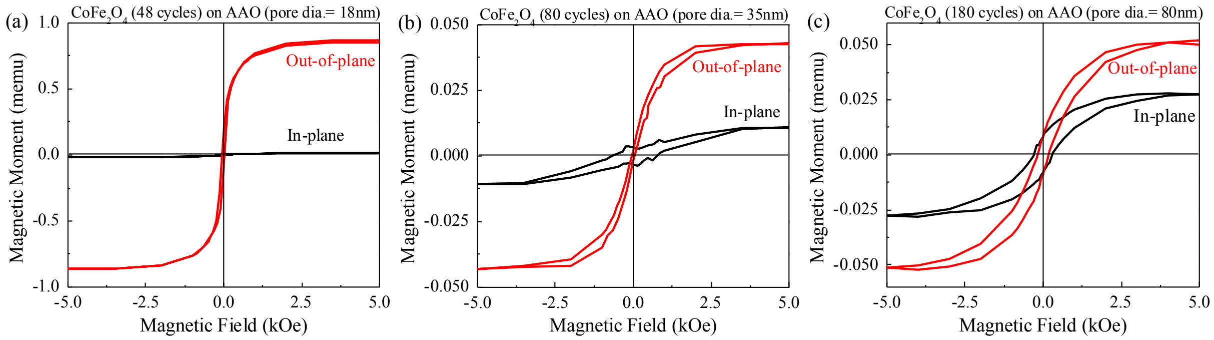

Figure 3.5 Magnetic responses of 100% filled 1D CFO nanopillars deposited in AAO with (a) 18 nm, (b) 35 nm, and (c) 80 nm pore diameter through ALD. The out-of-plane easy axis was less prominent at higher pore diameters as a result of increasing shape anisotropy.

The anisotropy energy at different degree of filling in the 35 nm pore diameter was calculated by integrating the hysteresis curve. The initial magnetization curve of each hysteresis was estimated by fitting the loop in the first quadrant. The curve was integrated against the magnetization value (y-axis) in order to obtain the anisotropy energy. The energies for both in-plane and out-of-plane hysteresis were calculated. As the %-filling of the pore increases, the in-plane anisotropy energy decreases linearly from 0.48 to 0.15 erg/cm^3. Similarly, the out-of-plane anisotropy energy decreases from 0.48 erg/cm^3 at 33% filled to 0.28 erg/cm^3 at 67% filled. At completely filling, the anisotropy energy increased indicating the prominent easy axis switching, as shown in Figure 3.6.

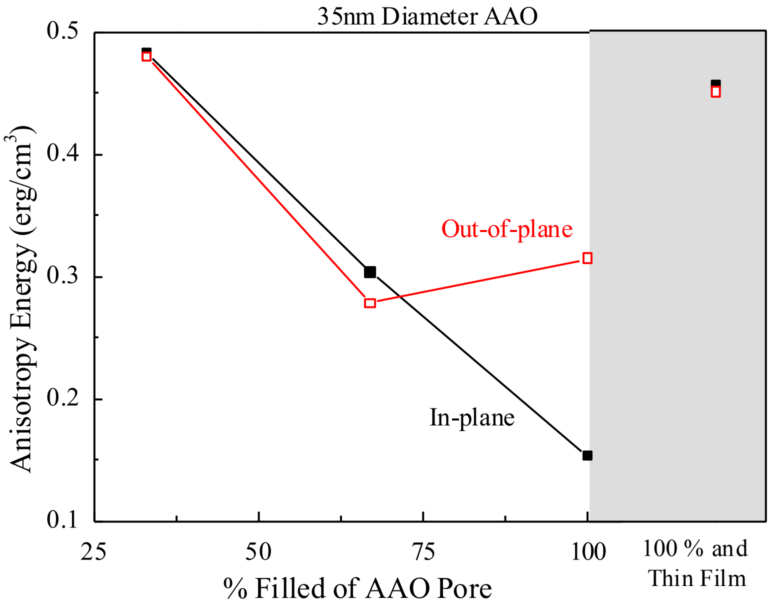

Figure 3.6 Magnetic anisotropy energy of 1D CFO nanostructures at different degree of filling in the 35 nm diameter pores of AAO

In summary, anodic aluminum oxide membranes with 18nm, 35nm and 80nm diameter pore were used to form CFO nanotubes and nanopillars via radical-enhanced atomic layer deposition. The presented work provided a simple and inexpensive route to create organized, high aspect ratio magnetic nanostructures in the prospect of studying magnetic anisotropies as well as the potential for integration into more complex multiferroic systems. The change in magnetic easy axis of CFO nanotubes from in-plane (partially filled) to out-of-plane when nanopillars were formed (100% filled) indicated the significance of the geometric factor in controlling magnetizations. The reduced magnetic shape anisotropy with increasing nanopillar diameter illustrated a potential path for engineering voltage-controlled magnetization switching effect in memory applications. With the use of ALD in AAO, only the deposition thickness can be controlled. While the structure is dictated by the synthesis of AAO membranes, it is important to control structural features to create smaller pores for maximizing the magnetic anisotropy.

CHAPTER 4 Magnetoelectric Coupling in Strain-Mediated of $CoFe_2O_4$ /$Pb(Zr,Ti)O_3$ 0D-3D Nanocomposite

Among different structures of multiferroic composites, 0D-3D was proposed due to the high interfacial coupling area. In this chapter, mesoporous structure of piezoelectric PZT was filled with magnetostrictive CFO to in order to achieve magnetoelectric coupling. Upon increasing filling of the pore neck in the porous structure, the mechanical flexibility decreased and restricted the strain transfer from one phase to another. High-resolution XRD showed the 33% filling of the pore neck yields the highest converse magnetoelectric coupling of 1.2×10^{-5} Oe-cm/mV. The saturation magnetization value was decreased by 42%. Upon electrical bias, the PZT lattice was compressed while the CFO lattice was expanded. The tuning of the intrinsic strain in the mesoporous composite can be used to optimize the magnetization easy axis from in-plane to out-of-plane.

4.1 Growth and Characterizations of 0D-3D CFO/PZT Composite

The multiferroic composite was prepared by combining sol-gel synthesis of PZT to create a three-dimensional and mesoporous ferroelectric template, and subsequently filled with ferromagnetic CFO by radical-enhanced atomic layer deposition. First, the growth and the intrinsic properties of the materials are studied.

The synthesis of mesoporous PZT was accomplished by using sol-gel method with amphiphilic diblock copolymer as the self-assembling agent. The precursors used were lead(II) acetate, zirconium butoxide, titanium isopropoxide, and poly(butadiene (1,4 rich)-*block*--poly(ethlyene oxide) as described in Chapter 2. The Pt(111)/TiO_x/SiO_2/Si substrate was dip-coated at a withdrawal rate of 2 mm/s. The (111)-oriented Pt layer allowed epitaxial growth of (111)-oriented PZT and crystallization of PZT into perovskite phase after rapid thermal annealing (Brooks 1994).

To confirm PZT has the correct stoichiometric ratio, the composition was investigated by XPS, as shown in Figure 4.1. The spectra were corrected based on C 1*s* peak at 284.8 eV. Both as-deposited (black curve) and annealed (red curve) samples were measured. The decreased amount of carbon content before and after annealing indicated the removal of organic polymers during the burn off process, which was consistent with the morphology change as observed in SEM. Since XPS is surface sensitive, little signal was detected from the underlying PZT From of the as-deposited sample. After the removal of the organic polymer, the photoemission peaks of Pb, Zr, and Ti were observed. From the spectra of Pb, the peak positions for Pb $4f_{5/2}$ and Pb $4f_{7/2}$ were at 142.8 eV and 138.0 eV respectively (Pintilie 2015). The symmetrical peak shape indicates a single oxidation state of Pb. The position of the $4f_{7/2}$ peak was 1.1 eV higher binding energy than that of Pb metal, indicating the oxide form of Pb was detected. Zr $3d_{5/2}$ and Ti $2p_{3/2}$ were found at 181.6 and 457.8 eV, respectively. To determine the oxidation states of both Zr and Ti, the peak locations were compared against literature values. The $3d_{5/2}$ peak of Zr^0 and Zr^{4+} were found at 178.8 and 181.5 eV from literature (Anderson 1994, Powell 2012), while $2p_{3/2}$ peak of Ti^0 and Ti^{4+} were found at 454.0 and 458.5 eV (Siemensmeyer 1991, Haukka 1993). The literature values suggested both Zr^{4+} and Ti^{4+} were detected. The Zr to Ti ratio was determined to be 1:0.395.

The crystal structure was determined to be perovskite with no preferred orientation. From the XRD spectra shown in Figure 4.2, intense Pt (111) substrate peaks was found at 39.98°. Non-substrate diffraction peaks were found at 21.98°, 31.08°, and 43.64°. The peak locations matched with perovskite phase PZT that (100), (101), and (002) peaks were found at 22.01°, 30.92°, and 43.63° according to JCPDS 00-033-0784. The average grain size was calculated to be 17.6 nm using Scherrer equation.

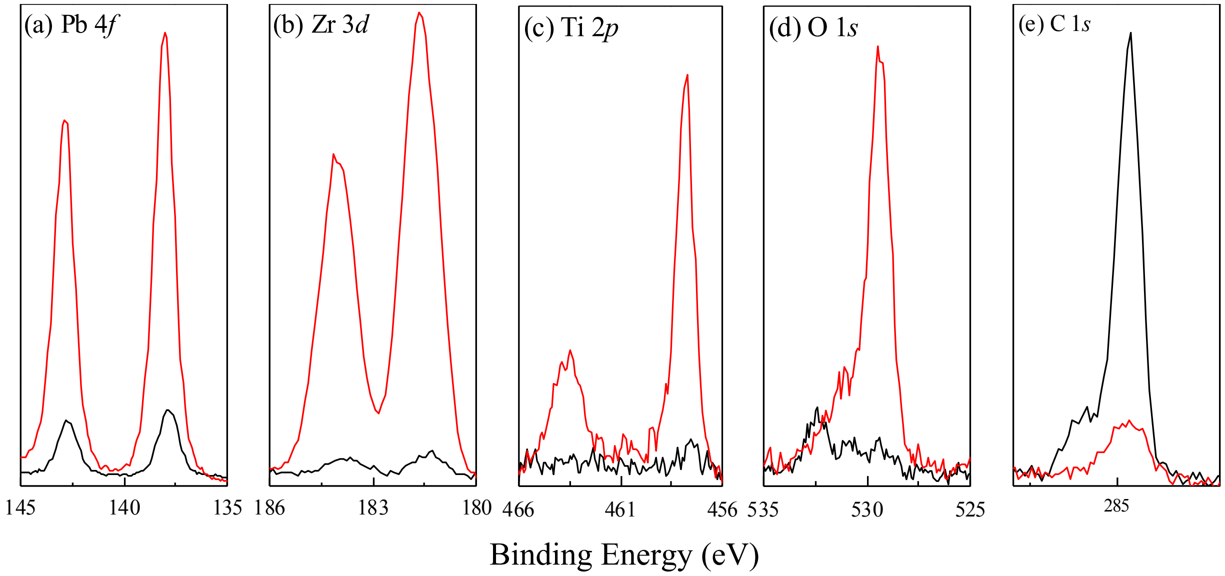

Figure 4.1 High resolution XPS spectra of (a) Pb 4*f*, (b) Zr 3*d*, (c) Ti 2*p*, (d) O 1*s*, and (e) C 1*s* from 100 nm thick of mesoporous PZT template on Si synthesized by EISA before (black) and after (red) rapid thermal annealing at 700 °C in air for 4 minutes.

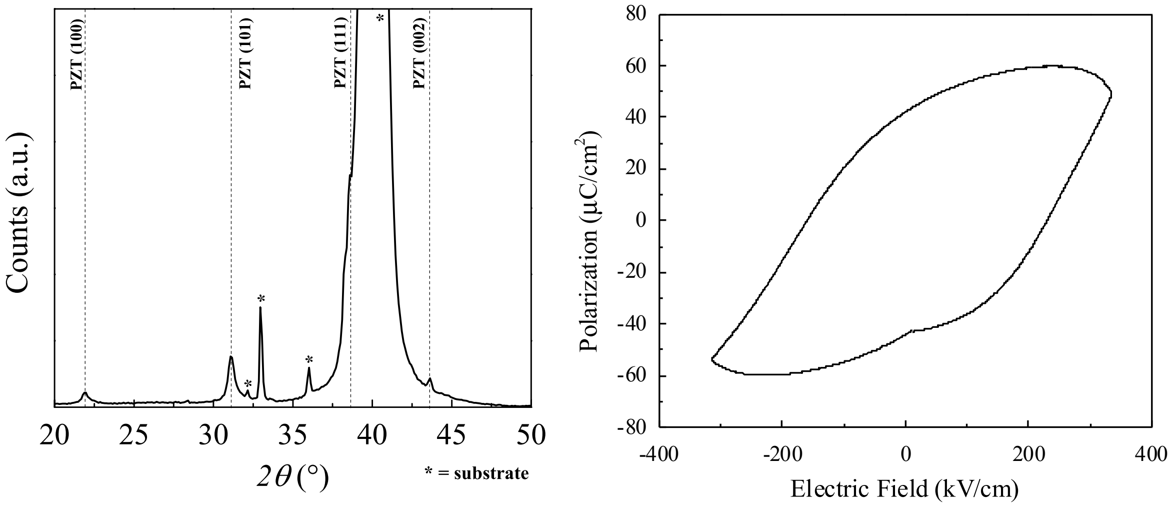

Figure 4.2 X-ray diffraction of the annealed mesoporous sample showed crystalline PZT (100) and (101) peak (left). Ferroelectric hysteresis responses of the annealed mesoporous PZT with 20 nm pore neck (100 nm thick) were measured through a Sawyer-Tower circuit at ±300 kV/cm with a saturation polarization of 60 μC/cm^2 (right).

The ferroelectric properties of the mesoporous PZT were measured using a Sawyer-Tower circuit. The remnant polarization was 42 and 44 μC/cm^2. The saturation polarization was about 60 μC/cm^2 at 300 kV/cm. The remnant polarization was in the same order of magnitude in comparison with literature at 30 μC/cm^2 (Udayakumar 1995). The coercivity of ~190 kV/cm was higher than the literature value of 31 kV/cm possibly due to the more difficult domain switching in the mesoporous structure. The non-ideal shape of the hysteresis was attributed to the leakage current within the structure. As higher electric field was applied, the increased leakage current generated a stronger screening field that counteracted polarizations, resulting in a lowered polarization values at both ends of the hysteresis. Nonetheless, the mesoporous PZT was shown to exhibit ferroelectric behaviors.

The mesoporous PZT was subsequently filled with CFO through RE-ALD in order to fabricate the 0D-3D nanocomposite. The SEM images in Figure 4.3 showed the change in surface morphologies after the depositions of various thicknesses of CFO. The PZT template was fully-filled when the porous structure was no longer visible. The degree of filling was then determined based on the number of ALD CFO cycles in compare to cycles required to fully fill the ferroelectric template.

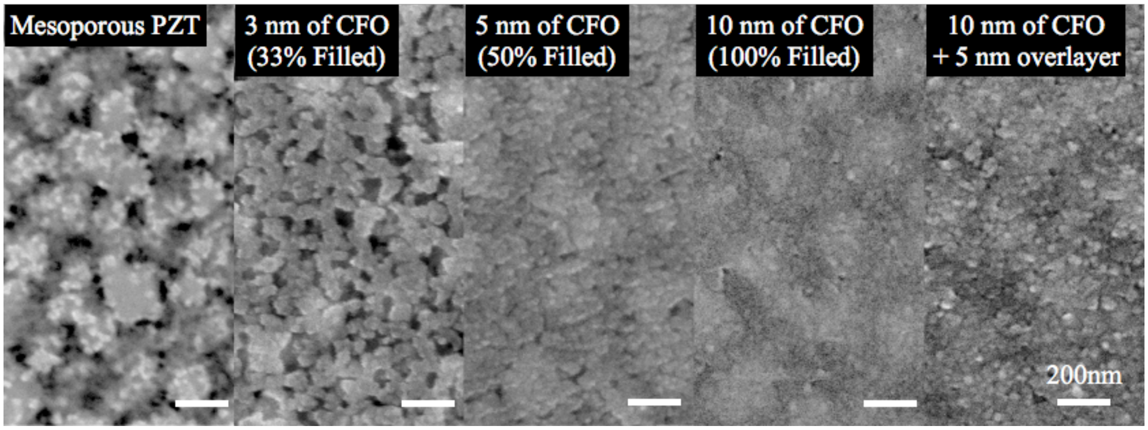

Figure 4.3 Top-down SEM images of mesoporous PZT with pore neck size of 20 nm at different degrees of pore neck filling using RE-ALD CFO.

4.2 Porosity Controlled Magnetic Easy Axis of 0D-3D CFO/PZT Composite

The magnetic properties were then investigated as a function of CFO pore neck filling. The in-plane and out-of-plane magnetizations from sample with three different degree of filling (33%, 67%, and 100%) were measured, as shown in Figure 4.4. The magnetic moment instead of the magnetization was shown in the y-axis due to the inability to accurately measure the volume of the magnetic material.

The coercivities in in-plane and out-of-plane directions increased as pore-neck filling increases. The coercivities were found to be 273 and 322 Oe respectively. The distinction of the out-of-plane easy axis was more apparent as the filling increases. At fully-filled, the coercivity increased to 1513 and 2248 Oe for in-plane and out-of-plane. The percentage difference was increased from 17.9% to 48.6%. The increase of coercivity with increasing CFO deposition could be attributed to the grain size dependence of the coercivity, as observed on NiFe thin films (2.5 – 30 nm) (Akhter 1997). However, that change in coercivity was relatively small which cannot be applied in this case. One explanation of the increase was the residual strain of the thin layer of CFO (10-20 nm). Liu has demonstrated an order of magnitude increase in coercivity of CFO powder through residual strain and defects (Liu 2006). With the thin film coating of CFO in the mesoporous structure, the extent of grain defects and dislocations of crystalline planes are inevitably increased due to the nanoscale pores. An enhanced coercivity was observed by Wang et. al. as CFO thin film thickness increases up to 100 nm, and decreases for films thicker than 100 nm (Wang 2004). Both in-plane and out-of-plane directions were observed to have an enhanced coercivity, which could correlate to the 0D-3D structure.

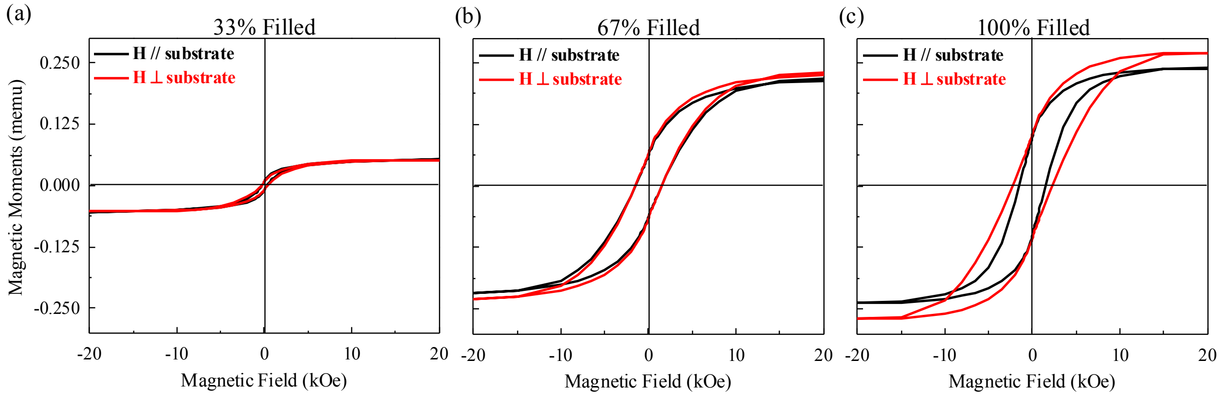

Figure 4.4 In-plane and out-of-plane magnetic properties of the 0D-3D CFO/PZT composite with (a) 33%, (b) 67%, and (c) 100% filling of the 20 nm PZT pore neck.

However, in CFO thin films, the in-plane coercivity was typically higher than that in out-of-plane direction due to shape anisotropy and pinning effect. While in the 0D-3D structure, the out-of-plane coercivity dominates, indicating both strain and thickness contributed to the coercivity enhancement. On the other hand, the saturation magnetizations were comparable in both directions at 33% filling. The difference was increased to 13.9% at 100% filling.

In order to verify the strain effects in coercivity of the composites at different degrees of filling, the lattice parameters were studied using high-resolution XRD at Stanford Synchrotron. The PZT (111) and CFO (311) peaks were selected as they have the highest signal-to-noise ratios among other diffraction peaks. Figure 4.5 shows the measured spectrum of the 33% filled CFO/PZT composite at different ex-situ poling voltages (0 V, 100 V, 300 V, and 1000 V). The peak was fitted using a 60% Gaussian and 40% Lorentzian distribution.

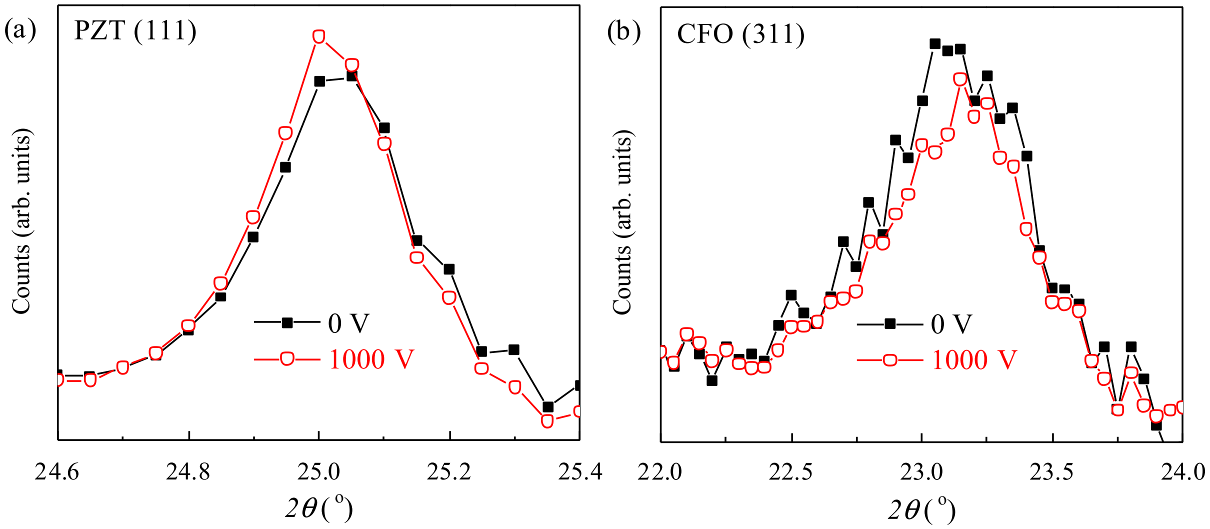

Figure 4.5 Out-of-plane high resolution XRD of (a) PZT (111) and (b) CFO (311) peaks at 0 and 1000 V *ex-situ* poling of the 33% filled CFO/PZT 0D-3D composite.

From the summary of peak positions, as shown in Figure 4.6(a), PZT was compressively strained while CFO was tensile strained in the in-plane direction. When there was no CFO deposition, the mesoporous PZT structure has a built-in compressive strain of 2060 με as compared against the d-spacing value of 2.351 Å from JCPDS 033-0784 of bulk PZT. Although the in-plane compressive strain could be caused by the lattice mismatch between the underlying Pt layer with a lattice parameter of 3.923 Å, which is lower than that of PZT of 4.036 Å (2.80% mismatch), it is more likely that the evaporation-induced self-assembling process had induced the strain from surface tensions. As an indication, the out-of-plane XRD pattern showed a greater compressive strain of 3190 με. When the pore necks were filled with CFO, the strain was reduced to 1350 με as 33% of the pore neck was filled with CFO. The compressive strain increases when more CFO was deposited up to 2250 με. Similar trend was observed in the out-of-plane direction. It indicated that the filling with CFO first relaxed and then compressed the PZT lattice. The strain was transferred from PZT to the deposited CFO as indicated from the increase of d-spacing. The CFO layer experienced an increasing in-plane tensile strain of 900 με at 33% filling to a 2540 με at 100% filled when compared against the d-spacing value of 2.531 Å from JCPDS 022-1086, which is similar to the strain observed in PZT. The out-of-plane measurements of CFO (311) were not observed since it overlapped with substrate peaks. Due to the nature of negative magnetostriction in CFO, the increased strain of CFO in the in-plane direction caused the out-of-plane magnetization an easier axis, hence a higher saturation magnetization and coercivity shown in Figure 4.4. The increasing strain in the CFO layer also coincides with the increasing differences of the hysteresis in both directions. As a result, the intrinsic strain, and hence the magnetic response, of CFO can be tuned by deposition thickness on mesoporous PZT.

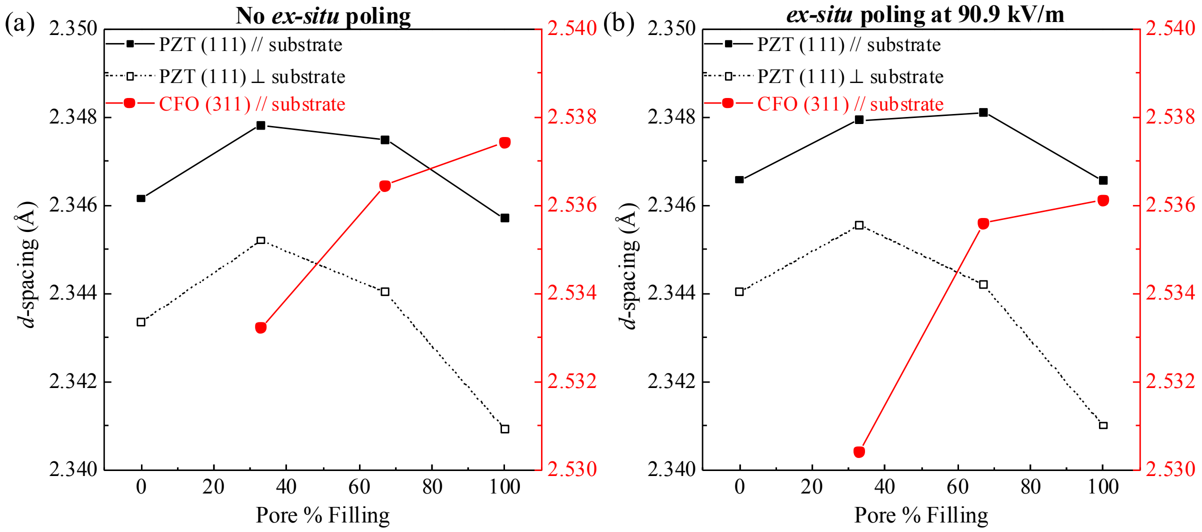

Figure 4.6 Fitted peak positions summary of in-plane PZT (111) and CFO (311) XRD peaks at 0%, 33%, 67%, and 100% pore-neck filling under (a) no *ex-situ* poling and (b) 90.9 kV/m *ex-situ* poling of the CFO/PZT mesoporous composite.

The effect of electrical poling of PZT on the change in CFO magnetization was accessed as the next step. The samples were poled in the out-of-plane direction at 90.9 kV/m for ten minutes immediately before high-resolution XRD measurements were performed. In Figure 4.6(b), the same compressive strain observed in PZT (111) spacing was relaxed in both in-plane and out-of-plane directions. The out-of-plane relaxation was the greatest with no CFO filled due to the unrestrained interface. Intermediate filling of CFO had a less ability to strain. When the porous structure was fully filled with CFO, the composite was unable to strain out-of-plane as indicated by the unchanged d-spacing value of PZT. On the other hand, the in-plane relaxation increases with increasing filling of the pore neck. It was noted that the electrical poling in the out-of-plane direction caused compressive strain in both directions of PZT due to the nature of the mesoporous structure.

The strain from the remnant polarization in the piezoelectric PZT was transferred to the magnetostrictive CFO, which results in change in magnetizations. The strain transfer from PZT to CFO was the most efficient when the composite was 33% filled with CFO, as evident by the greatest change in d-spacing of the CFO (311) plane. The in-plane strain was switched from tensile to compressive. The effect on the magnetic properties was shown in Figure 4.7. In the out-of-plane direction, the hysteresis responses had no noticeable change. However, the in-plane saturation magnetization was diminished to half of the original magnetization values after electrical bias at 90.9 kV/m. The converse magnetoelectric coupling coefficient was calculated to be 1.2×10^{-5} Oe-cm/mV. The coercivity was increased by more than two folds from 268.2 Oe to 709.4 Oe, indicating that the change from tensile to compressive strain in CFO drastically modified the magnetic strength in the corresponding direction.

For the composites with 67% and 100% of the pore neck filled, the *d*-spacing of CFO (311) decreased slightly similar to that observed in PZT because of reduced strain. The magnetic properties of the 100% filled composite were measured using SQUID as shown in Figure 4.8. In both directions, the saturation magnetization was slightly increased, which is more noticeable in the in-plane orientation. The coercivity was decreased from 2250 Oe to 1766 Oe and 1519 Oe to 1384 Oe after electrical poling respectively.

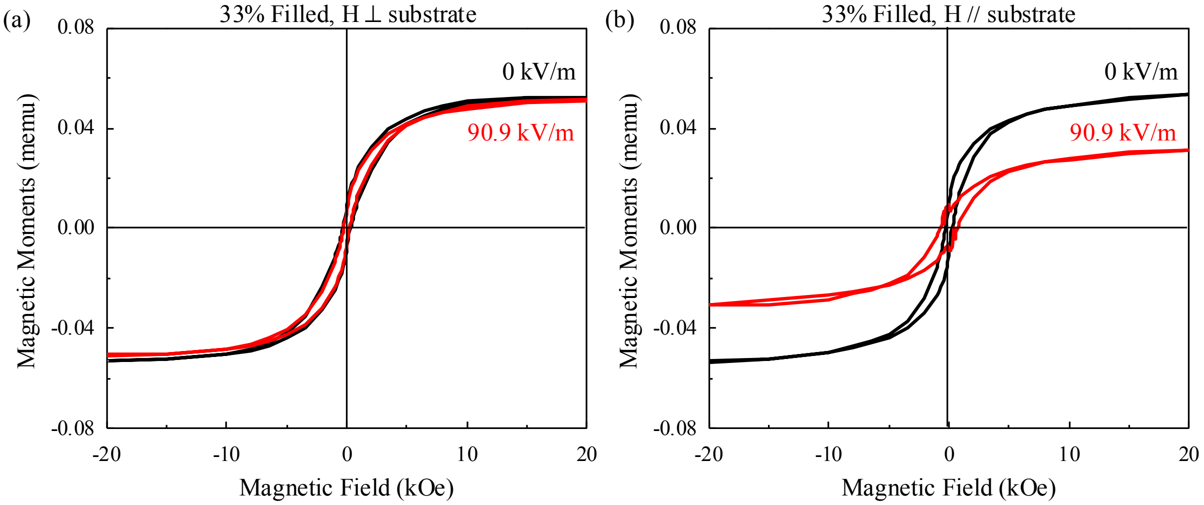

Figure 4.7 (a) Out-of-plane and (b) in-plane magnetic hysteresis loops of the 0D-3D CFO/PZT composite with 33% pore neck filling before and after *ex-situ* bias at 90.9 kV/m.

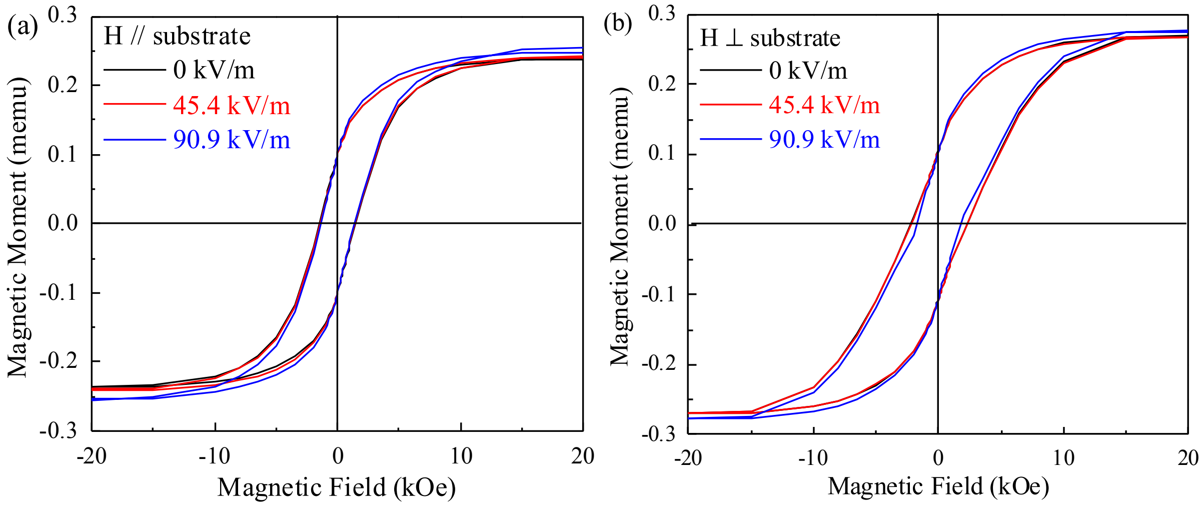

Figure 4.8 (a) Out-of-plane and (b) in-plane magnetic hysteresis loops of the 0D-3D CFO/PZT composite with 100% pore neck filling before and after *ex-situ* bias at 90.9 kV/m.

The results shown above were in coherent with the literature by Chien *et al.* on mesoporous CFO with ALD PZT filling (Chien 2016). The fabricated structure was the direct opposite to the structure fabricated in this work with a pore neck radius of 6 nm. Chien et al.

observed a more efficient strain transfer from PZT to CFO when half of the pore neck radius was filled, as evident by the magnetometry measurements under out-of-plane electrical poling. It agrees with the observations in this work that a partially filled composite retained more mechanical flexibility. In both structures, the saturation magnetization was decreased while the coercivity was increased. However, in-plane magnetization change was observed in the mesoporous PZT structure in opposed to out-of-plane magnetization change in the mesoporous CFO structure. One possible explanation was the fact that the increased amount of PZT would yield larger in-plane grain size and possibly increase the ability to retain a higher remnant polarization. The converse magnetoelectric coupling coefficient was calculated to be 1.2 × 10^{-5} Oe-cm/mV as compared to 1 × 10^{-5} Oe-cm/mV from the literature where 100 nm thick of mesoporous CFO (pore neck size of 5 nm) was coated with 3 nm of ALD PZT (Chien 2016). The reduced value could be accounted by the volume difference in the magnetic CFO

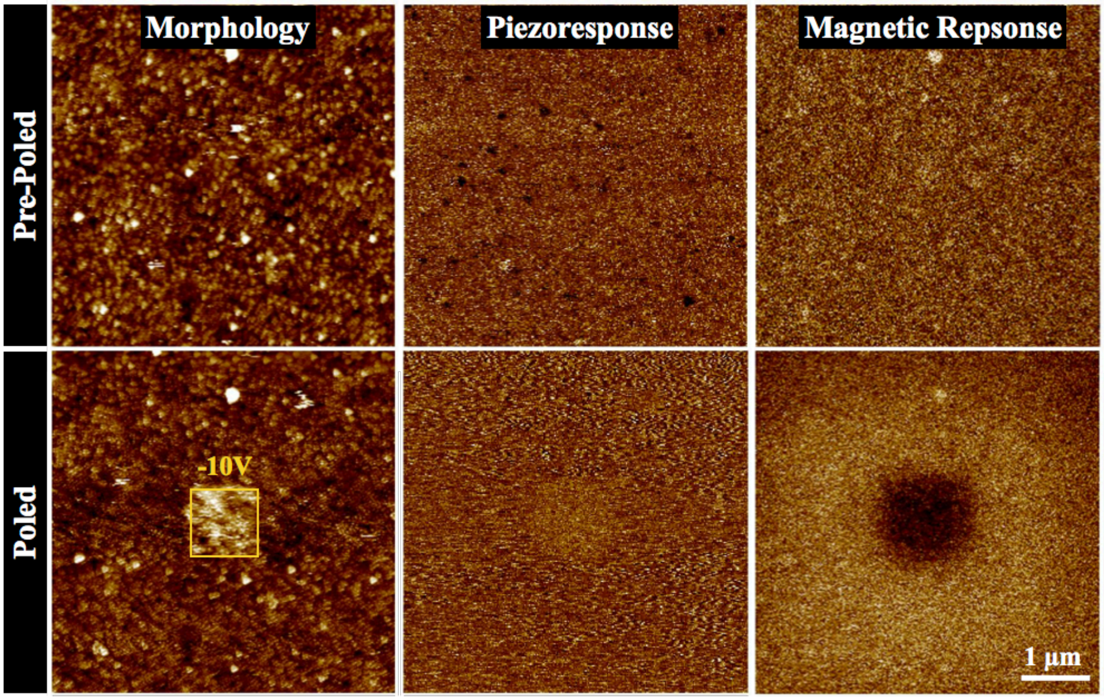

Figure 4.9 AFM/PFM/MFM measurement of 0D-3D CFO/PZT meosporous composite (33% pore neck filling). The 1 x 1 µm^2 was electrically poled at -10V.

As a visualization of the magnetoelectric coupling, a combined AFM/PFM/MFM studies was performed. The morphology, piezoresponse and the magnetic responses of the 33% filled composite were shown in Figure 4.9. The 5 x 5 μm^2 area was measured before electrical poling. After the central 1 x 1 μm^2 was poled with a -10V, the surface was elevated in the normal direction by 2-5 nm, while some remnant piezoresponse was observed. The magnetic response of the CFO was probed. The poled area was observed to have magnetization orientation switched to predominantly out-of-plane while the surrounding area had an antiparallel magnetization orientation as a result of the magnetoelectric coupling.

In summary, these experiments indicated that magnetoelectric coupling can be achieved in nanostructured thin film by combining ALD CFO process into template mesoporous PZT. Through careful tuning of the intrinsic strain of the PZT in the composite, the magnetization can be optimized. The strain transfer between the two phases was more efficient when the PZT pores were partially filled that yields mechanical flexibility, and hence a stronger ME coupling than the 100% filled PZT/CFO composite. In this work, the pore neck size was fixed due to the use of the same diblock copolymer. Nonetheless, it has shown that the mechanical flexibility is a key factor in controlling the ME coupling. From the d-spacing analysis, the porosity of the composite should further enhance the strain transfer between the two materials that could potentially increase ME coupling. Future experiment should focus on the effect of porosity as a function of pore neck size to elucidate its correlation to ME coupling .

CHAPTER 5 Magnetoelectric Coupling in Strain-Mediated $CoFe_2O_4$/Pb(Zr,Ti)O_3 1D-3D Nanocomposite

CFO/PZT nanocomposites were grown in anodic aluminum oxide (AAO) membranes with pore diameter of 40 nm, via radical-enhanced atomic layer deposition (RE-ALD) and thermal ALD to study magnetic shape anisotropy and ME coupling of the core-shell magnetic structure. The deposition was achieved using TMHD precursors (TMHD = 2,2,6,6-tetramethyl-3,5-heptanedionate) at 200°C with a growth rate of 2.41 and 10.0 Å/cycle for CFO and PZT respectively. Amorphous nanotube arrays were annealed at 550°C. By controlling the CFO to PZT volume ratio and the core-shell structure, the converse ME coupling coefficient of 1.3×10^{-4} Oe-cm/mV was achieved, which was higher than the target value of 4×10^{-5} Oe-cm/mV.

5.1 Magnetic Anisotropy of 1D-1D CFO/PZT Nanostructures

The multiferroic 1D-3D CFO/PZT composites were prepared by combining the ALD processes as mentioned in Chapter 2.1. Depending on the structure being studied, either ALD PZT or CFO was deposited first into the AAO substrate. In Figure 5.1, CFO with thicknesses of 5, 10, and 20 nm were deposited into the 40 nm diameter pores of AAO. The morphology of the surface became rougher with deposition in between pores as shown by the lighter spots after 5 nm of CFO deposition, while the majority of the surface remained smooth. Subsequent growth of the grains of the CFO after 10 nm and 20 nm thickness depositions was observed. Similarly, 5, 10, and 20 nm of PZT were deposited into the blank AAO. The morphology was very different from CFO. A much smoother surface was observed after 10 nm of PZT was deposited. Thin film PZT was seen in between pores with triangular shape after 20 nm of PZT deposition, indicating the pores were completely filled and the growth was predominately at the surface.

The difference in morphology between ALD CFO and ALD PZT was caused by the fundamental difference in radical enhanced and thermal ALD. As described in Chapter 3, radicals were generated by the plasma inside the quartz ampoule. The energetic species tend to recombine upon collision and therefore unable to penetrate the entire AAO substrate. By contrast, PZT has a relatively more uniform thickness inside the porous structure.

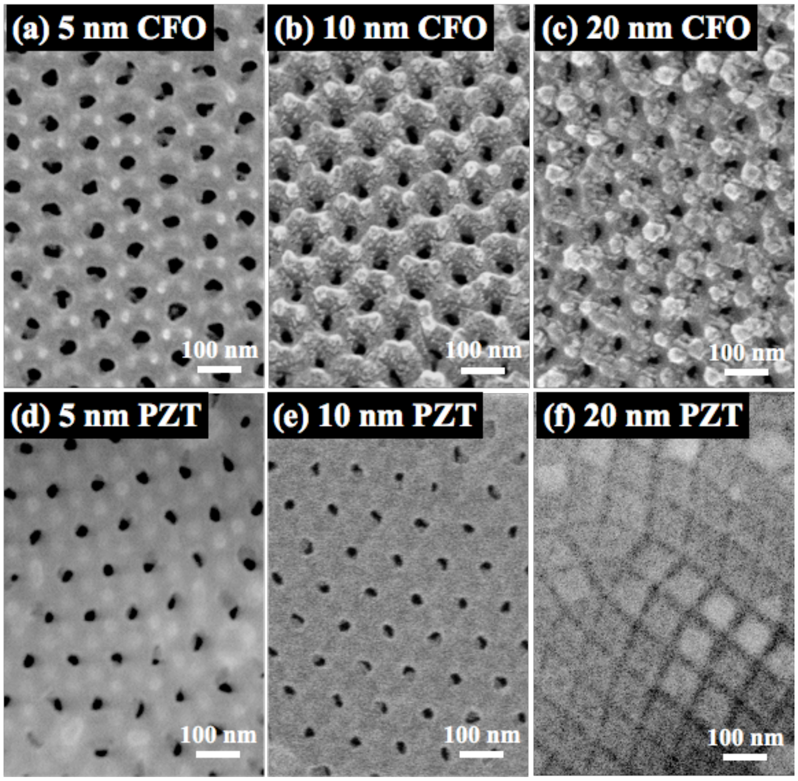

Figure 5.1 Top-down surface morphologies of AAO with diameter of 40 nm and subsequent filling with 5 nm, 10 nm, and 20 nm of (a-c) RE-ALD CFO and (d-f) thermal ALD PZT, respectively. The morphology difference originated from the nature of REALD and thermal ALD

Four PZT-core CFO-shell samples were synthesized for studying magnetic shape anisotropy of the 1D-1D composite. 5 nm, 10 nm, 15 nm, and 20 nm of CFO were deposited inside the AAO (40 nm pore diameter). The samples with open pores were fully filled with ALD PZT and subsequently annealed at 700 °C for 1 minute for crystallization.

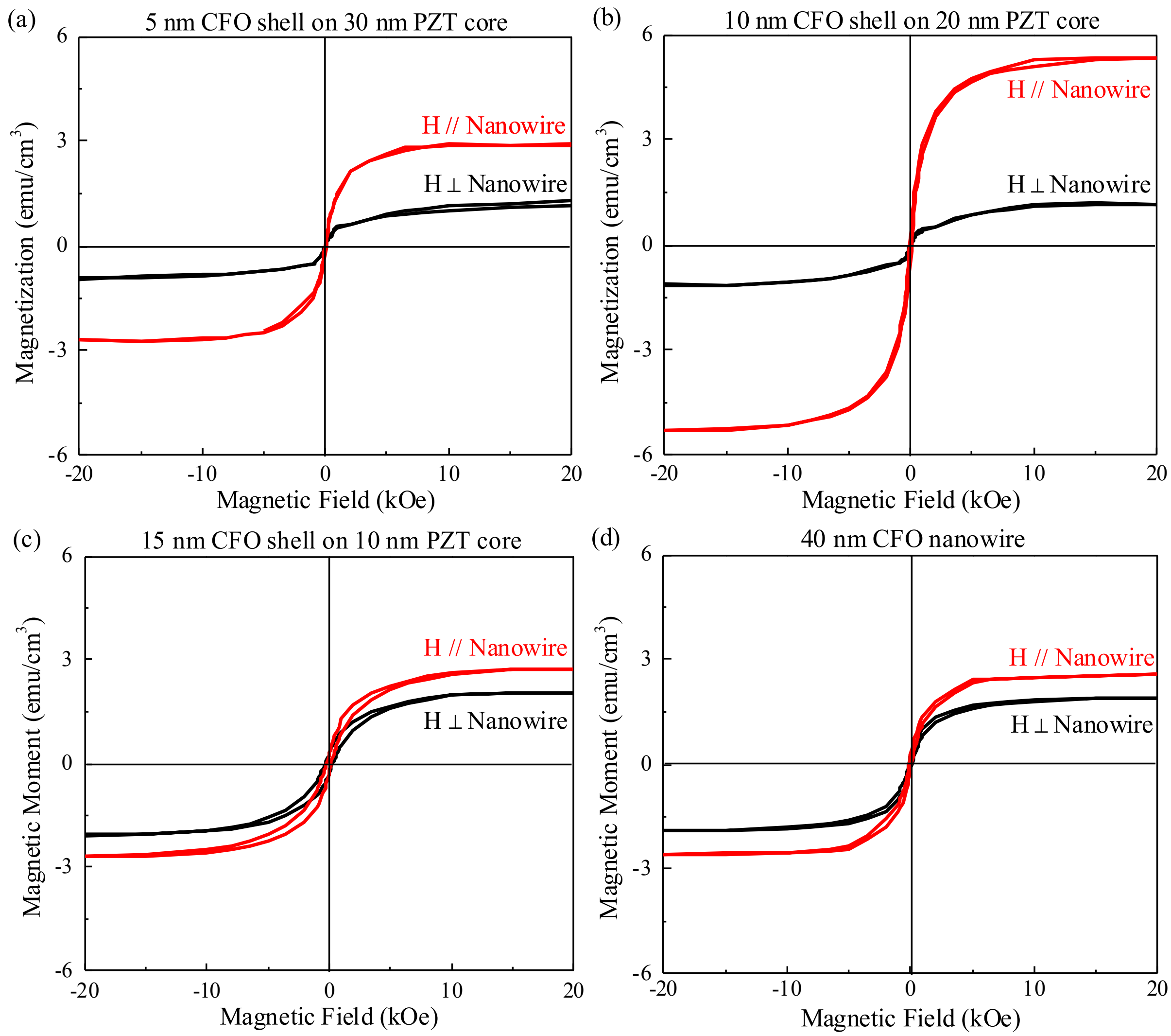

Figure 5.2 Parallel and perpendicular magnetic responses of CFO/PZT nanowires deposited in AAO (40 nm pore) with (a) 5 nm, (b) 10 nm, (c) 15 nm, and (d) 20 nm of CFO deposition. The core was deposited fully with ALD PZT except (d).

The magnetic shape anisotropy of the 1D-1D CFO/PZT composites were characterized through magnetometry studies. Figure 5.2 shows the magnetic hysteresis of the four different samples. In order to look at the effect of the CFO shell thicknesses on magnetic shape anisotropy, the magnetic responses were normalized by an approximated CFO volume. According to the SEM images as shown in Figure 5.1, the density of the pores was estimated to be 1.25 x 10^{10} pores/cm^2. The estimation can be achieved by pore counting divided by the SEM image dimensions using software such as ImageJ. With the penetration length of 1 μm of the ALD CFO process as shown in Chapter 3, the total CFO volume of a 1 x 1 cm^2 sample can be approximated. As a baseline, the magnetic response from the CFO nanowires of 40 nm diameters in Figure 5.2(d) has a self-consistent trend with the result shown in Figure 3.4(c), indicating the reproducibility of the magnetic shape anisotropy. The saturation magnetization along the nanowire was 1.3 times higher in the long axis than the short axis.

The hysteresis loops from Figure 5.2(a)-(c), on the other hand, represent the effect of a core-shell structure and PZT deposition on magnetic anisotropy. According to Figure 3.4(a)-(b), CFO nanotubes synthesized in AAO (35 nm pore diameter) has shown an easy axis predominantly perpendicular to the long axis of the nanotubes, which was attributed to the magnetic moments from the CFO thin film on the top planar surface. The magnetic moments inside the nanotube could potentially align along the annular surface, that the net moment along the nanotube was small relative to the top surface. The lower signal-to-noise ratio should also be noted. After the deposition of PZT, the easy axis was switched from perpendicular to parallel to the long axis of the core-shell structures. The saturation magnetization values along the nanowires of the structures with 5 nm, 10 nm and 15 nm CFO shells were 2.3, 4.5 and 1.3 times higher than that of perpendicular to the nanowires, respectively. A summary of the coercivities, saturation magnetizations and remnant magnetizations is shown in Table 5.1.

One possible explanation resides in the strain state of the CFO. From the d-spacing analysis of Figure 4.6, the magnetic easy axis of CFO was found when it was compressed due to negative magnetostriction. While the aluminum oxide template was amorphous, the lattice mismatch between PZT (3.91-4.04 Å) and CFO (8.39 Å) could cause compressive strain along the long axis of the nanowires, resulting in the enhanced magnetic anisotropy

The composite structure with 15 nm CFO shell on 10 nm PZT core had increased magnetic saturation to a 40 nm diameter CFO nanowires. The saturation magnetizations of the parallel and perpendicular orientations were 2.74 emu/cm^3 and 2.29 emu/cm^3 respectively. They were slightly higher than that from the CFO nanowires of 2.57 emu/cm^3 and 1.94 emu/cm^3. It indicated that the magnetic moment were comparable. The coercivities of the CFO/PZT composite, however, were doubled in both orientations. A higher coercivity in the perpendicular direction suggested that the parallel orientation was an easier axis of the composite, which requires less energy for magnetization switching.

The composite structure with 10 nm CFO shell on 20 nm PZT core had a doubled saturation and remnant magnetization parallel to the nanowires than that from a 40 nm CFO diameter CFO nanowires. One possible reason could be the magnetic domain size of the CFO of about 10 nm, beyond which the domains are antiparallel and cancels the magnetic moments. The saturation and remnant magnetization in the perpendicular orientation was about half at 0.10 and 0.17 emu/cm^3 respectively. It further indicates the magnetic shape anisotropy is the highest at this volume ratio. From the theoretical analysis in Chapter 1, the optimal ME coupling of a 1D-1D PZT-core-$NiFe_2O_4$ structure occurs at 0.15 volume ratio of PZT. In this particle sample the volume ratio of PZT was 0.25. Consider a higher magnetostrictive coefficient of CFO at -164 με in compared with -29 με for $NiFe_2O_4$, the ideal composition for ME coupling would shift to a higher volume ratio of PZT.

The coercivities of the composites increase as the CFO shell thickness increases from 5 nm to 15 nm. With a 5 nm shell, the coercivity and remnant magnetization were close to zero possibly due to the inability to retain magnetic moment in the perpendicular direction on the ultra thin shell. When the shell thickness was increased to 10 nm, the coercivities were comparable in both directions. The remnant magnetization along the nanowires was more than three-folded as an indication of the easy axis. While the saturation magnetizations in the perpendicular direction for both 5 nm and 10 nm shells were comparable, the value of parallel direction was significantly increased to 5.30 emu/cm^3. It suggested 10 nm CFO shell on a 20 nm PZT core has an optimal volume ratio between CFO and PZT in maximizing the difference in direction-dependent saturation magnetization.

Table 5.1 SQUID magnetometry results of the PZT-core CFO-shell structures formed in AAO with pores of 40 nm diameter.

	Parallel to nanowire			Perpendicular to nanowire		
	H_c (Oe)	M_r (emu/cm^3)	M_s (emu/cm^3)	H_c (Oe)	M_r (emu/cm^3)	M_s (emu/cm^3)
5 nm CFO / 30 nm PZT	45	0.12	2.89	/	/	1.20
10 nm CFO / 20 nm PZT	83	0.39	5.30	77	0.10	1.17
15 nm CFO / 10 nm PZT	182	0.26	2.74	282	0.28	2.29
40 nm CFO	96	0.21	2.57	138	0.19	1.94

In summary, magnetic easy axis was switched from perpendicular to parallel orientation of the nanowires by structural tuning and the deposition of PZT. The core-shell structure with 15 nm of CFO had similar saturation magnetization to a 40 nm CFO nanowire structure. The highest magnetic anisotropy was observed in the core-shell structure with 10 nm of CFO on a 20 nm PZT core.

5.2 Core-shell Structural Control of Magnetoelectric Coupling in 1D-1D $CoFe_2O_4$ Nanostructures

After the studies of the structural control and deposition of PZT on magnetic shape anisotropy, the ME coupling of the composite was investigated as a function of the CFO shell thickness. The three samples were *ex-situ* electrically poled at 0.27 MV/m and 0.54 MV/m along the nanowires for 10 minutes before magnetometry measurements.

The sample with 15 nm of CFO shell deposited on 10 nm of PZT core demonstrated the least enhancement in ME coupling, as shown in Figure 5.3. With the lowest amount of PZT, it has the least ability to respond to electric field and strain. The latter was hinted from the similarities of the hysteresis in Figure 5.2(c) and (d). The saturation magnetization in the parallel orientation was decreased from 2.74 emu/cm^3 to 2.17 emu/cm^3, while that in the perpendicular orientation was increased from 2.29 emu/cm^3 to 2.71 emu/cm^3 at 0.54 MV/m. It suggested that the tensile strain from the PZT along the nanowires was transferred to CFO after poling. The negative magnetostrictive CFO experienced the tensile stress along the nanowires and therefore the magnetization was reduced, whereas the compressive stress in perpendicular to the nanowires enhanced the magnetization. The converse ME coupling coefficient was not observable at 0.27 MV/m, and a value of 2.8×10^{-5} Oe-cm/mV at 0.54 MV/m. The value was 70% of the target value, which was lower than expected limited by the high voltage applied. The ME coupling could further be improved by increasing the amount of PZT as it was not fully strained before electrical breakdown

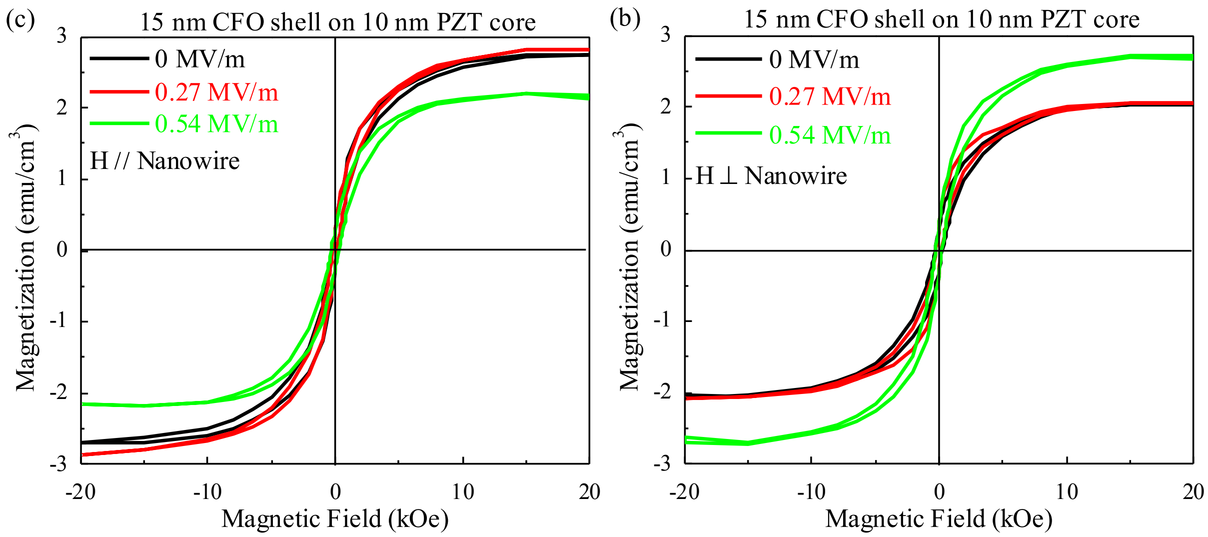

Figure 5.3 Magnetic hysteresis responses of 10 nm PZT core and 15 nm CFO shell 1D-1D nanotubes (a) in parallel and (b) perpendicular to applied magnetic field after *ex-situ* poling at 0 MV/m, 0.27 MV/m, and 0.54 MV/m.

Similarly, the sample with 10 nm of CFO shell deposited on 20 nm of PZT core demonstrated a cohesive change, as shown in Figure 5.4. The saturation magnetization parallel to the nanowires was decreased from 5.30 emu/cm^3 to 2.32 emu/cm^3, and was increased from 1.17 emu/cm^3 to 3.15 emu/cm^3 in the perpendicular orientation. The converse ME coupling coefficient was calculated to be 6.6 × 10^{-5} Oe-cm/mV at 0.27 MV/m, which exceeded the target value of 4 × 10^{-5} Oe-cm/mV by more than 50%. Due to the more dielectric nature of PZT than CFO, the increased amount of PZT allowed to establish a higher electric field across the composite, resulting in a higher strain state and converse ME coupling. The strain transfer between the two phases was saturated at 0.27 MV/m, beyond which the piezoelectric response of PZT was small and little change was observed in hysteresis at 0.54 MV/m.

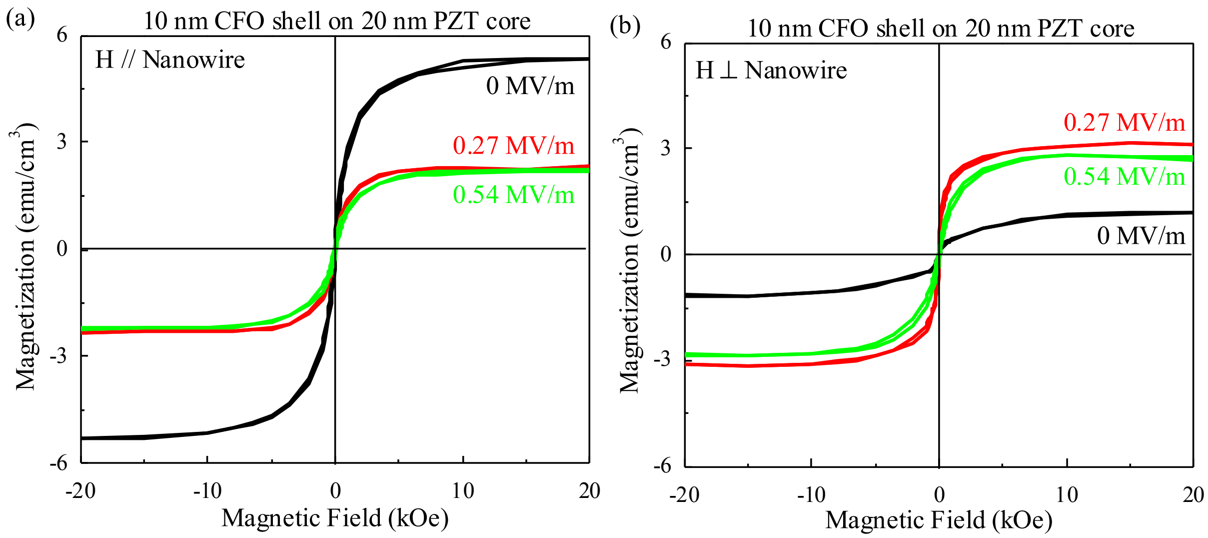

Figure 5.4 Magnetic hysteresis responses of 20 nm PZT core and 10 nm CFO shell 1D-1D nanotubes (a) in parallel and (b) perpendicular to applied magnetic field after *ex-situ* poling at 0 MV/m, 0.27 MV/m, and 0.54 MV/m.

For the ultra thin shell of 5 nm CFO on a 30 nm PZT core, saturation magnetization increases in both orientations, as shown in Figure 5.5. The saturation magnetization parallel to the nanowires was increased from 2.89 emu/cm^3 to 7.88 and 10.98 emu/cm^3 after electrical poling at 0.27 MV/m and 0.54 MV/m respectively. This increasing trend was opposite to what was expected and that observed from previous samples. The converse ME coefficient was calculated to be 1.3×10^{-4} Oe-cm/mV, which was three-folded of the target value. When tensile strain was induced from PZT along the nanowires after electrical poling, the negative magnetostrictive CFO would experience a reduction in magnetization from the tensile strain. However, the magnetization was increased with an ultra thin CFO shell.

On the other hand, the saturation magnetization in the perpendicular orientation was increased from 1.20 emu/cm^3 to 1.60 and 3.34 emu/cm^3. Interestingly, these values were comparable to that from the sample with 10 nm of CFO deposited on 20 nm PZT core. It indicates that the strain induced from the 20 nm of PZT was already sufficient to manipulate the magnetization of the CFO perpendicular to the nanowires. From the study in Chapter 4, the deposition of PZT on CFO induced residual tensile strain, which was increased with the volume of PZT from 900 to 2570 με. In both mesoporous CFO/PZT and CFO/PZT in AAO, the interfacial area between the two phases remained unchanged. While the residual tensile strain resides along the interfacial area, the electrically induced tensile strain of PZT combined with the residual strain in the direction parallel to the nanowires. That could potentially lead to an excessive strain existed along the nanowires and result in dramatic change in the magnetization behavior. In the case of an ultra thin CFO shell, spin cancellation between the iron ions at octahedral and tetrahedral sites could be altered under excessive strain. It was shown in the literature that a portion of the Co^{2+} ions at the octahedral sites could occupy the tetrahedral sites at nanoscale below 15 nm, resulting in a different spin-cancelling environment (Giri 2002) and therefore a different trend in saturation magnetization.

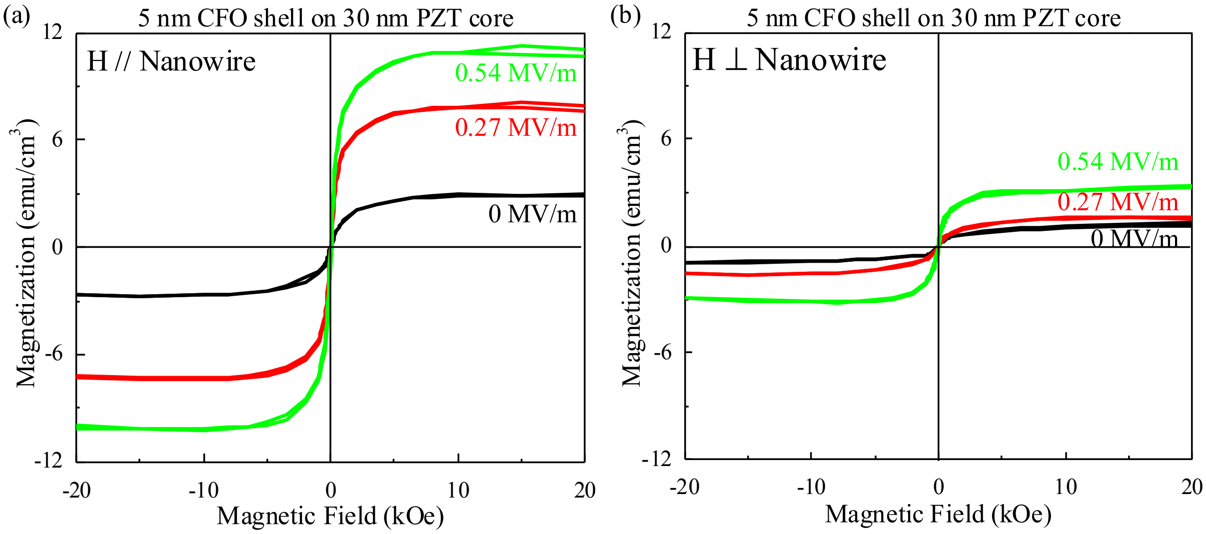

Figure 5.5 Magnetic hysteresis responses of 30 nm PZT core and 5 nm CFO shell 1D-1D nanotubes (a) in parallel and (b) perpendicular to applied magnetic field after *ex-situ* poling at 0 MV/m, 0.27 MV/m, and 0.54 MV/m.

In comparing the three different core-shell structures, the magnetization parallel to the nanowires increases after electrical bias with decreasing CFO shell thickness, while the magnetization perpendicular to the nanowires remained below 3 emu/cm^3. It was a promising trend that indicates a more effective strain transfer as the PZT volume increases and the CFO shell thickness decreases.

In summary the magnetoelectric coupling of the PZT-core CFO-shell structure was investigated as a function of the electrical field and CFO shell thickness. For the sample with the thinnest shell and highest volume of PZT, the magnetizations were increased in both orientations indicating effective strain transfer and enhancement in converse ME coupling coefficient, exceeding the research target of 4 × 10^{-5} Oe-cm/mV to 1.3 × 10^{-4} Oe-cm/mV. The summary of converse ME coupling coefficients is shown in Table 5.2. Although further experiments are needed to explain the incoherent trend, it was proven that the 1D-1D nanostructure introduced magnetic anisotropy and can be further optimized for converse ME coupling.

Table 5.2 Converse ME coefficients of strain-mediated multiferroic composite 2D-2D and 1D-3D nanostructures

FE	FM	Type (D-D)	ME coef. α_{CME} (Oe-cm/mV)	Critical Dimension (nm)	Reference
BTO	Ni	2-2	5×10^{-10}	100	(Gepras 2010)
BFO	CoFe/Cu/CoFe	2-2	3×10^{-5}	100	(Heron 2014)
BTO	LSMO	2-2	2.3×10^{-5}	40	(Eerenstein 2007)
PMN-PT	LSMO	2-2	6×10^{-6}	20-50	(Thiele 2007)
PMN-PT	Fe_3O_4	2-2	6.7×10^{-5}	900	(Liu 2009)
PMN-PT	CFO	2-2	3.2×10^{-6}	200	(Yang 2009)
PZT	CFO	0-3	1.1×10^{-6}	100	(Peng 2015)
PZT	CFO	0-3	1×10^{-5}	6	(Chien 2016).
PZT	**CFO**	**0-3**	$\mathbf{1.2 \times 10^{-5}}$	**5**	**This work**
BFO	CFO	1-3	1×10^{-5}	200	(Zavaliche 2005)
PZT	CFO	1-3	4×10^{-5}	80	(Ren 2008)
PZT	**CFO**	**1-1**	$\mathbf{2.8 \times 10^{-5} – 1.3 \times 10^{-4}}$	**5-15**	**This work**

CHAPTER 6 Summary

The optimizations of magnetoelectric coupling in multiferroic composites were demonstrated using different nanostructuring techniques. The remarkable tunabilities in their ferromagnetic and ferroelectric have provided the potential in enabling the control of magnetizations by electric field for integrations into commercial applications.

In this work, radical-enhanced ALD of CFO and thermal ALD of PZT were combined to enable complex multiferroic architectures in investigating the effect of nanostructuring and magnetic shape anisotropy on improving ME coupling. In particular, (1) 1D CFO nanotubes and nanowires; (2) 0D-3D CFO/PZT mesoporous composite; and (3) 1D-1D CFO/PZT core-shell nanowire composite were studied.

The synthesis of 1D CFO nanostructures was realized by ALD of CFO in anodic aluminum oxide (AAO) membranes with cylindrical pores of 18 nm, 35 nm and 80 nm in diameter. This work provided a simple and inexpensive route to create parallel and high aspect ratio of 56 magnetic nanostructures. The morphology and magnetic properties of partially filled pores (nanotubes) and fully filled pores (nanowires) were studied using SEM and SQUID. It was observed that as the wall thickness increases, the magnetic easy axis of the CFO nanotubes was changed from perpendicular to parallel when nanowires were formed. It has demonstrated the significance of the geometric factors in controlling magnetizations. The easy axis could potentially be manipulated if coupled to a piezoelectric material for device applications.

In the next step, an isotropic 0D-3D CFO/PZT mesoporous structure was synthesized to investigate also the effect of interfacial area for converse ME coupling. 100 nm of mesoporous PZT was synthesized on $Pt/TiO_x/SiO_2/Si$ using amphiphilic diblock copolymers to provide a porous ferroelectric template with 10 nm pores for ALD CFO growth. Increasing filling of the mesoporous PZT with CFO introduced in-plane compressive strain in PZT and tensile strain in

CFO, which modified the out-of-plane magnetic properties due to negative magnetostrictive CFO. On the other hand, the increased amount of CFO decreased the mechanical flexibility of the composite when strain was induced by electric field in PZT. Hence, ME coupling was mitigated. The highest converse ME coefficient of 1.2×10^{-5} Oe-cm/mV was achieved with a 33% pore filling of CFO, in compare to a 1×10^{-5} Oe-cm/mV from mesoporous CFO filled with 6 nm of PZT in literature (Chien 2016). It has demonstrated that converse ME coupling and strain transfer between the ferroelectric and ferromagnetic phases could be optimized by the precise filling of the 0D-3D mesoporous structure.

In further optimization of converse ME coupling through nanostructuring, highly directional 1D-1D PZT-core CFO-shell multiferroic composite was synthesized. 5, 10, and 15 nm CFO shell were deposited inside the 40 nm pores of the AAO templates using radical enhanced ALD, while PZT was subsequently deposited to complete the core-shell structure. It has demonstrated the magnetic shape anisotropy of the nanostructure was controlled by the volume ratio of the two phases. The CFO shell thickness allowed the tuning of magnetic easy axis and saturation magnetizations; whereas the PZT volume allowed the optimization of electric field induced strain of the composite. An enhanced converse ME coupling of 1.3×10^{-4} Oe-cm/mV was realized by 5 nm CFO shell on 30 nm of PZT core.

In summary, the work has demonstrated nanostructuring of multiferroic composite is an effective pathway to engineer converse ME coupling through optimizations of both magnetic shape anisotropy and interfacial strain transfer.

Future directions of this work would emphasize on the synthesis and characterizations of the 1D-1D multiferroic composites. In particular, comparing the effect of magnetic core and magnetic shell in controlling converse ME coupling would provide a more impactful analysis of how nanostructuring could manipulate interfacial strain transfer. On the other hand, it is necessary to understand the fundamental mechanism of the enhanced magnetic moments observed in CFO nanostructures. By studying the strain states of the core-shell structures, it would provide insights of how intrinsic strain could enhance saturation magnetizations; whereas a detailed analysis of Co^{2+} occupancies in tetrahedral and octahedral sites of the inverse spinel structure through X-ray absorption studies and structural simulations could further quantify a possible spin canting, modifications on spin cancelling, or strain-induced transition of ferrimagnetism to ferromagnetism of CFO.

Bibliography

Akhter, M. A., D. J. Mapps and Y. Q. Ma Tan (1997). "Thickness and Grain-Size Dependence of the Coercivity in Permalloy Thin Films." journal of Applied Physics **81**(8): 4122.

Alford, T. L., L. C. Feldman and J. W. Mayer (2007). Fundamentals of nanoscale film analysis. New York, N.Y., Springer.

Amiri, P. K. and K. L. Wang (2012). "Voltage-Controlled Magnetic Anisotropy in Spintronic Devices." Spin **2**: 1240002.

Amiri, P. K. and K. L. Wang (2012). "Voltage-Controlled Magnetic Anisotropy in Spintronic Devices." Spin **02**(03): 1240002.

Anderson, J. A. and J. L. G. Fierro (1994). "Bulk and Surface Properties of Copper-Containing Oxides of the General Formula LaZr1-xCuxO3." Journal of Solid State Chemistry **108**(2): 305-313.

Ascher, E., H. Rieder, H. Schmid and H. Stossel (1966). "Some Properties of Ferromagnetoelectric Nickel-Iodine Boracite Ni3b7o13i." Journal of Applied Physics **37**(3): 1404-&.

Bibes, M. and A. Barthelemy (2008). "Multiferroics: towards a magnetoelectric memory." Nature Materials **7**: 425-426.

Bichurin, M. I., V. M. Petrov and G. Srinivasan (2003). "Theory of low-frequency magnetoelectric coupling in magnetostrictive-piezoelectric bilayers." Physical Review B **68**(5).

Biesinger, M. C., B. P. Payne, A. P. Grosvenor, L. W. M. Lau, A. R. Gerson and R. S. Smart (2011). "Resolving Surface Chemical States in XPS Analysis of First Row Transition Metals Oxides and Hydroxides: Cr, Mn, Fe, Co, and Ni." Applied Surface Science **257**: 2717-2730.

Bozorth, R. M., E. F. Tilden and A. J. Williams (1955). "Anisotropy and Magnetostriction of Some Ferrites." Physical Review **99**(6): 1788-1798.

Brinker, C. J., Y. F. Lu, A. Sellinger and H. Y. Fan (1999). "Evaporation-induced self-assembly: Nanostructures made easy." Advanced Materials **11**(7): 579-+.

Brooks, K. G., I. M. Reaney, R. Klissurska, Y. Huang, L. Bursill and N. Setter (1994). "Orientation of Rapid Thermally Annealed Lead Zirconate Titanate Thin Films on (111) Pt Substrates." Journal of Materials Research **9**(10): 2540-2553.

Cardarelli, F. (2008). Materials handbook a concise desktop reference. London, Springer,**:** xxxv, 1340 p.

Catalan, G. and J. F. Scott (2009). "Physics and Applications of Bismuth Ferrite." Advanced Materials **21**(24): 2463-2485.

Chien, D. (2016). "Engineering Nanoscale Multiferroic Composites for Memory Applications with Atomic Layer Deposition of Pb(Zrx,Ti1-x)O3 Thin Films." Doctoral Thesis.

Chien, D., A. N. Buditama, L. T. Schelhas, H. Y. Kang, S. Robbennolt, J. P. Chang and S. H. Tolbert (2016). "Tuning Magnetoelectric Coupling Using Porosity in Multiferroic Nanocomposites of ALD-grown Pb(Zr,Ti)O3 and Templated Mesoporous CoFe2O4." Applied Physics Letters **109**(11): 112904.

Choi, J. H., F. Zhang, Y. C. Perng and J. P. Chang (2013). "Tailoring the Composition of Lead Zirconate Titante by Atomic Layer Deposition." Journal of Vacuum Science & Technology B, Nanotechnology and Microelectronics: Materials, Processing, Measurement, and Phenomena **31**: 012207.

Cibert, C., J. Zhu, G. Poullain, R. Bouregba, J. More-Chevalier and A. Pautrat (2013). "Magnetoelectric coupling in Tb0.3Dy0.7Fe2/Pt/PbZr0.56Ti0.44O3 thin films deposited on Pt/TiO2/SiO2/Si substrate." Applied Physics Letters **102**(2).

Cohen, R. E. (1992). "Origin of Ferroelectricity in Perovskite Oxides." Nature **358**(6382): 136-138.

Cullity, B. D. and C. D. Graham (2005). Introduction to Magnetic Materials, John Wiley & Sons.

Dong, S. X., J. F. Li and D. Viehland (2004). "Characterization of magnetoelectric laminate composites operated in longitudinal-transverse and transverse-transverse modes." Journal of Applied Physics **95**(5): 2625-2630.

Eerenstein, W., N. D. Mathur and J. F. Scott (2006). "Multiferroic and magnetoelectric materials." Nature **442**(7104): 759-765.

Eerenstein, W., M. Wiora, J. L. Prieto, J. F. Scott and N. D. Mathur (2007). "Giant Sharp and Persistent Converse Magnetoelectric Effects in Multiferroic Epitaxial Heterostructures." Nature Materials **6**: 348-351.

Fritsch, D. and C. Ederer (2012). "First-principles calculation of magnetoelastic coefficients and magnetostriction in the spinel ferrites CoFe2O4 and NiFe2O4." Physical Review B **86**(1).

Gepras, S., A. Brandlmaier, M. Opel, R. Gross and S. T. B. Goennenwein (2010). "Electric Field Controlled Manipulation of the Magnetization in Ni/BaTiO3 Hybrid Structures." Applied Physics Letters **96**: 142509.

Giri, A. K., E. M. Kirkpatrick, P. Moongkhamklang, S. A. Majetich and V. G. Harris (2002). "Photomagnetism and Structure in Cobalt Ferrite Nanoparticles." Applied Physics Letters **80**(13): 2341-2343.

Gong, W., H. Li, Z. G. Zhao and J. C. Chen (1991). "Ultrafine Particles of Fe, Co, and Ni Ferromagnetic Metals." Journal of Applied Physics **69**(8): 5119-5121.

Gopalan, V., T. E. Mitchell, Y. Furukawa and K. Kitamura (1998). "The role of nonstoichiometry in 180 degrees domain switching of LiNbO3 crystals." Applied Physics Letters **72**(16): 1981-1983.

Gul, I. H. and A. Maqsood (2008). "Structural, Magnetic and Electrical Properties of Cobalt Ferrites Prepared by the Sol-Gel Route." Journal of Alloys and Compounds **465**(1-2): 227-231.

Hall, R. C. (1959). "Single Crystal Anisotropy and Magnetostriction Constants of Several Ferromagnetic Materials Including Alloys of Nife, Sife, Alfe, Coni, and Cofe." Journal of Applied Physics **30**(6): 816-819.

Haukka, S., E. L. Lakomaa, O. Jylha, J. Vilhunen and S. Hornytzkyj (1993). "Dispersion and Distribution of Titanium Species Bound to Silica from TiCl4." Langmuir **9**: 3497-3506.

Heron, J. T., J. L. Bosse, Q. He, Y. Gao, M. Trassin, L. Ye, J. D. Clarkson, C. Wang, J. Liu, S. Salahuddin, D. C. Ralph, D. G. Schlom, J. Iniguez, B. D. Huey and R. Ramesh (2014). "Deterministic Switching of Ferromagnetism at Room Temperature Using An Electric Field." Nature **516**: 370-373.

Ho, J. C., K. S. Liu and I. N. Lin (1993). "Study of Ferroelectricity in the Pmn Pt System near the Morphotropic Phase-Boundary." Journal of Materials Science **28**(16): 4497-4502.

Horiuchi, S. and T. Yoshinori (2008). "Organic Ferroelectrics." Nature Materials **7**: 357-366.

Hubert, A. and R. Schäfer (1998). Magnetic Domains: The Analysis of Magnetic Microstructures, Springer.

Kim, D. H., N. M. Aimon and C. A. Ross (2014). "Pillar Shape Modulation in Epitaxial BiFeO3-CoFe2O4 Vertical Nanocomposite Films." Applied Materials **2**: 081101.

Kim, Y., C. Pham and J. P. Chang (2015). "Potentials and Challenges of Integration for Complex Metal Oxides in CMOS Devices and Beyond." Journal of Physics D: Applied Physics **48**(6): 063001.

Kingon, A. I. and S. Srinivasan (2005). "Lead zirconate titanate thin films directly on copper electrodes for ferroelectric, dielectric and piezoelectric applications." Nature Materials **4**(3): 233-237.

Kryder, M. H. and C. S. Kim (2009). "After Hard Drives - What Comes Next?" IEEE Transactions on Mangetics **45**(10): 3406-3413.

Lebedev, G. A., B. Viala, T. Lafont, D. I. Zakharov, O. Cugat and J. Delamare (2012). "Converse magnetoelectric effect dependence with CoFeB composition in ferromagnetic/piezoelectric composites." Journal of Applied Physics **111**(7).

Liu, B. H. and J. Ding (2006). "Strain-Induced High Coercivity in CoFe2O4 Powders." Applied Physics Letters **88**: 042506.

Liu, M., O. Boi, J. Lou, Y. Chen, Z. Cai, S. Stoute, M. Espanol, M. Lew, X. Situ, K. S. Ziemer, V. G. Harris and N. X. Sun (2009). "Giant Electric Field Tuning of Magnetic Properties in Multiferroic Ferrite / Ferroelectric Heterostructures." Advanced Functional Materials **19**(11): 1826-1831.

Lou, J., D. Reed, M. Liu, C. Pettiford and N. X. Sun (2009). "Novel Electrostatically Tunable FeGaB/(Si)/PMN-PT Multiferroic Heterostructures for Microwave Application." 2009 Ieee/Mtt-S International Microwave Symposium, Vols 1-3: 33-36.

Lueken, H. (2012). Superconducting Quantum Interference Device Magnetometry. Methods in Physical Chemistry, Wiley-VCH Verlag GmbH & Co. KGaA**:** 763-795.

Ma, W. H. and L. E. Cross (2003). "Strain-gradient-induced electric polarization in lead zirconate titanate ceramics." Applied Physics Letters **82**(19): 3293-3295.

McClean, B. (2017). The McClean Report 2017, IC Insights, Inc.

Nan, C. W., G. Liu, Y. H. Lin and H. D. Chen (2005). "Magnetic-field-induced electric polarization in multiferroic nanostructures." Physical Review Letters **94**(19).

Nechache, R., P. Gupta, C. Harnagea and A. Pignolet (2007). "Enhanced magnetism in epitaxial BiFeO(3)/BiCrO(3) multiferroic heterostructures." Applied Physics Letters **91**(22).

Nie, J. W., G. Y. Xu, Y. Yang and C. W. Cheng (2009). "Strong magnetoelectric coupling in CoFe2O4-BaTiO3 composites prepared by molten-salt synthesis method." Materials Chemistry and Physics **115**(1): 400-403.

Park, S. E. and T. R. Shrout (1997). "Ultrahigh strain and piezoelectric behavior in relaxor based ferroelectric single crystals." Journal of Applied Physics **82**(4): 1804-1811.

Peng, J. H., M. Hojamberdiev, H. Q. Li, D. L. Mao, Y. J. Zhao, P. Liu, J. P. Zhou and G. Q. Zhu (2015). "Electrical, Magnetic, and Direct and Converse Magnetoelectric Properties of

(1−x)Pb(Zr0.52Ti0.48)O3−(x)CoFe2O4 (PZT–CFO) Magnetoelectric Composites." Journal of Magnetism and Magnetic Materials **378**: 298-305.

Petrov, V. M., G. Srinivasan, M. I. Bichurin and A. Gupta (2007). "Theory of magnetoelectric effects in ferrite piezoelectric nanocomposites." Physical Review B **75**(22).

Pham, C. (2015). "Atomic Layer Deposition Enabled Synthesis of Multiferroic Nanostructures." Doctoral Thesis.

Pham, C. D., J. Chang, M. A. Zurbuchen and J. P. Chang (2017). "Magnetic Properties of CoFe2O4 Thin Films Synthesized by Radical Enhanced Atomic Layer Deposition." In preparation.

Pintilie, L., C. Ghica, C. M. Teodorescu, I. Pintilie, C. Chirila, I. Pasuk, L. Trupina, L. Hrib, A. G. Boni, N. G. Apostol, L. E. Abramiuc, R. Negrea, M. Stefan and D. Ghica (2015). "Polarization Iduced Self-Doping in Epitaxial Pb(Zr0.20Ti0.80)O3 Thin Films." Scientific Reports **5**: 14974.

Powell, C. J. (2012). "Recommended Auger Parameters for 42 Elemental Solids." Journal of Electron Spectroscopy and Related Phenomena **185**(1-2): 1-3.

Pulskamp, J. S., R. G. Polcawich, R. Q. Rudy, S. S. Bedair, R. M. Proie, T. Ivanov and G. L. Smith (2012). "Piezoelectric PZT MEMS technologies for small-scale robotics and RF applications." MRS Bulletin **37**(11): 1062-1070.

Rado, G. T., J. M. Ferrari and W. G. Maisch (1984). "Magnetoelectric Susceptibility and Magnetic Symmetry of Magnetoelectrically Annealed Tbpo4." Physical Review B **29**(7): 4041-4048.

Raman, N. K., M. T. Anderson and C. J. Brinker (1996). "Template-based approaches to the preparation of amorphous, nanoporous silicas." Chemistry of Materials **8**(8): 1682-1701.

Reitz, C., P. M. Leufke, H. Hahn and T. Brezesinski (2014). "Ordered Mesoporous Thin Film Ferroelectrics of Biaxially Textured Lead Zirconate Titanate (PZT) by Chemical Solution Deposition." Chemistry of Materials **26**(6): 2195-2202.

Ren, S., R. M. Briber and M. Wuttig (2008). "Diblock Copolymer Based Self-Assembled Nanomagnetoelectric." Applied Physics Letters **93**: 173507.

Ren, S. Q., M. Laver and M. Wuttig (2009). "Nanolamellar magnetoelectric BaTiO3-CoFe2O4 bicrystal." Applied Physics Letters **95**(15).

Roy, S., R. Chatterjee and S. B. Majumder (2011). "Magnetoelectric coupling in sol-gel synthesized dilute magnetostrictive-piezoelectric composite thin films." Journal of Applied Physics **110**(3).

Samuelson, L. (2003). "Self-forming nanoscale devices." Materials Today **6**(10): 22-31.

Sandlund, L., M. Fahlander, T. Cedell, A. E. Clark, J. B. Restorff and M. Wunfogle (1994). "Magnetostriction, Elastic-Moduli, and Coupling Factors of Composite Terfenol-D." Journal of Applied Physics **75**(10): 5656-5658.

Shrout, T. R. and S. J. Zhang (2007). "Lead-free Piezoelectric Ceramics: Alternatives for PZT?" Journal of Electroceramics **19**(1): 113-126.

Siegbahn, K., C. Nordling, A. Fahlman, R. Nordberg, K. Hamrin, F. Hedman, G. Johansson, T. Bergmark, S. E. Karlsson, I. Lindgren and B. Lindberg (1967). ESCA: Atomic, Molecular and Solid State Structure Studied by Means of Electron Spectroscopy.

Siemensmeyer, B., K. Bade and J. W. Schultze (1991). "XPS and Electrochemical Studies of Thin TiN Layers." Berichte der Bunsengesellschaft für physikalische Chemie **95**(11): 1461-1469.

Sim, C. H., A. Z. Z. Pan and J. Wang (2008). "Thickness and coupling effects in bilayered multiferroic CoFe(2)O(4)/Pb(Zr(0.52)Ti(0.48))O(3) thin films." Journal of Applied Physics **103**(12).

Song, C., B. Cui, F. Li, X. Zhou and F. Pan (2017). "Recent Progress in Voltage Control of Magnetism: Materials, Mechanisms, and Performance." Progress in Materials Science **87**: 33-82.

Srinivasan, G., E. T. Rasmussen, A. A. Bush, K. E. Kamentsev, V. F. Meshcheryakov and Y. K. Fetisov (2004). "Structural and magnetoelectric properties of MFe2O4-PZT (M = Ni, Co) and La-x(Ca, Sr)(1-x)MnO3-PZT multilayer composites." Applied Physics a-Materials Science & Processing **78**(5): 721-728.

Srinivasan, G., E. T. Rasmussen, J. Gallegos, R. Srinivasan, Y. I. Bokhan and V. M. Laletin (2001). "Magnetoelectric bilayer and multilayer structures of magnetostrictive and piezoelectric oxides." Physical Review B **64**(21).

Srinivasan, G., E. T. Rasmussen and R. Hayes (2003). "Magnetoelectric effects in ferrite-lead zirconate titanate layered composites: The influence of zinc substitution in ferrites." Physical Review B **67**(1).

Srinivasan, G., E. T. Rasmussen, B. J. Levin and R. Hayes (2002). "Magnetoelectric effects in bilayers and multilayers of magnetostrictive and piezoelectric perovskite oxides." Physical Review B **65**(13).

Takenaka, T., H. Nagata and Y. Hiruma (2009). "Phase Transition Temperatures and Piezoelectric Properties of (Bi1/2Na1/2)TiO3- and (Bi1/2K1/2)TiO3-Based Bismuth Perovskite Lead-Free Ferroelectric Ceramics." Ieee Transactions on Ultrasonics Ferroelectrics and Frequency Control **56**(8): 1595-1612.

Tang, Z. H., M. H. Tang, X. S. Lv, H. Q. Cai, Y. G. Xiao, C. P. Cheng, Y. C. Zhou and J. He (2013). "Enhanced magnetoelectric effect in La0.67Sr0.33MnO3/PbZr0.52Ti0.48O3 multiferroic nanocomposite films with a SrRuO3 buffer layer." Journal of Applied Physics **113**(16).

Thiele, C., K. Dorr, O. Bilani, J. Rodel and L. Schultz (2007). "Influence of Strain on the Mangetization and Magnetoelectric Effect in La0.7A0.3MnO3/PN-PT(001) (A = Sr, Ca)." Physical Review B **75**: 054408.

Tipler, P. A. (1999). Physics for Scientists and Engineers, Worth Publishers.

Tokunaga, Y., S. Iguchi, T. Arima and Y. Tokura (2008). "Magnetic-Field-Induced Ferroelectric State in DyFeO3." Physical Review Letters **101**(9).

Udayakumar, K. R., P. J. Schuele, J. Chen, S. B. Krupanidhi and L. E. Cross (1995). "Thickness-Dependent Electrical Characteristics of Lead Zirconate Titanate Thin Films." journal of Applied Physics **77**(8): 3981.

Vandenboomgaard, J., A. M. J. G. Vanrun and J. Vansuchtelen (1976). "Magnetoelectricity in Piezoelectric-Magnetostrictive Composites." Ferroelectrics **10**(1-4): 295-298.

Vickerman, J. C. and I. S. Gilmore (2009). Surface analysis : the principal techniques. Chichester, U.K., Wiley.

Wagner, C. D., E. E. Passoja, H. F. Hillery, T. G. Kinisky, H. A. Six, W. T. Jansen and J. A. Taylor (1982). "Auger and Photoelectron Line Energy Relationships in Aluminum-Oxygen and Silicon-Oxygen Compounds." Journal of Vacuum Science & Technology **21**: 933.

Wan, J. G., X. W. Wang, Y. J. Wu, M. Zeng, Y. Wang, H. Jiang, W. Q. Zhou, G. H. Wang and J. M. Liu (2005). "Magnetoelectric CoFe2O4-Pb(Zr,Ti)O-3 composite thin films derived by a sol-gel process." Applied Physics Letters **86**(12).

Wan, J. G., Y. Y. Weng, Y. J. Wu, Z. Y. Li, J. M. M. Liu and G. H. Wang (2007). "Controllable phase connectivity and magnetoelectric coupling behavior in CoFe2O4-Pb(Zr, Ti)O-3 nanostructured films." Nanotechnology **18**(46).

Wang, D. X., C. Nordman, Z. H. Qian, J. M. Daughton and J. Myers (2005). "Magnetostriction effect of amorphous CoFeB thin films and application in spin-dependent tunnel junctions." Journal of Applied Physics **97**(10).

Wang, K. L., J. G. Alzate and P. K. Amiri (2013). "Low-Power Non-Voatile Spintronic Memory: STT-RAM and Beyond." Journal of Physics D: Applied Physics **46**(7): 074003.

Wang, Y., J. M. Hu, Y. H. Lin and C. W. Nan (2010). "Multiferroic magnetoelectric composite nanostructures." Npg Asia Materials **2**(2): 61-68.

Wang, Y. C., J. Ding, J. B. Yi, B. H. Liu, T. Yu and Z. X. Shen (2004). "High-Coercivity Co-Ferrite Thin Films on (100)-SiO2 Substrate." Applied Physics Letters **84**(14): 2596.

Wu, J. G. and Y. M. Wang (2014). "Two-step sintering of new potassium sodium niobate ceramics: a high d(33) and wide sintering temperature range." Dalton Transactions **43**(34): 12836-12841.

Xu, Y. D., G. A. Wu, H. L. Su, M. Shi, G. Y. Yu and L. Wang (2011). "Magnetoelectric CoFe2O4/Pb(Zr0.53Ti0.47)O-3 composite thin films of 2-2 type structure derived by a sol-gel process." Journal of Alloys and Compounds **509**(9): 3811-3816.

Yang, J. J., Y. G. Zhao, H. F. Tian, L. B. Luo, H. T. Zhang, Y. J. He and H. S. Luo (2009). "Electric Field Manipulation of Magnetic at Room Temperature in Multiferroic CoFe2O4/Pb(Mg1/3Nb2/3)0.7Ti0.3O3 Heterostructures." Applied Physics Letters **94**: 212504.

Yang, S. Y., L. W. Martin, S. J. Byrnes, T. E. Conry, S. R. Basu, D. Paran, L. Reichertz, J. Ihlefeld, C. Adamo, A. Melville, Y. H. Chu, C. H. Yang, J. L. Musfeldt, D. G. Schlom, J. W. Ager and R. Ramesh (2009). "Photovoltaic effects in BiFeO3." Applied Physics Letters **95**(6).

Zaliznyak, A. (2007). Spin Structures and Spin Wave Excitations: Handbook of Magnetism and Advanced Magnetic Materials. Hoboken, NJ, John Wiley & Sons.

Zavaliche, F., H. Zheng, L. Mohaddes-Ardabili, S. Y. Yang, Q. Zhang, P. Shafer, E. Reilly, R. Chopdekar, Y. Jia, P. Wright, D. G. Schlom, Y. Suzuki and R. Ramesh (2005). "Electric Field-Induced Magnetization Switching in Epitaxial Columnar Nanostructures." Nano Letters **5**(9): 1793-1796.

Zhai, J. Y., N. Cai, L. Liu, Y. H. Lin and C. W. Nan (2003). "Dielectric behavior and magnetoelectric properties of lead zirconate titanate/Co-ferrite particulate composites." Materials Science and Engineering B-Solid State Materials for Advanced Technology **99**(1-3): 329-331.

Zhang, F., Y. C. Perng, J. H. Choi, T. Wu, T. K. Chung, G. P. Carman, C. Locke, S. Thomas, S. E. Saddow and J. P. Chang (2011). "Atomic Layer Deposition of Pb(Zr,Ti)Ox on 4H-SiC for Metal-Ferroelectric-Insulator-Semiconductor Diodes." journal of Applied Physics **109**: 124109.

Zhang, S. J., J. B. Lim, H. J. Lee and T. R. Shrout (2009). "Characterization of Hard Piezoelectric Lead-Free Ceramics." Ieee Transactions on Ultrasonics Ferroelectrics and Frequency Control **56**(8): 1523-1527.

Zhang, S. J., R. Xia, T. R. Shrout, G. Z. Zang and J. F. Wang (2006). "Piezoelectric properties in perovskite 0.948(K0.5Na0.5)NbO3-0.052LiSbO(3) lead-free ceramics." Journal of Applied Physics **100**(10).

Zhang, X. D., X. J. Meng, J. L. Sun, T. Lin and J. H. Chu (2005). "Low-temperature preparation of highly (100)-oriented Pb(ZrxTi1-x)O-3 thin film by high oxygen-pressure processing." Applied Physics Letters **86**(25).

Zhang, Y., C. Y. Deng, J. Ma, Y. H. Lin and C. W. Nan (2008). "Enhancement in magnetoelectric response in CoFe2O4-BaTiO3 heterostructure." Applied Physics Letters **92**(6).

Zhao, D., Y. Wan and W. Zhou (2013). Ordered mesoporous materials. Weinheim, Wiley-VCH,**:** 1 online resource (xvii, 522 p.

Zhao, T., A. Scholl, F. Zavaliche, K. Lee, M. Barry, A. Doran, M. P. Cruz, Y. H. Chu, C. Ederer, N. A. Spaldin, R. R. Das, D. M. Kim, S. H. Baek, C. B. Eom and R. Ramesh (2006). "Electrical Control of Antiferromagnetic Domains in Multiferroic BiFeO3 Films at Room Temperature." nature Materials **5**: 823-829.

Zheng, H., J. Wang, S. E. Lofland, Z. Ma, L. Mohaddes-Ardabili, T. Zhao, L. Salamanca-Riba, S. R. Shinde, S. B. Ogale, F. Bai, D. Viehland, Y. Jia, D. G. Schlom, M. Wuttig, A. Roytburd and R. Ramesh (2004). "Multiferroic BaTiO3-CoFe2O4 nanostructures." Science **303**(5658): 661-663.

Zheng, H., J. Wang, L. Mohaddes-Ardabili, M. Wuttig, L. Salamanca-Riba, D. G. Schlom and R. Ramesh (2004). "Three-dimensional heteroepitaxy in self-assembled BaTiO3-CoFe2O4 nanostructures." Applied Physics Letters **85**(11): 2035-2037.

Zheng, T., J. G. Wu, X. J. Cheng, X. P. Wang, B. Y. Zhang, D. Q. Xiao, J. G. Zhu, X. J. Loub and X. J. Wang (2014). "New potassium-sodium niobate material system: a giant-d(33) and high-T-c lead-free piezoelectric." Dalton Transactions **43**(30): 11759-11766.

Zhong, X. L., J. B. Wang, M. Liao, G. J. Huang, S. H. Xie, Y. C. Zhou, Y. Qiao and J. P. He (2007). "Multiferroic nanoparticulate Bi3.15Nd0.85Ti3O12-CoFe2O4 composite thin films prepared by a chemical solution deposition technique." Applied Physics Letters **90**(15).

Zhu, W. M., L. W. Su, Z. G. Ye and W. Ren (2009). "Enhanced magnetization and polarization in chemically modified multiferroic (1-x)BiFeO3-xDyFeO(3) solid solution." Applied Physics Letters **94**(14).

Zou, G. F., K. Xiong, C. L. Jiang, H. Li, Y. Wang, S. Y. Zhang and Y. T. Qian (2005). "Magnetic Fe3O4 nanodisc synthesis on a large scale via a surfactant-assisted process." Nanotechnology **16**(9): 1584-1588.

APPENDIX A. Multiferroic

A.1 Ferromagnetism (Detailed)

In order to discuss ferromagnetism, the origin of magnetization should first be elaborated. When a magnetic field, $H = H_0 e^{i\omega t}$ [A/m], is applied through a material, a magnetic flux density appears, $B = B_0 e^{i\omega t}$ [T], namely magnetic induction. Their relationship can be described by the general equation,

$$\mathbf{B} = \mu \mathbf{H} = \mu_0 \mu_r \mathbf{H} \tag{A.1}$$

where the induction is collinear and directly proportional to the applied field. The proportionality is described by the magnetic permeability of the medium μ [H/m]. The permeability can also be expressed by permeability of free space, d_0, and relative permeability, μ_r, at which $\mu = \mu_0 \mu_r$. For magnetic material with magnetic losses, the permeability can be expressed by a real (μ') and imaginary part (μ"), both of which are functions of frequency of the applied magnetic field. At low frequencies, the induced magnetic flux is proportional to the applied field as mentioned above in linear-response materials. With increased frequency, the induced flux exhibit delays in response with a phase lag $i\delta$ such that $B = B_0 e^{i(\omega t-\delta)}$ due to the resonance of magnetic moments. Since permeability is the ratio between the induced flux and applied field, that is,

$$\mu = \frac{\mathbf{B}}{\mathbf{H}} = \frac{B_0 e^{i(\omega t-\delta)}}{H_0 e^{i\omega t}} = \frac{B_0}{H_0} e^{-i\delta} = \frac{B_0}{H_0}(\cos\delta - i\sin\delta) = \mu' - i\mu'' \tag{A.2}$$

which, in general, h' describes the resonance and absorption of the applied field, while μ'' describes losses of the response. A convenient quantity, loss tangent, is defined to indicate the energy loss upon applied magnetic field, $\tan\delta_m = \mu' / \mu''$.

The magnetic properties of materials are originated from spin and orbital magnetic moment of unpaired electrons. Collection of magnetic moments in the same direction forms regions called magnetic domains that can be aligned with an applied field direction with a torque,

$$\tau = \mathbf{m} \times \mathbf{B} \tag{A.3}$$

with the unit of N-m. Neighboring magnetic domains have opposing orientations in order to minimize magnetostatic energy of the system. Microscopic magnetic dipole moments give rise to a macroscopic vector quantity, magnetization density M. As to quantify the amount of material being magnetized upon applied magnetic field H, magnetic susceptibility (χ_m) is introduced, that is,

$$\mathbf{M} = \chi_m \mathbf{H} \tag{A.4}$$

Magnetic materials are divided into groups based on their susceptibilities. Materials that can be highly magnetized i.e. $\chi_m > 1$ are known as ferromagnets with their domains aligning to the applied field; weakly-magnetized materials ($10^{-3} < \chi_m < 10^{-5}$) are, on the other hand, paramagnets. Materials possessing negative susceptibility are referred to as diamagnets, which are able to create an opposing field to the applied field. Susceptibility of negative unity are perfect superconductors, expelling any magnetic flux into the material by creating a spontaneous electric current on the surface, and thus used for superconducting.

As a result, for a material under a magnetic field, the total magnetic induction from both the applied field and spontaneous dipole alignments is expressed as follows,

$$\mathbf{B} = \mu_0 \mathbf{H} + \mu_0 \mathbf{M} = \mu_0 \left(1 + \chi_m\right) \mathbf{H} \tag{A.5}$$

where the equation is applicable to isotropic materials. Susceptibility becomes a tensor when the material is anisotropic. It should be noted that the permeability is related to the susceptibility by

$\mu_r = 1 + \chi_m$. Therefore, the susceptibility should also be a function of frequency of the applied field(Cardarelli 2008).

The origin of magnetism is described by quantum mechanics, in which orbital angular momentum and spin angular momentum should be discussed, and their contributions in magnetic dipoles and thus, magnetizations.

Schrödinger Equation (SE) derives the discrete energy levels of electrons and quantum confinement effects as illustrated in many quantum mechanics textbooks. The description of the complete quantum state of an electron is essential, which consists of four quantum numbers: principle (*n*), azimuthal (*l*), magnetic (*ml*) and spin (*ms*) quantum numbers. Electrons cannot have identical quantum state in one system based on Pauli exclusion principle.

When the Schrödinger Equation is expressed in spherical coordinates for the analysis of hydrogen atom, with the corresponding spherical symmetric potentials, it can be solved by separation of variables such that the wavefunction is a multiple of individual functions, i.e., $\Psi(r,hen) = R(r)\Theta(\theta)\Phi(\varphi)$.After rearranging variables, the Schrödinger Equation is given by,

$$\frac{1}{R}\frac{d}{dr}\left[r^2\frac{dR}{dr}\right]+\frac{2\mu}{\hbar^2}\left(Er^2+ke^2r\right)+\frac{1}{\sin^2\theta}\left[\frac{\sin\theta}{\Theta}\frac{d}{d\theta}\left(\sin\theta\frac{d\Theta}{d\theta}\right)+\frac{1}{\Phi}\frac{d^2\Phi}{d\phi^2}\right]=0 \qquad \text{(A.6)}$$

in which the first part is the radial equation with variable r, and the second part is the colatitude and azimuthal equation containing angular variables θ and φ. Both parts should be real for all values or r, θ and φ, if and only if each part equals to a constant, C_r. Similarly, the two terms in the angular part must equal to another constant C_φ. This characteristic is then used to solve for eigenvalues of the Schrödinger Equation.

The azimuthal quantum number, l, also known as orbital quantum number, describes the magnitude of orbital angular momentum, $|L|$, by

$$|\mathbf{L}| = \sqrt{l(l+1)}\hbar \qquad 0 \le l < n \tag{A.7}$$

as the result of the constraints in colatitude equation that $C_r = l(l+1)$ and comparing coefficients in the series expansion of the colatitude equation. It also describes the sub-shell levels (*s*, *p*, *d*, *f*) within the principle level limited by the principal quantum number *n*. The number of electrons states in one sub-shell is $2(2l+1)$, which is explained by magnetic and spin quantum numbers for allowable states.

The magnetic quantum number, m_l, describes the orientations of the orbital angular momentum with a projected magnitude of L onto the magnetization direction *z*,

$$L_z = m_l\hbar \qquad -l \le m_l \le l \tag{A.8}$$

The quantized values of ml from the solutions of azimuthal equation ($C_\varphi = -m_l^2$) through angular periodicity of 2π lead to discrete orientations of L. Electrons with the same orbital angular momentum have equal energy with the absence of magnetic field. However, under magnetic field, the magnetic quantum number describes the energy level splitting with integral values from –*l* to +*l*.

Both orbital and magnetic quantum number are commonly described in a vector model, as shown in Figure A.1, in which the angular momentum vector precesses about a specific direction z, usually the direction of the applied magnetic field, i.e. the magnetization direction. The magnitude |L| and the projection of orbital angular momentum along the field direction L_z are given by the above equations. The limited values of ml imply the orientation is quantized, and never collinear with the field direction. The precession of the angular momentum is analogous to the precession of magnetic moment caused by the magnetic field-induced torque, namely the Larmor precession, described by Equation (A.3). When the torque is produced in the direction perpendicular to the orbital angular momentum, the angular momentum changes with an increment ΔL, and allows it to precess.

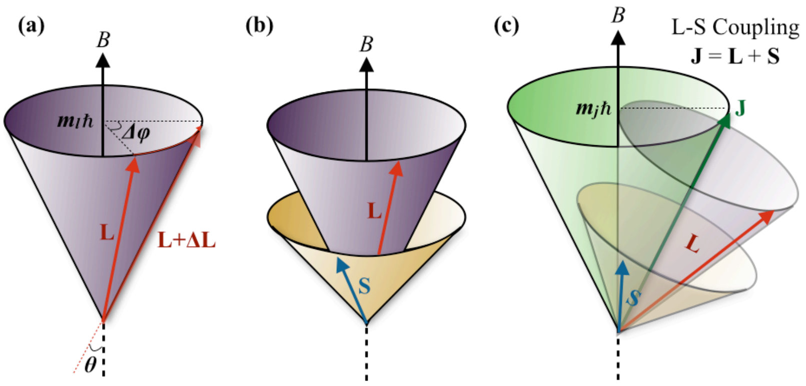

Figure A.1 Precession of (a) orbital angular momentum L, (b) spin angular momentum S, and (c) total angular momentum through L-S coupling

Zeeman effect is the first illustration of energy level splitting through the splitting of spectral lines under magnetic field. From classical mechanics, the current equals to number of charges divided by distance travelled. Therefore,

$$\mathbf{m}_{orb} = IA = \left(\frac{-ev}{2\pi r}\right)\left(\pi r^2\right) = -\frac{evr}{2} = -\frac{e}{2m_e}\mathbf{L} \tag{A.9}$$

By substituting the angular momentum in the z-direction,

$$\mathbf{m}_{orb,z} = -\frac{e}{2m_e}\left(m_l\hbar\right) = -\mu_B m_l \tag{A.10}$$

where μ_B is the Bohr magneton, representing the elementary unit of orbital magnetic moment in a single-electron atom. Upon the presence of magnetic field, the energy levels associated are,

$$E_{orb} = -\mu_0 \mathbf{m}_{orb} \cdot \mathbf{B} = \mu_0 \mathbf{m}_{orb,z} B = \mu_0 \mu_B m_l B \tag{A.11}$$

which is a function of the applied magnetic field with an energy splitting based on values of the magnetic quantum number. Since the orbital magnetic moment is quantized, the resulting energy level splitting is also quantized.

The spin quantum number, s, describes the spin of an electron within a certain orbital. The magnitude of spin angular momentum is analogous to orbital angular momentum, given by,

$$|\mathbf{S}| = \sqrt{s(s+1)}\hbar \tag{A.12}$$

with the value equal to ±½ for electrons. Fundamental particles like fermions have half-integral values of spins, whereas bosons have integral values. Similarly, the spin quantum number has its own counterpart m_s, analogous to magnetic quantum number ml, which describes the projected magnitude of the spin angular momentum,

$$S_z = m_s\hbar \qquad -s \le m_s \le s \tag{A.13}$$

with values of half integers. The spin magnetic moment is derived analogously,

$$\mathbf{m}_{spin} = -g_e \frac{e}{2m_e}\mathbf{S} \qquad \mathbf{m}_{spin,z} = -g_e \mu_B m_s \tag{A.14}$$

where g_e is the spin g-factor to account for the correction from quantum electrodynamic theory. The precise value of g-factor was predicted in Dirac equation of approximately 2. Upon the presence of magnetic field, the energy levels associated are,

$$E_{spin} = -\mu_0 \mathbf{m}_{spin} \cdot \mathbf{B} = g_e \mu_0 \mu_B m_s B \tag{A.15}$$

The concept of vector model can be extended to both orbital electrons and electron spins, especially in the case of spin-orbital coupling. Electron orbital precession, as mentioned above, the torque associated with the applied magnetic field can be expressed by infinitesimal change in orbital angular momentum with respect with time, that is, as shown in Figure A.1(a). The torque can also be calculated using Equation (A.3)

$$\tau_{orb} = \mathbf{m} \times \mathbf{B} = \frac{e}{2m_e}|\mathbf{L}| B \sin\theta \tag{A.16}$$

The precession angular velocity, ω_{orb}, namely Larmor frequency, can then be determined by rearranging terms of the above equation,

$$\omega_{orb} = \frac{d\varphi}{dt} = \frac{e|\mathbf{L}|B\sin\theta / 2m_e}{|\mathbf{L}|\sin\theta} = \frac{e}{2m_e}B \tag{A.17}$$

Similarly for the case of electron spin precession, the Larmor frequency is,

$$\omega_{spin} = g_e \frac{e}{2m_e}B \tag{A.18}$$

The two types of magnetic moments, electron orbital and spin magnetic moment, have been discussed individually. However, both could interact with each other, that is, the magnetic moment from the electron spin is interfered by the magnetic moment from the electron's orbital motion, and vice versa, resulting in spin-orbital coupling.

Russell-Saunders Coupling, or L-S coupling, describes weak spin-orbital coupling in light atoms that spin-spin coupling and orbital-orbital coupling are more dominant. Orbital angular momentum L is the sum of individual orbital momentum of electrons L_1, L_2, …,L_n; and the spin angular momentum S is the sum of individual spin momentum S_1, S_2, …, S_n. Therefore, the total angular momentum J is given by,

$$\mathbf{J} = \mathbf{L} + \mathbf{S} \tag{A.19}$$

The allowed states would then be the sum of vector L and S. Also, filled shells have no contribution in magnetic dipoles. The magnitude of the total angular momentum is given by,

$$|\mathbf{J}| = \sqrt{j(j+1)}\hbar \tag{A.20}$$

with the corresponding projected magnitude as $J_z = m_j\hbar$. Under magnetic field, the total angular momentum precesses around the direction of applied field, as shown in Figure A.1(c).

As J is a vector sum of L and S, the energy splitting associated depends on coupling effect. For $g_e = 2$, implying spin angular moment is twice as effective in inducing magnetic moments, the energy splitting can be described as,

$$E_{L-S} = -\mu_0 \mathbf{m}_{L-S} \cdot \mathbf{B} = \mu_0 \frac{e}{2m_e} (\mathbf{L} + 2\mathbf{S}) \cdot \mathbf{B} \tag{A.21}$$

As L and S precess at changing radius from B, the dot product cannot be resolved easily. J is used as a reference axis thru dot products of unit vector of J,

$$E_{L-S} = \mu_0 \frac{e}{2m_e} \left[\frac{(\mathbf{L} + 2\mathbf{S}) \cdot \mathbf{J}}{|\mathbf{J}|} \frac{\mathbf{J} \cdot \mathbf{B}}{|\mathbf{J}|} \right] = \mu_0 \frac{e}{2m_e} \left[\frac{(\mathbf{L} + 2\mathbf{S})(\mathbf{L} + \mathbf{S})}{|\mathbf{J}|^2} J_z B \right] \tag{A.22}$$

With the use of trigonometry identities, the above equation can be reduced to the form,

$$E_{L-S} = \mu_0 \mu_B m_j B \left[1 + \frac{|\mathbf{J}|^2 - |\mathbf{L}|^2 + |\mathbf{S}|^2}{2|\mathbf{J}|^2} \right] = g_L \mu_0 \mu_B m_j B \tag{A.23}$$

where g_L is Landé *g*-factor that dictates the unequal energy splitting in anomalous Zeeman effect. Similar to spin angular momentum, the total magnetic moment is,

$$\mathbf{m}_{L-S} = -g_L \frac{e}{2m_e} \mathbf{J} \qquad \mathbf{m}_{L-S,z} = -g_L \mu_B m_j \tag{A.24}$$

With the special case when S = 0, the g-factor equals to 1 (J = L) and yields the same result as normal Zeeman effect in orbital angular momentum. Upon a strong magnetic field, the spin and orbital decoupled and precess individually, which is the result of coupling directly to the applied field, known as Paschen-Back effect.

Magnetic materials can be categorized into the following classes: Diamagnetic, paramagnetic, ferromagnetic and antiferromagnetic.

Materials are classified as *diamagnetic* when spontaneous opposing field is induced under an external magnetic field. The electron configuration of diamagnetic material is usually fully-filled that no permanent magnetic moment could contribute to magnetization. Some materials such as copper oxide possess perfect diamagnetism for superconductivity when quenched below a critical temperature. A strong opposing field could be induced spontaneously to exclude any magnetic flux from its surface, known as Meissner effect.

Most transitional metal salts are *paramagneti*c that magnetization increases proportionally to the applied magnetic field as suggested by Curie-Weiss Law. The net magnetic moment originates from the partially filled *d*-shell. With a weak coupling between neighboring spins through the mediation of anions in the crystal structure, the small magnetization is perfectly reversible to its random state when applied field is removed. *Ferromagnetic* materials have similar electronic structures but the coupling between spins is stronger compare with paramagnets. Magnetic states exhibit hysteresis characteristics under changing magnetic field. Ferromagnets become paramagnets when the temperature elevated beyond Curie temperature, T_c. Above the critical temperature, thermal energy outweighs the coupling of spins, and thus destroy the long-range FM ordering. The derivation can be explained as the following.

In classical mechanics, Langevin equation is used to describe randomly oriented magnetic moments due to their thermal energy, assuming individual magnetic moment do not interact with each other (i.e. paramagnets). The probability of occupying an energy state is solely based on Boltzmann statistics $P(E) = \exp(mH\cos\theta/k_BT)$, in which mechanics, Langevin equation is used to describe randomly oriented magnetic moments due to their thermal energy, assuming individual magnetic moment do not interact with each other (i.e. θ and $\theta+d\theta$ is calculated for the entire segment by,

$$P(\theta)=\frac{P(E)(2\pi r)r\sin\theta d\theta}{\int_0^\pi P(E)(2\pi r)r\sin\theta\, d\theta}=\frac{P(E)\sin\theta d\theta}{\int_0^\pi P(E)\sin\theta\, d\theta} \tag{A.25}$$

The total magnetization is then the sum of projections from N individual magnetic moment per unit volume along the applied magnetic field, with its expected value $m\cos\theta P(\theta)$,

$$\mathbf{M}=N\int_0^\pi \mathbf{m}\cos\theta P(\theta)d\theta=N\mathbf{m}\left(\coth\alpha-\frac{1}{\alpha}\right)=M_s\mathcal{L}(\alpha) \tag{A.26}$$

where L(α) is called the Langevin function with $\alpha = \mu_0 mH/k_BT$; and M_s is the saturation magnetization when all dipoles are aligned. The Langevin function can then be simplified through Taylor series expansion and result in,

$$\mathbf{M} = \frac{\mu_0 N|\mathbf{m}|^2}{3k_BT}\mathbf{H} \Rightarrow \chi = \frac{\mu_0 N|\mathbf{m}|^2}{3k_BT} = \frac{C}{T} \tag{A.27}$$

The above classical mechanics approach allows any orientation θ of the magnetic moment, which is not the case in quantum mechanic. With the quantization taken into account, the susceptibility becomes,

$$\chi = \frac{N\mu_0\left[g_L\mu_B\sqrt{J(J+1)}\right]^2}{3k_BT} = \frac{C'}{T} \tag{A.28}$$

where the inverse proportionality of temperature remains. The above result is known as Curie Law. However, many materials do not satisfy the above equation due to interactions between magnetic moments (i.e. Ferromagnets). Weiss proposed there exists a molecular field that mutual interactions between electrons tend to align neighboring magnetic moments in parallel, producing a magnetic field that increases with magnetization,

$$\mathbf{H}_w = \gamma\mathbf{M} \tag{A.29}$$

where γ is called molecular field constant. Therefore, the resultant magnetic field acting on the materials is the sum of the applied and the induced field. By replacing H by ($H+H_w$),

$$\chi = \frac{C}{T - C\gamma} = \frac{C}{T - T_C} \tag{A.30}$$

where T_C is the Curie temperature. Weiss' theory layout the fundamental concept of ferromagnetism that internal molecular field is sufficient for some materials to overcome thermal energy from randomizing magnetic moments below a critical temperature T_C after the applied magnetic field is removed. If the magnetization is assumed to be contributed solely from the molecular field such that $H = H_w$, the critical temperature at which magnetization becomes zero should equal to the result from Langevin function. The molecular field constant can then be represented through Curie temperature.

$$\gamma = \frac{3k_B T_C}{\mu_0 N |\mathbf{m}|^2} \tag{A.31}$$

where m can be substituted by $m_{\mathrm{eff}} = g{=}_{\mathrm{B}}[J(J+1)]^{1/2}$ as the quantum mechanical result. The spontaneous magnetization decays as temperature increases toward the Curie temperature.

Graphs of M as a function of H, namely magnetization curves, are commonly used as an illustration of magnetism types of materials. In paramagnets and diamagnets, the magnetization curves are represented by a positive and negative slope respectively, both of which are reversible in dipole moment orientations, restoring its random alignments when the applied field is removed. For ferromagnets, however, the magnetization increases with increasing magnetic field until they have reached the saturation M_s with a corresponding field H_s. Further elevation of magnetic field strength does not change magnetization value since all magnetic (Weiss) domains are aligned, reaching its maximum value. In B-H plots, though, the magnetic induction increase linearly as a result of intrinsic response to applied magnetic field beyond saturation.

When the applied field slowly decreases, magnetization does not follow the previous path, but a curve with higher values due to the irreversibility of domain in ferromagnets. When the applied field is removed, the intrinsic demagnetizing field rotates domains in opposite direction. However, such field is not strong enough to overcome the exchange interactions between domains. The magnetization remains as remanence or remnant magnetization M_r. Fully demagnetization occurs at coercivity or coercive field strength H_c, which is a measure of the "hardness" of the material among ferromagnets in terms of the energy required for demagnetization. At coercivity, the net magnetic moment is zero but not necessarily randomized.

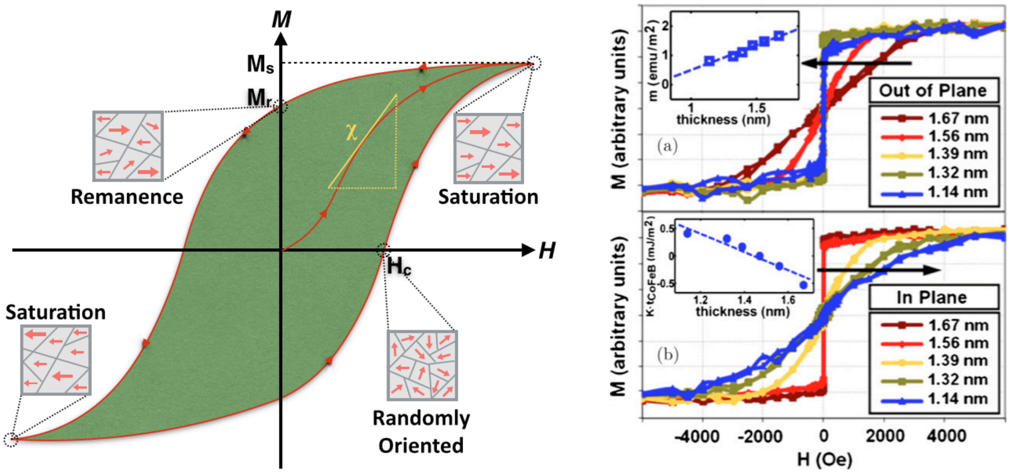

Figure A.2 Typical hysteresis loop for ferromagnets with domain wall motions (left). M-H curve of CoFeB with out-of-plane and in-plane field at various thickness (right, adapted from ref (Amiri 2012)

Further increase in the opposing field would reverse the behavior previously described by saturating the magnetization in the different direction, and complete the loop by increasing the field until the positive coercivity. The entire loop is termed hysteresis curve. The permeability is represented as the slope of the curve as a function of the applied field. The magnetic dipoles cannot be reset to random alignment unless the material is heated beyond its Curie temperature, T_c, above which becomes paramagnetic as thermal energy dominates.

Unlike paramagnets, ferromagnets allow the neighboring spins to have parallel orientation instead of randomly oriented. From quantum mechanics, the system with parallel spins is more energetically favorable due to exchange interactions between spins, overcoming the thermal energy in randomly aligning spins. Exchange interaction occurs between indistinguishable fermions, whose spin number is multiple of half-integer. Electrons are fermions and limited by Pauli exclusion principle that two electrons cannot occupy identical quantum states that two electrons are antisymmetric when exchanging. Hund’s rule suggests electrons tend to maximize their total spin. It indicates each orbital has to be filled with one electron with parallel spin before pairing in the same orbital. Qualitatively, such arrangement minimizes electron spatial overlap between orbitals and thus electron repulsions.

Consider a two-electron system in hydrogen with atom *a* and *b* with electron positionsr1 and r_2, the total wavefunction is the product of functions in spatial (Ψ r_1,r_2)) and spin (χ(s_1,s_2)) coordinates. As electrons are indistinguishable and thus have antisymmetric wavefunction overall, the spatial coordinate can be symmetric and antisymmetric with the complimentary spin coordinate,

$$\Psi_{S,A}\left(\mathbf{r}_1,\mathbf{r}_2\right)=\frac{1}{\sqrt{2}}\left[\psi_a(\mathbf{r}_1)\psi_b(\mathbf{r}_2)\pm\psi_a(\mathbf{r}_2)\psi_b(\mathbf{r}_2)\right] \tag{A.32}$$

which Ψ_s represents spatially symmetric wavefunction with antisymmetric spin interchange; Ψ_A represents spatially antisymmetric wavefunction with symmetric spin interchange. To calculate the energy of the system, the Hamiltonian operator is used,

$$E_{S,A}=\left\langle\Psi\left(\mathbf{r}_1,\mathbf{r}_2\right)\middle|\hat{H}\middle|\Psi\left(\mathbf{r}_1,\mathbf{r}_2\right)\right\rangle \tag{A.33}$$

$$\hat{H}=-\frac{\hbar}{2m}\left(\nabla_1^2+\nabla_2^2\right)-\frac{Ze^2}{4\pi\varepsilon_0 r_1}-\frac{Ze^2}{4\pi\varepsilon_0 r_2}+\frac{e^2}{4\pi\varepsilon_0 r_{12}}$$

After mathematical manipulations of the equations, the solution is grouped into four energy contributions. The total energy is the sum of individual energies of the orbitals (E_a and E_b), Coulomb interaction between two electrons (C), and the exchange interaction (J_{ex}):

$$E_{S,A}=E_a+E_b+C\pm J_{ex} \tag{A.34}$$

where the minus sign represent the antisymmetric spatial coordinate, and symmetric spin ordering. In such cases, parallel spin configuration has less total energy than aligning in antiparallel fashion. As a result, when the exchange coupling is strong, such as Fe, Co and Ni, FM ordering is preferred. Notice that J is the form of,

$$J_{ex} = \int \psi_a^*(r_1)\psi_b^*(r_2)\hat{H}\psi_a(r_2)\psi_b(r_1)dr_1dr_2 \tag{A.35}$$

Although quantum mechanics suggested parallel spins contribute the least energy to the system, but single magnetic domain is rare in nature. A single-domain material is similar to a permanent magnet that magnetic field conduct in the vicinity of the material, which requires a large magnetostatic energy to sustain. Therefore, magnetic domain intrinsically divides themselves into compartments in order to complete the magnetic circuit (flux closure domain), minimizing the demagnetizing field and the total internal energy of the system.

On the other hand, domains tend to align in certain crystallographic directions (easy axes) as energy required to magnetize in such orientations is lower, namely magnetocrystalline energy. The energy difference in magnetizing easy and hard axes is known as magnetocrystalline anisotropy energy. This quantity has been used extensively, as shown in Figure 1.2 for magnetic random-access memories (MRAM) and voltage-controlled magnetic anisotropy (VCMA) devices for switching of the device. To minimize the energy, larger domains tend to form along the easy axes for magnetization, while smaller domains with perpendicular orientation form to complete the magnetic circuit.

When the material is magnetostrictive, which elongates or contracts upon magnetization, flux closure domains build up strain along the domain walls and contribute strain energy to the total internal energy. Reducing the dimensions of closure domain would decrease strain, but increases domain exchange energies. The exchange energy is the lowest when neighboring spins are parallel; spins in the direction of easy axes lower the magnetocrystalline energy; while closure domains are required to reduce magnetostatic energy. Therefore, compromise between the three energies dictates the morphology of the domains.

The following table summarizes single-phase FM materials commonly used. Intermetallics, in general, can be sputtered or synthesized by physical vapor deposition. The adjustment of individual constituents in intermetallic allows tuning of coercivity and saturation magnetizations. Terfenol-D has exceptional high coercivity. However, the approach is not scalable in production while synthesis through chemical route is not trivial. Spinel ferrites such as cobalt and nickel ferrite are used as alternatives when retaining FM properties.

A.2 Ferroelectricity (Detailed)

Analogously, in order to understand ferroelectricity, the dielectric properties of materials have to be discussed. Dielectric materials are generally described as the ability to conduct electric field lines through the material before electrical breakdowns. Materials that could sustain large amount of electric field are regarded as insulators. When electric field, $E = E_0 e^{i\omega t}$ [V/m], is applied to dielectric materials, a electric flux density appears, $D = D_0 e^{i\omega t}$ [C/m^2], namely electric displacement. It describes the degree of bound charge displaced from its equilibrium position under applied electric field.

$$\mathbf{D} = \varepsilon \mathbf{E} = \varepsilon_0 \varepsilon_r \mathbf{E} \tag{A.36}$$

The proportionality is described by permittivity of the medium ε [F/m]. The subscript 0 and r correspond to vacuum and relative permittivity respectively. Similar to magnetic materials, the permittivity can be expressed by a real (ε') and imaginary part (ε"). The imaginary part describes dielectric loss due to absorption and resonance in high frequency applications, where the induced flux exhibit phase lag δ,

$$\varepsilon = \frac{\mathbf{D}}{\mathbf{E}} = \frac{D_0 e^{i(\omega t - \delta)}}{E_0 e^{i\omega t}} = \varepsilon' - i\varepsilon'' \tag{A.37}$$

The mathematical relation between the real and imaginary parts is described by the Kramers-Kronig integrals. The above equation is written in the form of $N = n_r + ik$ in spectroscopic analysis, where n_r is the refractive index and k is the absorption coefficient, both as a function of frequency. A convenient quantity, loss tangent, is defined to indicate the energy loss upon applied magnetic field, $\tan\delta_e = \varepsilon' / \varepsilon''$. The subscript e corresponds to electric loss tangent in compare with magnetic loss tangent.

When electrical dipoles are induced and aligned in the field direction, an internal electric field is created. The total built-in field is called polarization P, analogous to magnetization in magnetic materials. For materials that could sustain polarizations after the removal of external field, they are termed ferroelectric, which will be discussed later in the chapter.

Under external field, electrons are displaced towards the cathode and bounded by the nucleus, inducing dipole moments *p*, as the basic unit of polarization,

$$\mathbf{p} = \sum_{j}^{Z} q_j \mathbf{r}_j \tag{A.38}$$

where *q* refers to the charge of the electron with a relative position vector r from its resting position. Collection of microscopic electric dipole moment yields the macroscopic vector quantity, polarization density P, which is defined as the density of dipole moment per unit volume [C/m^2], that is, P = Np/V, where N is number of dipoles and V is the volume.

To quantify the internal field created from dipoles alignment n response to external field E, electric susceptibility (χ_e) is introduced.

$$\mathbf{P} = \varepsilon_0 \chi \mathbf{E} \tag{A.39}$$

The internal field further displaces dipoles and thus the total displacement can be expressed as follows,

$$\mathbf{D} = \varepsilon_0 \mathbf{E} + \mathbf{P} = \varepsilon_0 \left(1 + \chi_e\right) \mathbf{E} \tag{A.40}$$

It should be noted that the permittivity is related to the susceptibility by $\varepsilon_r = 1 + \chi_e$. Therefore, the susceptibility should also be a function of frequency of the applied field. Similar to Equation (A.5), permittivity and susceptibility become tensor quantities when the material is not isotropic.

In magnetism, the contributing factor of magnetization is originated from electron spins, spin-orbital coupling and exchange interactions. In dielectrics, polarization is a collective contribution from separation of charges and induced electric fields as suggested in Equation(A.41). However, each dipole moment is induced based on the local electric field it experiences. This field can be decomposed into four parts,

$$\mathbf{E}_{local} = \mathbf{E}_{ex} + \mathbf{E}_{surf} + \mathbf{E}_{Lorentz} + \mathbf{E}_{cavity} \tag{A.41}$$

where E_{ex} is the external applied electric field; E_{sufis} the surface charge depolarization field; $E_{Lorentz}$ is the Lorentz cavity field; and E_{cavity} is the field inside the cavity.

Consider an electric field is applied along the thickness of a thin slab. The charge density in the bulk volume of the slab will always be zero, if the material is neutral and isotropic. The unbalanced charge density appears on the surface, inducing an internal electric field antiparallel to the external field, known as depolarization field. The field strength equals to the electric field produced from the surface and derived through Gauss' Law:

$$\mathbf{E}_{surf} = \frac{\sigma}{\varepsilon_0} = -\frac{NP}{\varepsilon_0}\hat{\mathbf{n}} \tag{A.42}$$

where the negative sign suggested the antiparallel nature of the macroscopic polarization. The equation can be generalized by depolarization factor N_p to account for the morphology of the material, which equals to 1 for thin slab. The sum of first two terms in local field is called homogenous field E_0.

An imaginary spherical cavity is removed from the material for calculating the field experienced at the center of the sphere. The local field from this portion can be treated as the sum of the field produced from dipoles inside the sphere, namely the Lorentz field $E_{Lorentz}$, and the field inside the sphere, E_{cavity}. This charges induced on the surface of the cavity has the opposite charges as the polarization to represent the charges enclosed, as shown in (A.43).

The field can be calculated by integrating the surface charge density on the sphere,

$$\mathbf{E}_{Lorentz} = \int_0^{\pi}\left(\frac{1}{4\pi\varepsilon_0}\frac{q}{r^2}\right)\cos\theta d\theta = \int_0^{\pi}\frac{2\pi(r\sin\theta)rd\theta\cdot P\cos\theta}{4\pi\varepsilon_0 r^2}\cos\theta\, d\theta = \frac{1}{3\varepsilon_0}\mathbf{P} \qquad \text{(A.43)}$$

The positive solution indicates parallel direction as the external field. The last contribution to the local electric field is from dipoles inside the cavity. It takes into account the charges from atoms and ion in the sphere.

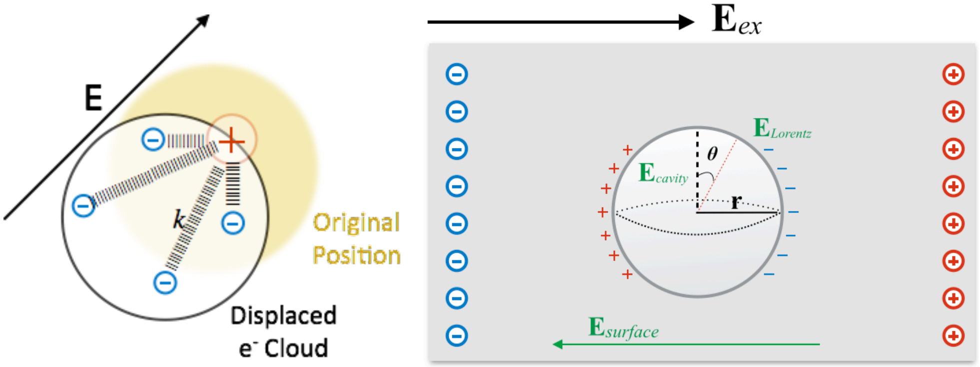

Figure A.3 Electronic polarization by the displacement of electron cloud (left). Contributions of local electric field at the center of an imaginary cavity in dielectric materials (right).

Since there is no net charge inside the cavity when charges are assumed to homogenously distribute, no electric field can be deduced, such that $E_{cavity} = 0$. However, this may not be always the case for non-cubic crystals. Finally, the total local field is given by,

$$\mathbf{E}_{local} = \mathbf{E}_0 + \frac{1}{3\varepsilon_0}\mathbf{P} \qquad \text{(A.44)}$$

The total field is slightly different from the macroscopic field since the reference charge located at the center of the imaginary sphere is not taken into field calculations. This charge experiences the total local field and thus polarized. A dipole moment can then be described by the local electric field with polarizability α of an atom.

$$\mathbf{p} = \alpha \mathbf{E}_{local} \tag{A.45}$$

Through substituting the above equation into calculating polarization, the Clausius-Mossotti relation can be obtained, which describes the permittivity of isotropic materials such as ionic compounds to be,

$$\frac{\varepsilon - 1}{\varepsilon + 2} = \frac{1}{3\varepsilon_0} \sum (N\alpha)_j \tag{A.46}$$

Physically, polarization can be categorized into four parts: electronic polarization (electron displacement), ionic polarization (ion displacement), and orientation polarization (molecular dipole moment reorientation). Corresponding polarizability can be derived depending on the type of polarization and the morphology of the material. Interfacial polarization is the fourth category in polarization mechanism. It describes dipoles trapped at defect sites and gram boundaries including mobile charges and impurities. Since there is no general way to quantity such polarization, it is often omitted in dielectric discussions.

It should be noted that polarization mechanism reacts differently to the frequency of the applied field since the body being acted on is different. As the electric field oscillates, dipoles resonate in response to the external field. In general, the smaller the entity, the faster it could response due to inertia. When the resonance frequency is reached, all of the driving electric field is absorbed. (A.45) shows the total variation of susceptibility (or refractive index, polarizability) as a function of driving frequency.

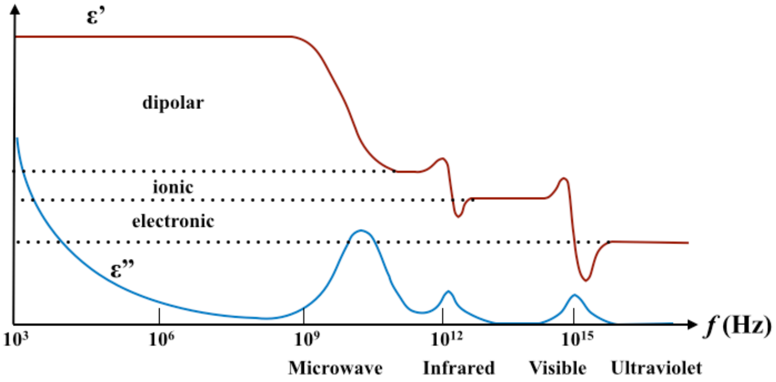

Figure A.4 Real and imaginary dielectric function as function of the frequency of applied electric field.

All dielectrics are electrostrictive due to certain degree of ion or charge polarization and result in dimension changes. Under external field, electric dipoles (and domains) are induced and attract neighboring dipoles and. It results in compression in the field direction, while expansion occurs in the perpendicular directions. The induced strain is generally small, and can be described by a quadratic dependence of external field.

Among 32 crystal classes, 11 point groups are centrosymmetric, which often have balanced polarizations. The remaining non-centrosymmetric crystal classes, with one exception, are known as piezoelectric materials. Unlike electrostrictive effect, piezoelectric effect is a linear response and has the ability to expand or contract depending on the direction of the field. The inverse effect produces electric field under mechanical stress. Two coupling of strain and polarization can be illustrated as,

$$\begin{cases} \mathbf{P} = d\sigma + \varepsilon_0 \chi \mathbf{E} \\ \mathbf{S} = s\sigma + d^T \mathbf{E} \end{cases} \tag{A.47}$$

where s is the elastic compliance; and d is the piezoelectric coefficient [m/V]. Common materials such as barium titanate ($BaTiO_3$), lead zirconate titanate (PZT), and lithium niobate ($LiNbO_3$) are used as actuators, microphones, motors and ultrasound generators.

Ferroelectric material has attracted great interests from research field due to the multi-functionality of the material class. From the classification of material properties, FEs are a subset of pyroelectric materials within a larger set of piezoelectric materials. Therefore, FE materials possess piezoelectricity (strain-electric field coupling), pyroelectricity (thermal-electric field coupling, and spontaneous dielectric polarizations. It has the ability to retain polarizations when external field is removed. Some ferroelectric often exhibits electro-optic effect with potential applications in optoelectrics.

Polarization curves in hysteresis loops are usually observed in FE materials in analogous to ferromagnetism. Controlling parameters in FE loops are remnant polarization (P_r), saturation polarization (P_s), and coercive field (E_c). Detail definition of the parameters can be referred to the description regarding magnetic hysteresis loop.

The temperature dependence of FEs can be described by the Curie-Weiss Law. Similarly, Curie temperature (T_c) indicates the onset of paraelectricity in analogy of paramagnetism, The long range ordering is destroyed and revert to little polarization when temperature is elevated above the Curie temperature. The domain wall movement is very similar to observations from ferromagnetism, in which magnetization is replaced by polarization. As a result, memory devices are developed known as ferroelectric random-access memories (FeRAM).

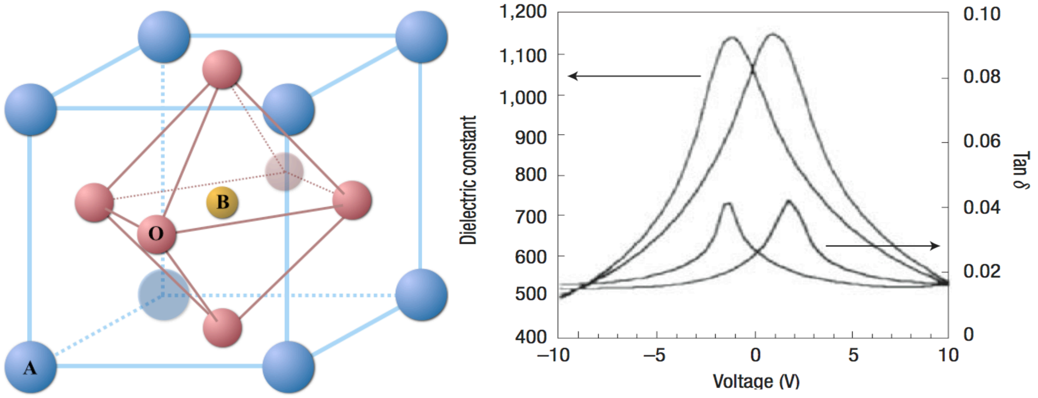

Figure A.5 Schematic of perovskite structure ABO_3 (left). Dielectric constant (permittivity) as a function of voltage in PZT thin film. “Butterfly” characteristic is observed (right, adapted from ref (Kingon 2005)).

One of the interesting features of FE material is the voltage-dependent permittivity. It is usually shown in capacitance-voltage (C-V) and dielectric constant-voltage (ε-V) characteristics. “Butterfly” shape is observed by changing DC voltage in two opposing directions. Such C-V profile measures the change of polarization with respect to the change in electric field, namely $\partial P/\partial E$. Therefore, the peak of capacitance corresponds to a large polarization change, at which near the vicinity of coercive field. From the discussion of hysteresis loop in ferromagnetism, coercive field is the energy required to decouple parallel magnetizations (or polarizations). The vicinity of the coercive field induces the largest domain reorientations and thus a high capacitance. Further voltage increase results in suppression of capacitance due to depletion of space-charge effects similar to MOS devices.

In general, FEs have various polarization mechanism. Displacive mechanism is the most common principle for ionic structures and perovskite crystal structures. Lead titanate is an example of this mechanism.

Perovskites has a chemical formula of $A^{(2+)}B^{(4+)}O_3$, which A and B are metal cations. Cation A are located at cubic corners (0,0,0) with eightfold coordination, cation B situated in the body-center (½,½,½) positions with octahedral coordination, while the oxygen atoms occupy face-centered position (½,½,0). The smaller cation usually located at the body-center with a charge of +4. At above Curie temperature, perovskites have cubic structure with space group Pm3m, and became tetragonal P4mm at temperature below and exhibit spontaneous polarization. Some complex perovskites contain two types of B-site cation to increase possible coordination of the domains, such as PZT ($Pb(Zr_{1-x}Ti_x)O_3$) whose neighboring cubic cell contain different B-site ions.

Under external electric field, cations and anions displace from the resting position corresponding to the field direction. Ionic polarization is then observed. In perovskite structures, similar displacements of the ions are observed. As the face-center sites for oxygen atoms do not have cubic surrounding, the local field is relatively large, and thus a larger response in ferroelectricity. Monoclinic and tetragonal are common phase transitions in perovskite structures and result in antiferroelectricity and paraelectricity. For example, lead titanate has phase transition from tetragonal to cubic at 760 K and becomes paraelectric.

The cause of polarization is further described by the softening and freezing of LO phonons that the frequency of the phonon decreases and becomes zero at phase transition. Mathematically, the amplitude of the phonon mode (i.e. dipole moment) becomes the order parameter in Landau theory, which will be discussed in next subchapter.

When the external field is removed, the polarization retains. Unlike ferromagnetism, polarization does not involve spin-orbital coupling and thus there is no exchange interaction between spins to stabilize the structure when Coulomb repulsion exists. Theoretical calculation shows that transition B-site ions allow *d*-hybridization with oxygen, which weaken short-range B-O repulsions(Cohen 1992). On the other hand, A-site ions stabilize the structure by coupling the ferroelastic responses to the FE distortions, which is usually on the order of 0.1Å. The total free energy is then decreased. At certain degree of distortion, the energy diagram shows local minimums especially in tetragonal crystal structure.

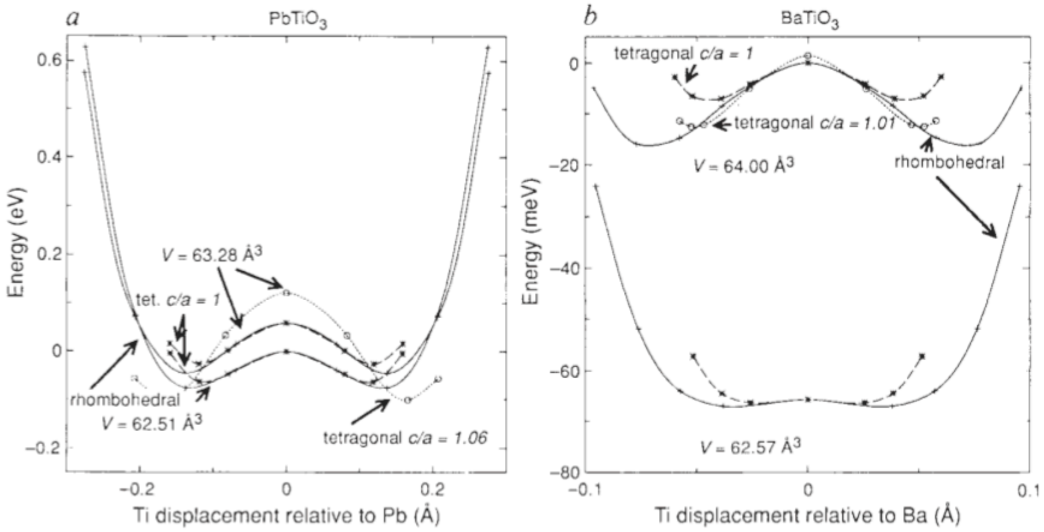

Figure A.6 Calculated energy diagram as a function of ferroelectric distortion for (a)$PbTiO_3$ and (b)$BaTiO_3$. Local minimum shows stabilized state with polarization (adapted from ref (Cohen 1992)).

Among all the FE materials, the selection of material of choice depends on the balance between material properties and synthesis difficulty. Some of the intrinsic materials such as manganese oxides (RMn_2O_5, $RMnO_3$), chromates ($RCrO_2$), and borates ($RFe_3(BO_3)_4$) are not included as they possess small piezoelectric response with Curie temperature below room temperature. Lead-containing compounds remain dominant for their strong piezoelectric couplings. Both $Pb(Mg_{0.33}Nb_{0.67})O_3$-$PbTiO_3$ (PMN-PT) and $Pb(Zn_{0.33}Nb_{0.67})O_3$-$PbTiO_3$ (PZN-PT) have complex compositions that would be difficult to control through certain synthesis route. On the other hand, PZT and lead zinc niobate (PZN) are simpler to synthesize while retaining good FE properties, and thus become common choices of material for research.

A.3 Landau Theory

Landau Free energy, *F*, is a thermodynamic quantity that defines the energetics in the vicinity of phase transition in a system, similar to Gibbs free energy describing how favorable a reaction occurs spontaneously. During phase transition, the system undergoes a change in symmetry, and the minimum of Landau free energy indicates the stability of the system under any controlling parameter such as temperature, pressure and external fields. It is assumed that higher-symmetry phase is always the state with higher temperature.

Landau suggested that free energy of the system can be described by Taylor series expansion in terms of some order parameters ζ for phase transition. Each term in the expansion correspond to difference in symmetry. This order parameter is a thermodynamic quality that, as Landau suggested, equals to zero for the phase with higher symmetry, and becomes non-zero for asymmetric phase, assuming no coupling terms between different order parameters. For most cases, temperature above a critical point T_c has a higher symmetry For example, magnetization and polarization are order parameters in ferromagnets and ferroelectricity phase transition respectively. Other typical systems include Bose-Einstein condensation, superconductivity and nematic liquid crystal. From a general power series in one dimension:

$$\Delta F\left(P,T,\zeta\right)=F_0+\alpha\zeta+A\zeta^2+\beta\zeta^3+B\zeta^4+\ldots \tag{A.48}$$

where F_0, A, B, α and β are functions of temperature and pressure. Higher-order terms are neglected as they are assumed to have positive expansion coefficient, which will not deviate the function from $F\rightarrow$ are func$\zeta| \rightarrow \infty$. Phase transition occurs when one of the coefficients changes sign, while other coefficient remain positive.

From the first derivative, $\alpha = 0$ for minimum *F* with the assumption $F(\zeta) = F(-\zeta)$. Odd-order terms are eliminated by the same assumption. From the second derivative, A > 0 for minimum *F* at $T > T_c$, and $A \leq 0$ for non-minimum *F* at $T < T_c$, leading to A = 0 at the critical point. In order to have the critical point to be stable, the third derivative has to be zero (i.e. $\beta = 0$) and the fourth derivative has to be positive for minimum F (i.e. B> 0). The free energy becomes,

$$\Delta F(P,T,\zeta) = F_0 + A\zeta^2 + B\zeta^4 \tag{A.49}$$

Assuming A can be expanded around T = T$_c$ such that A(P,T) =a(P)(T - T$_c$) and B(P, T)= B(P),Landau free energy is derived. Under some external field h, the extra energy is added as a linear coupling with the order parameter. The Landau free energy is as follows,

$$\Delta F(P,T,\zeta) = F_0 - hV\zeta + a(T-T_c)\zeta^2 + B\zeta^4 \tag{A.50}$$

In the case of no external field, the free energy hasglobal minimum at non-zero value of order parameter:

$$\begin{aligned} &\zeta = 0 && T > T_c \\ &\zeta = \pm\sqrt{\frac{a(T_c - T)}{2B}} && T < T_c \end{aligned} \tag{A.51}$$

It should be noted that $\zeta = 0$ is a local maximum when T < T$_c$. In condensed-matter physics, transitions involve a change in entropy (symmetry). First order transition involves release of latent heat. All thermodynamic quantity experiences an abrupt change in symmetry as a function of temperature. Second order transition involves continuous change. However, the first derivative is discontinuous, such as ferromagnetic-paramagnetic transition. The saturation polarization with zero external field can be expressed as,

$$\Delta F(P,T,\mathbf{P}_s) = F_0 + a(T-T_c)\mathbf{P}_s^2 + B\mathbf{P}_s^4 \tag{A.52}$$

which has the same solution as Equation (A.51). As all three solutions of the order parameter converge to zero when temperature approaches T$_c$, the function is continuous, and thus known as continuous phase transition (2nd order).

When an external field is applied, the expression to describe susceptibility can be derived. The first derivative extremum condition can be rearranged,

$$hV = 2a(T - T_c)\zeta + 4B\zeta^3 \tag{A.53}$$

and derive the characteristic field h_t such that it balance the free energy, and

$$V = \left(\frac{\partial \zeta}{\partial h}\right)_T \left(2a(T - T_c) + 12B\zeta^2\right) = \left(\frac{\partial \zeta}{\partial h}\right)_T \left(\frac{\partial^2 F}{\partial \zeta^2}\right) \tag{A.54}$$

where the sign of the partial derivative of order parameter dictates the extremums of F.

The plots indicate that, in the absence of external field, the free energy has a symmetric minimum at non-zero order parameter (i.e. P_r or M_r) when the temperature is below some critical temperature. When the temperature is above the crucial temperature, the minima returns to zero order parameter (i.e. ferroelectric-paraelectric transition). Under the applied field, one side of the minimum become global minimum depending on the field direction (i.e. P_s or M_s) at below T_c, while the field breaks the symmetry of phase transition.

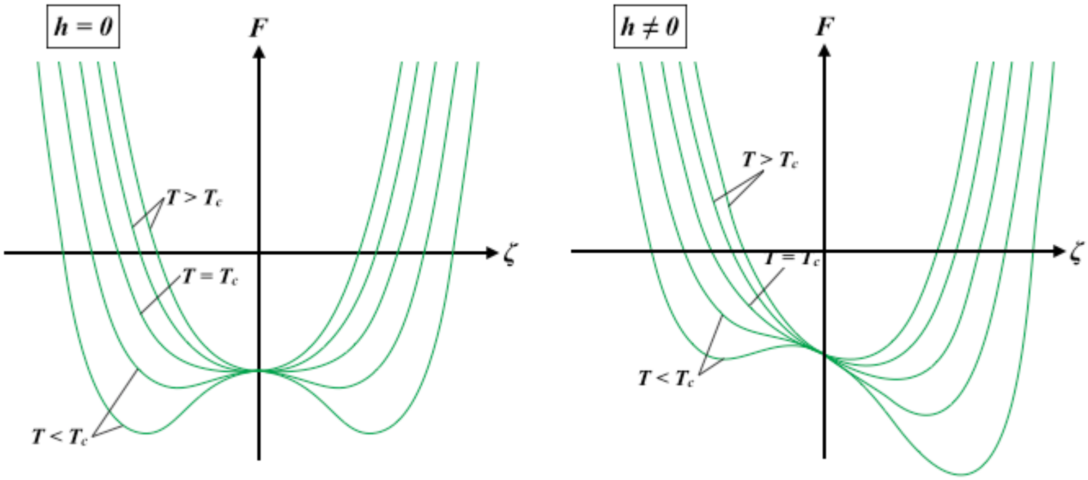

Figure A.7 Free energy as a function of order parameters with and without external field applied. The phase transition is first order as the free energy is continuous near T = Tc.

From the discussion in ferroelectricity and ferromagnetism, the susceptibility is then the partial derivative of order parameter with respect to external field,

$$\chi = \left(\frac{\partial \zeta}{\partial h} \right)_{T,h \to 0} = \frac{V}{2a(T - T_c) + 12B\zeta^2} = \begin{cases} V\left[4a(T_c - T)\right]^{-1} & T < T_c \\ V\left[2a(T_c - T)\right]^{-1} & T > T_c \end{cases} \tag{A.55}$$

which gives the Curie-Weiss law above T_c. At the critical temperature, however, the susceptibility diverges. Both polarization and magnetization can be explained by thermodynamic qualitatively near the critical temperature. However, the actual value of the expansion coefficients are distinct among different transitions, and often deviate from the predicted value in Landau theory as it does not include the effect of fluctuations under mean-field theory.

APPENDIX B. Standard Operating Procedures

B.1 ALD CFO Chamber Operating Procedure

Emergency Shutdown

1. Turn of the ion gauge for the chamber. On the Varian Multi-Gauge display press CHAN to switch to the chamber pressure, then press EMIS to turn off.
2. Close the UHV and LL-1 gate valves, both are manual valves
3. Turn off the Control Circuit Breaker on the compressor
4. Turn off the System Circuit Breaker on the compressor
5. Turn off the TMP by depressing the power button on the controller.

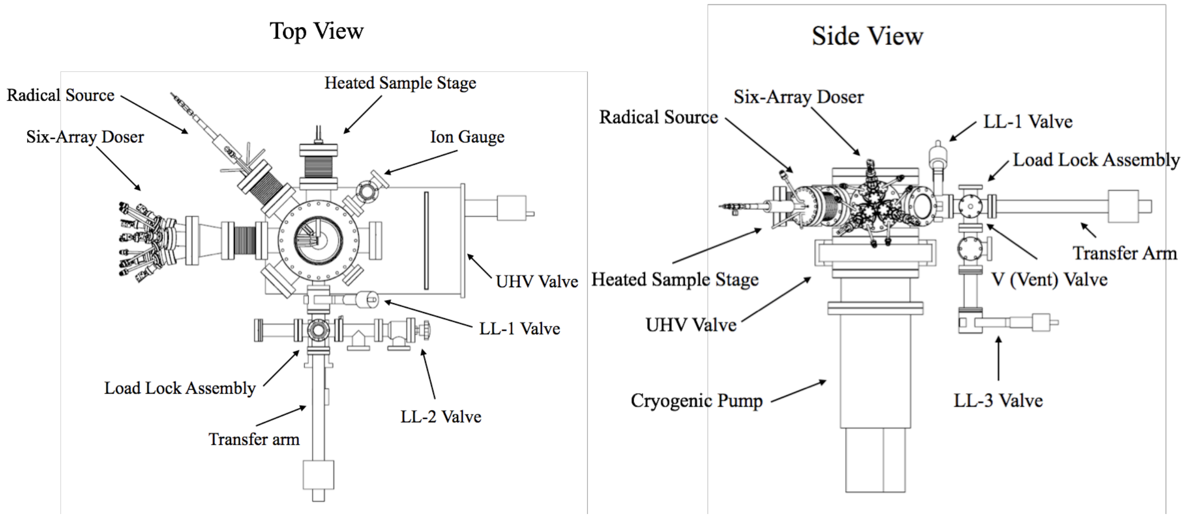

Figure B.1.1 Schematic of the ALD CFO system

Operating Procedures:

Load Lock

1. Venting the load lock chamber:
   a. Close the LL-1 gate valve to isolate the main MB chamber from the load lock chamber (this valve should always be closed)
   b. Close the LL-2 valve to isolate the load lock chamber from the mechanical pump
   c. Close the LL-3 gate valve to isolate the load lock chamber from the turbomolecular pump
   d. Open the V valve slowly to vent the chamber while observing the Pirani gauge to allow for controlled venting
   e. Sample can now be removed from/inserted into load lock

2. Pumping down the load lock chamber
   a. Close the V valve
   b. Turn off the 5-L pneumatic valve to isolate the turbomolecular pump from the mechanical pump
   c. Turn off the 5-U pneumatic valve for the differential pumping of the radical source
   d. Open the LL-2 valve slowly and watch the TC gauge reach the stabilized value (30-60 mTorr)

e. Once system reaches base pressure, close the LL-2 valve
f. Turn on the 5-L pneumatic valve and wait 15 seconds to avoid pressure backflow to the turbo
g. Open the LL-3 gate valve, load lock base pressure when pumped with Turbomolecular pump is 1.0Le-5 as shown on the Pirani gauge.

Radical Source

1. Turning on the plasma radical source:
   a. Before using H_2 gas, notify the lab and post the sign first
   b. Ensure that the cooling water is on; cooling water temperature should be about 18-20 °C
   c. Turn on the microwave power supply unit (*note*: let the electronics warm up for at least 20 minutes before engaging microwave power)
   d. Check the pressures of the gas cylinder and the gas line; if H_2 is used, open the H_2 gas cylinder and the gas line (*note*: all three valves on the regulator should be open and the pressure of the gas line should be ~20-30 psi)
   e. Turn off the 5-L pneumatic valve (closing the differential pumping line for radical system)
   f. Turn off the 5-U pneumatic valve (closing the back-pumping line for the turbomolecular pump)
   g. Evacuate the gas line through the mechanical pump by opening valve A-3 while watching the pressure on the TC vacuum gauge
   h. Wait until the pressure on the TC returns to base (the pressure should not fluctuate much)
   i. Set the gas MFC flow rate to 0%
   j. Open the valve before MFC controller:
      i. 1-U if O_2 is used or
      ii. 2-U if Ar is used
   k. Open the valve after the MFC controller:
      iii. 1-L if O_2 is used or
      iv. 2-L if Ar is used
   l. To make sure that the O_2 gas line is completely pumped, wait for the TC gauge (indicating MB chamber) to be pumped down to base pressure, then close the purging valve A-3
   m. Turn on the 5-U pneumatic valve (opening the differential pumping line for radical system)
   n. Turn on the 5-L pneumatic valve (opening the back-pumping line for the turbomolecular pump)
   o. Set the desired gas flow rate (~3%) on the MFC to achieve a pressure $\sim 5\times10^{-6}$ - 6×10^{-6} Torr (*note: the main chamber pressure should not exceed $3x10^{-5}$ Torr)*
   p. Press “ON” (green button) on the microwave power supply unit
   q. Increase the power to 25 watts
   r. If necessary, to attain the minimized reflected power to 0-1 watts, tune the tuning slug between the outer and inner conductor of the radical source

2. Turning off the plasma radical source

   a. Decrease the microwave forward power to zero
   b. Press "OFF" (red button) on the microwave power supply unit
   c. Decrease the MFC gas flow rate to 0%
   d. Close the valve before the MFC (valve 3-U or 4-U or A-2-U)
   e. Close the valve after the MFC (valve 3-L or 4-L or A-2-L)
   f. Close the injection valve A-1
   g. Close the gas cylinder and the gas regulator if H_2 is used
   h. Fill in the log sheet for H_2 run time
   i. Turn off the microwave power supply unit

Precursors

Precursor	Temperature controller			Pneumatic valve
	Housing	Gas line/valve	In-vacuum	
$Fe(TMHD)_3$	Controller 3, channel 1	Controller 3, channel 2	Controller 3, channel 3	#5
$Co(TMHD)_3$	Controller 1, channel 1	Controller 1, channel 2	Controller 1, channel 3	#7

1. Flowing the precursors
   a. Make sure that all the valves are open to prevent the gas lines from clogging
   b. Make sure that all the temperature controller are turned on, except during system maintenance
   c. Each precursor doser has three different heaters corresponding to different doser location. The corresponding heater switch numbers of the temperature controller for different precursors are listed as following
   d. Heat the precursors to operating temperatures by temperature controllers. The operating temperature of different precursors are listed below (note: the operation temperatures should not exceed individual precursor's decompose temperature):

Precursor	Operating temperature		
	Housing	Gas line/valve	In-vacuum
$Fe(TMHD)_3$	130	190	185
$Co(TMHD)_3$	120	190	185

2. Stopping precursor flow (when loading samples / pumping down)
   a. The pneumatic valves should be open at all times (prevent doser system clogging)
   b. Turn off the heaters that was turned on during deposition
   c. Check the MB chamber pressure by IG while the heaters are cooling down, make sure that the pressure dose not rise significantly

Cryogenic Pump

1. Starting the compressor

  a. Isolate the cryogenic pump by closing valve UHV connecting the cryogenic pump to the main chamber and valve CM connecting the MP to the cryogenic pump
  b. Make sure the cryogenic pump is not at low pressure (lower than mechanical pump base) by checking the pressure gauge on the cryogenic pump (reading should exceed 80 K) and if the cryogenic pump was recently turned off, condensation is a good sign
  c. Rough pump the cryogenic pump with the mechanical pump by slowly opening the CM valve
  d. Wait until mechanical base pressure reaches (~30-60 mT), then close cryogenic pump roughing valve CM
  e. Quickly set the System Circuit Breaker to the ON (UP) position
  f. Then set the Control Circuit Breaker to the ON (UP) position

2. Turning off the compressor
  a. Isolate the cryogenic pump by closing valve L-1
  b. Set the System Circuit Breaker to the OFF (DOWN) position
  c. Set the Control Circuit Breaker to the OFF (DOWN) position

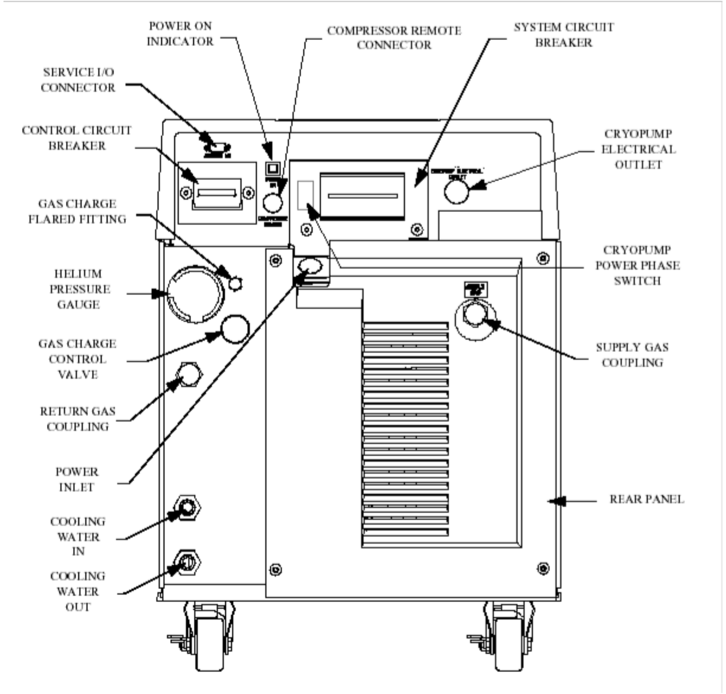

Figure B.1.2 Compressor for cryogenic pump

Main Chamber

1. Venting main chamber (only for maintenance)
  a. Close the 5-L (PV-9) valve to end the differential pumping for radical source
  b. Close the A-1 valve to stop gas injection to radical source
  c. Turn off the ion gauge by selecting the controller (Multi-gauge channel 1) and pressing “Emis” *(note: the ion gauge will can be seriously damaged if it remains on while venting)*
  d. If the load lock chamber is at its base pressure, close the LL-3 gate valve. But if the load lock chamber pressure is higher than its base, pump it with the turbomolecular

  pump first (*note: for the pump down process of the load lock chamber, please see the previous section*)
  e. Open valve LL-1 to connect the load lock chamber and main chamber
  f. Close the UHV gate valve to isolate the cryogenic pump
  g. Close the LL-3 valve to isolate the chamber from the turbomolecular pump
  h. Slowly open the V venting valve, observe the pressure increase on Pirani gauge (*note: the Thermocouple gauge should stay at base pressure since mechanical pump is isolated*)
  i. Eventually, the Pirani gauge should be displaying 5.5x 10^2 Torr, depending on the ambient condition

2. Pumping down main chamber (only for maintenance)
   a. Make sure that the load lock chamber is connected to the main chamber and both of them are completely vented (Pirani gauge displaying 5.5x 10^2 Torr)
   b. Close the V venting valve and the load lock door
   c. Close the 5-U pneumatic valve (green) to protect the turbomolecular pump and close the 5-L pneumatic valve (red) for the radical source differential pumping and isolating them from the mechanical pump *(note: prevent back flow)*
   d. Open LL-1 roughing valve to pump down the system by mechanical pump, the Pirani gauge readings should decrease while the Thermocouple gauge will first have a drastic increase but decrease to its base pressure afterwards. (*note: the base pressures for Pirani gauge and Thermocouple gauge are low 10^{-2}Torr and ~60-100 mTorr, respectively*)
   e. Remember not to isolate the Turbomolecular pump too long otherwise the Turbomolecular pump seriously can suffer serious damage. Therefore, it is normally recommended to turn off the turbomolecular pump if it is to be isolated for longer than 10 minutes. However, for occasions when turning off the turbomolecular pump is not feasible, it should be pumped by mechanical pump every 10-15 minute interval, by closing the LL-2 valve and then open the 5-U valve for a few minutes. Close 5-U valve and open LL-2 valve to pump down the system again after pumping down the Turbomolecular pump
   f. Once the base pressure of the mechanical pump is reached, start pumping down the system with Turbomolecular pump by closing the LL-2 valve (*note: to isolate the mechanical pump*) and then open the 5-L valve (*note: to connect the Turbomolecular pump with the mechanical pump*), and then open the LL-3 valve. The Pirani gauge reading should be lower than 10^{-4} Torr
   g. When the base pressure is reached, close LL-1 gate valve to isolate the load lock chamber from the main chamber
   h. Open the UHV gate valve to pump down the main chamber by cryogenic pump. Turn the ion gauge by selecting Multi-gauge channel 1 and pressing "Emis". The base pressure should be lower than 10^{-6} Torr

Deposition Procedures

1. Check pressure of chamber and resistances of heaters
2. Ensure pneumatic valves for dosers are open to prevent clogging

3. Turn on heaters for precursor doser and housing as well as sample stage using temperature controller.
4. Turn on radical source power supply to warm up electronics
5. When temperatures have reached set points, close pneumatic valves for dosers to prevent reaction when radical source is turned on
6. Pump down radical source gas supply by opening manual valve 5-L leading to mechanical pump. Then open lower pneumatic valve for intended gas (1-L for O_2 or 2-L for Ar) and upper pneumatic valve (1-U for O_2 or 2-U for Ar). When sufficiently pumped, close manual valve 5-L.
7. Open inlet gas supply for radical source by first opening manual valve A-1 at radical source Check pressure gauges to check for leaking. Turn on mass flow controller for intended gas.
8. Turn on radical source power supply to check if plasma strikes. If plasma strikes, leave on for several seconds to terminate substrate surface with radical atoms.
9. Turn off radical source power supply

Automated Deposition Procedures

1. Starting an automated deposition
   a. After following instructions in section B.2.7, input desired numbers onto automation control window for number of total global cycles, number of precursor cycles, metal precursor exposure time (in seconds), pump-down time (in seconds), and oxidant exposure time (in seconds).
   b. Press start button (resembles a black triangle like a PLAY button)

2. Stopping an automated deposition
   a. If a deposition is still running and has not reached the total number of global cycles, press the STOP button following a radical exposure step.
   b. Click on Tools -> Measurement & Automation Explorer
   c. Expand “Devices and Interfaces” under “My System”
   d. Locate NI-USB 9481 “Microwave Power” and right click
   e. Left click on Test Panels
   f. Press “Start” and make sure all switches are in the “Low” configuration
   g. Press “Stop”
   h. Close the Test Panel and close the Measurement & Automation Explorer
   i. Press the “ON” manual switch for the microwave power source and ramp down the power to zero
   j. Press the “OFF” manual switch for the microwave power source
   k. Turn off the flow of oxygen gas by closing the upper valve, setting the mass-flow controller to zero, and closing the lower valve. Allow the system to pump down to base pressure.
   l. Close the manual valve A1 leading to the gas feed-through on the radical source
   m. Flip the manual switches to open the Pneumatic valves for all the precursors
   n. Turn off the temperature controllers

B.2 ALD PZT Chamber Operating Procedure

Chemicals Used

- Lead bis (2,2,6,6-tetramethyl-3,5-heptanedionato) [$Pb(C_{11}H_{19}O_2)_2$, $Pb(TMHD)_2$]
- Titanium diisopropoxidebis (2,2,6,6-tetramethyl-3,5-heptanedionato) [$TI(O\text{-}i\text{-}C_3H_7)(_2(C_{11}H_{19}O_2)_2$, $Ti(O\text{-}i\text{-}Pr)_2(TMHD)_2$]
- Zirconium tetrakis(2,2,6,6-tetramethyl-3,5-heptanedionato) [$Zr(C_{11}H_{19}O_2)_4$, $Zr(TMHD)_4$]
- Deionized Water

.

Emergency Shutdown

1. If depositing, stop the LabView program.
2. Shut down all the electronics: Temperature Controllers (top and bottom), Water Heating Transformer, Mass Flow Controller control panel, and Substrate Heating Transformer.
3. Close all the precursor/reactant valves: Pb (V12), Zr (V8), Ti (V10), N_2 (V9), and H_2O (V5)
4. Manually close the roughing valve to isolate the chamber.
5. Proceed to emergency exit locations.

Operating Procedures

1. *Initial check:* Check TC pressure gauge reads base pressure, make sure all the valves are closed, and both temperature controllers (top and bottom) are reading room temperature on all channels.

2. *Venting the chamber:* Close the roughing valve to isolate the chamber, unlock the viewing port so it is able to open when vented, set the N_2 MFC (channel 4) to 50%, open the N_2 line (V1, V2, V4, and V9), and wait 1-5 minutes. Once the door opens, close the N_2 line (V1, V2, V4, and V9), set the N_2 MFC (channel 4) to 0%, and close the viewing port.

3. *Sample loading:* Make sure chamber is vented. Take off the conflat flange with TC/power feedthrough and load the sample onto the substrate heater. Use the multimeter to check the resistance. Readings should be:
   Across the thermocouples: 0.5 ohms
   Across the power leads (through sample heater): 8.9 to 9.5 Ohms
   Across the power leads (through transformer): 0.2 Ohms
   From thermocouple to power leads: OL
   From thermocouple to chamber wall: OL
   From power leads to chamber wall: OL

If resistance readings are too high, ensure that the screws on the sample heater are fully tightened. If there is shorting through the chamber wall, remove the sample and adjust its position accordingly.

If resistance readings are correct, then attach the conflat flange to the chamber. Shine a flashlight through the closed viewport to help line up the sample surface parallel to the ground (and facing down). Check the resistance again after tightening the conflat flange

4. *Pumping the chamber:* Open the roughing valve very slightly, being careful not to overload the roughing pump. After 30 seconds, open the roughing pump valve fully and wait until the TC pressure gauge reads below 150 mTorr (should not take more than a minute).

5. *Nitrogen Purge:* (*) Open the first half of the N2 line (V1, V2, and V4) and set the N2 MFC (channel 4) to 50%. After 30 seconds, briefly open the rest of the N2 line (V9) for 5 seconds then let the chamber reach base pressure once again (should not take more than a minute). Repeat this until no further decrease in base pressure is observed. On the last purge, keep the N2 line (V9) open and set the N2 MFC to 0%, waiting until base pressure is reached, then close the N2 line (V1, V2, V4, and V9).

6. *Heating:*
    a. Check all the temperature settings on the temperature controllers for the channels you will be using.

	Setpoint Temperature (^oC)		*Channel (temperature controller)*
Pb valve	150 (ALD)	190 (CVD)	1 (top temperature controller)
Pb house	115 (ALD)	120 (CVD)	2 (top temperature controller)
Zr valve	190 (ALD)	190 (CVD)	3 (bottom temperature controller)
Zr house	180 (ALD)	170 (CVD)	4 (bottom temperature controller)
Ti valve	110 (ALD)	130 (CVD)	5 (bottom temperature controller)
Ti house	75 (ALD)	90 (CVD)	6 (bottom temperature controller)
Chamber	100 (ALD)	460 (CVD)	7 (bottom temperature controller)

    b. Chamber walls and substrate heater: Heat the chamber walls by turning on channel 7 on the bottom temperature controller. Turn on the sample heater by setting the sample heater transformer to 55%. The chamber wall should be heated for 1 hour before heating the precursors and 2 hours total before starting the deposition.
    c. Precursors: After heating the chamber walls and substrate for at least 1 hour, begin heating the Pb, Ti, and Zr housings and valves by turning on the appropriate channels on the appropriate temperature controllers (see table above). The precursors need to be heated for 45 minutes before heating the water line and 1 hour total before starting the deposition.
    d. Water: Heat the water line by connecting the heating cord to the power and turning the gray transformer to 25%. After the water line heats for 10 minutes, open the water line leak valve by 30 units to allow the flow of water vapor into the water gas line and wait 5 minutes.
    e. Record the base pressure after heating. Set the N2 MFC to 2% and open the first half of the N2 line (V1, V2, and V4). Deposition can now begin.

7. *Manual Deposition: The procedures are only for one cycle.*
    a. PbO Deposition
        i. Open Pb valve (V12) for 15 seconds.
        ii. Close the valve and wait 30 seconds to pump down the chamber to the base pressure.
        iii. Open Water valve (V5) for 15 seconds.
        iv. Close the valve and wait 45 seconds to pump down the chamber to the base pressure.
        v. *(if needed) Repeat Step 5* (*) *(Perform if the chamber doesn't go back to base pressure.*
    b. ZrO_2 Deposition
        i. Open Zr valve (V8) for 15 seconds.
        ii. Close the valve and wait 30 seconds to pump down the chamber to the base pressure.
        iii. Open Water valve (V5) for 15 seconds.
        iv. Close the valve and wait 45 seconds to pump down the chamber to the base pressure.
        v. *(if needed) Repeat Step 5* (*) *(Perform if the chamber doesn't go back to base pressure.*
    c. TiO_2 Deposition
        i. Open Ti valve (V10) for 15 seconds.
        ii. Close the valve and wait 30 seconds to pump down the chamber to the base pressure.
        iii. Open Water valve (V5) for 15 seconds.
        iv. Close the valve and wait 45 seconds to pump down the chamber to the base pressure.
        v. *(if needed) Repeat Step 5* (*) *(Perform if the chamber doesn't go back to base pressure.*
    d. Record the base pressure after deposition is done.

8. *Automated Deposition:*
    a. Check that all valves are closed and temperatures on the controller are reading correctly for all channels.
    b. Choose the desired LabView deposition program.
    c. Input the desired # of global cycles, PbO, ZrO_2, and TiO_2 cycle.
    d. Record the base pressure before deposition.
    e. Start the LabView program.
    f. After deposition is done, record the base pressure.

9. *Finishing the deposition:* Turn off the substrate heater and water line heater transformers, along with all temperature controllers. Open the rest of the N2 line (V9), set the N2 MFC to 0%, and wait for the chamber to reach base pressure, then close the N2 line (V1, V2, V4, and V9).

10. *Sample unloading:* Wait at least 1 hour for the chamber to cool down. Perform Steps 1 and 2, then take off the conflat flange with TC/power feedthrough from the chamber to unload the sample.

B.3 Superconducting Quantum Interference Device (SQUID) Measurements

1. Refilling Liquid Helium
    a. Check the remaining percentage of liquid Helium (>40%), refill liquid Helium into SQUID system if the percentage is too low
    b. To refill liquid Helium, firstly attach the pressured Helium gas cylinder to the liquid Helium tank (should be already attached), in order to provide back pressure to accelerate the refilling process
    c. Vent the Helium gas in the tank (note: due to the Helium liquid-gas equilibrium)
    d. Vent the Helium gas in SQUID using a tweezers to relieve pressure.
    e. Take off the cap on the liquid Helium tank, connect the tank and SQUID with the metal tube and secure the connections (note: gloves needed to prevent frostbite)
    f. Close the venting valve and open the valve connected to gas cylinder on the tank
    g. After the connection is secured, the refilling process should begin simultaneously
    h. The refilling rate should be around 2%/min, tune the flow controller of the cylinder to attain desired rate
    i. Turn off the cylinder valve when the filling percentage reaches 91%, wait until the percentage slowly increases to 100%
    j. Loosen the connections, pull out the metal tube, isolate the Helium cylinder from the tank
    k. Cap the SQUID and the tank back, remember to open the venting valve of the tank

Note:
· Liquid Helium is consumed faster when the experiment is under high magnetic fields
· Liquid Helium is needed for SQUID measurements to retain extremely low temperatures, which allows superconducting behaviors of the picking up coil
· Superconducting behavior of the picking up coil is needed to increase the sensitivity

2. Sample Preparation
    a. The magnetic field direction is fixed based on the configuration of the SQUID magnetometer. Therefore, in order to measure orientation-dependent magnetization, sample preparation is needed to accommodate.
    b. Sample holding rod is parallel to the field direction. To prepare samples for measuring in-plane (of substrate) magnetizations, the sample should be attached in the same orientation with plastic straw. To prepare samples for measuring out-of-plane (of substrate) magnetizations, the sample surface should be perpendicular to the straw, as illustrated below:

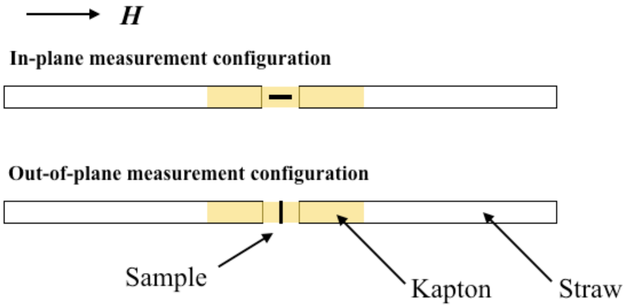

Figure B.2.1 Sample preparation for SQUID

3. Sample loading
    a. Under SQUID control software, click Sample -> Remove
    b. Wait for the yellow light to turn on for “venting” on the sample transfer head.
    c. Open the top cap. Remove the sample transfer rod with the back of the cap
    d. Attach the sample straw and make sure the sample is aligned properly
    e. Plunge a through-hole on both ends of the straw about 2 cm below the edge.
    f. Put the bottom sample straw cap at the end of the straw
    g. Insert sample rod into the SQUID chamber.
    h. Press “Purge” to purge the airlock system in SQUID
    i. Click Sequence, then depends on the sample being measured, click on the proper sequence. A sample sequence is attached after this section
    j. Center the sample position by clicking Measure -> RSO..
    k. After initiating transport, click “Center”
    l. The peak location of the red and blue color curves should coincide. If not, click “adjust manually” to input value. The system will center around the input value
    m. Input desired parameters for collecting data points
    n. Click on Run on the left column to start SQUID

The following is the sequence file used in the SQUID software. The steps are self-explanatory. New steps can be added by clicking the column on the right of the software. Double-clicking the existing step allows the user to input edits.

```
high res from 300 to -300 with 15 RSO, 5 RSO up to 1000 and 3 RSO for all
others
Set Temperature 298.000K at 10.000K/min.
Wait for Temp: Stable Delay: 30secs

Set Datafile:
C:\QdMpms\Data\JPChanglab\Cyrus\170410\AAO40_CFO42_PZT20_ip_600V
Start Data Logging C:\QdMpms\Data\JPChanglab\Logfile\SQUID logfile.env
60000ms Mask:8191 (VM)1 Overwrite:0

Set Magnetic Field 20000.00 Oe, No Overshoot, Hi Res Disabled

Scan Field from 20000.00 Oe to 10000.00 Oe in -5000.00 Oe increments (3 steps),
No Overshoot, Hi Res Enabled
    Wait for Temp: Stable Field: Stable Delay: 5secs
    Multi-Measure 3x Measure RSO: 4.00 cm, 5 cyc, 1 meas, 0.5 Hz, Center,
    AutoRng, Long, Iterative Reg., track:Yes, raw:Yes, diag:Yes
End Scan

Scan Field from 8000.00 Oe to 2000.00 Oe in -1500.00 Oe increments (5 steps),
No Overshoot, Hi Res Enabled
    Wait for Temp: Stable Field: Stable Delay: 5secs
    Multi-Measure 3x Measure RSO: 4.00 cm, 5 cyc, 1 meas, 0.5 Hz, Center,
    AutoRng, Long, Iterative Reg., track:Yes, raw:Yes, diag:Yes
End Scan

Scan Field from 1000.00 Oe to 300.00 Oe in -175.00 Oe increments (5 steps), No
Overshoot, Hi Res Enabled
    Wait for Temp: Stable Field: Stable Delay: 5secs
    Multi-Measure 3x Measure RSO: 4.00 cm, 5 cyc, 1 meas, 0.5 Hz, Center,
    AutoRng, Long, Iterative Reg., track:Yes, raw:Yes, diag:Yes
End Scan

Scan Field from 200.00 Oe to -450.00 Oe in -81.25 Oe increments (9 steps), No
Overshoot, Hi Res Enabled
    Wait for Temp: Stable Field: Stable Delay: 5secs
    Multi-Measure 5x Measure RSO: 4.00 cm, 5 cyc, 1 meas, 0.5 Hz, Center,
    AutoRng, Long, Iterative Reg., track:Yes, raw:Yes, diag:Yes
End Scan

Scan Field from -500.00 Oe to -1000.00 Oe in -100.00 Oe increments (6 steps),
No Overshoot, Hi Res Enabled
```

```
        Wait for Temp: Stable Field: Stable Delay: 5secs
        Multi-Measure 3x Measure RSO: 4.00 cm, 5 cyc, 1 meas, 0.5 Hz, Center,
        AutoRng, Long, Iterative Reg., track:Yes, raw:Yes, diag:Yes
End Scan

Scan Field from -2000.00 Oe to -8000.00 Oe in -1500.00 Oe increments (5 steps),
No Overshoot, Hi Res Enabled
        Wait for Temp: Stable Field: Stable Delay: 5secs
        Multi-Measure 3x Measure RSO: 4.00 cm, 5 cyc, 1 meas, 0.5 Hz, Center,
        AutoRng, Long, Iterative Reg., track:Yes, raw:Yes, diag:Yes
End Scan

Scan Field from -10000.00 Oe to -20000.00 Oe in -5000.00 Oe increments (3
steps), No Overshoot, Hi Res Enabled
        Wait for Temp: Stable Field: Stable Delay: 5secs
        Multi-Measure 3x Measure RSO: 4.00 cm, 5 cyc, 1 meas, 0.5 Hz, Center,
        AutoRng, Long, Iterative Reg., track:Yes, raw:Yes, diag:Yes
End Scan

Scan Field from -20000.00Oe to -10000.00 Oe in 5000.00 Oe increments (3 steps),
No Overshoot, Hi Res Enabled
        Wait for Temp: Stable Field: Stable Delay: 5secs
        Multi-Measure 3x Measure RSO: 4.00 cm, 5 cyc, 1 meas, 0.5 Hz, Center,
        AutoRng, Long, Iterative Reg., track:Yes, raw:Yes, diag:Yes
End Scan

Scan Field from -8000.00Oe to -2000.00 Oe in 1500.00 Oe increments (5 steps),
No Overshoot, Hi Res Enabled
        Wait for Temp: Stable Field: Stable Delay: 5secs
        Multi-Measure 3x Measure RSO: 4.00 cm, 5 cyc, 1 meas, 0.5 Hz, Center,
        AutoRng, Long, Iterative Reg., track:Yes, raw:Yes, diag:Yes
End Scan

Scan Field from -1000.00Oe to -300.00 Oe in 175.00 Oe increments (5 steps), No
Overshoot, Hi Res Enabled
        Wait for Temp: Stable Field: Stable Delay: 5secs
        Multi-Measure 3x Measure RSO: 4.00 cm, 5 cyc, 1 meas, 0.5 Hz, Center,
        AutoRng, Long, Iterative Reg., track:Yes, raw:Yes, diag:Yes
End Scan

Scan Field from -200.00Oe to 450.00 Oe in 81.25 Oe increments (9 steps), No
Overshoot, Hi Res Enabled
        Wait for Temp: Stable Field: Stable Delay: 5secs
        Multi-Measure 5x Measure RSO: 4.00 cm, 5 cyc, 1 meas, 0.5 Hz, Center,
        AutoRng, Long, Iterative Reg., track:Yes, raw:Yes, diag:Yes
End Scan
```

```
Scan Field from 500.00Oe to 1000.00 Oe in 100.00 Oe increments (6 steps), No
Overshoot, Hi Res Enabled
        Wait for Temp: Stable Field: Stable Delay: 5secs
        Multi-Measure 3x Measure RSO: 4.00 cm, 5 cyc, 1 meas, 0.5 Hz, Center,
        AutoRng, Long, Iterative Reg., track:Yes, raw:Yes, diag:Yes
End Scan

Scan Field from 2000.00Oe to 8000.00 Oe in 1500.00 Oe increments (5 steps),
No Overshoot, Hi Res Enabled
        Wait for Temp: Stable Field: Stable Delay: 5secs
        Multi-Measure 3x Measure RSO: 4.00 cm, 5 cyc, 1 meas, 0.5 Hz, Center,
        AutoRng, Long, Iterative Reg., track:Yes, raw:Yes, diag:Yes
End Scan

Scan Field from 10000.00Oe to 20000.00 Oe in 5000.00 Oe increments (3 steps),
No Overshoot, Hi Res Enabled
        Wait for Temp: Stable Field: Stable Delay: 5secs
        Multi-Measure 3x Measure RSO: 4.00 cm, 5 cyc, 1 meas, 0.5 Hz, Center,
        AutoRng, Long, Iterative Reg., track:Yes, raw:Yes, diag:Yes
End Scan

Set Magnetic Field 0.00 Oe, Oscillate, Hi Res Disabled
Set Temperature 298.000K at 10.000K/min.
```

End of sequence file.